CARDIFF UNIVERSITY

LASER HAEMOCYTOMETER

Sara-Jayne Gillgrass

A thesis submitted as partial fulfilment for the degree of

Doctor of Philosophy

School of Physics and Astronomy

28^{th} September 2018

Abstract

This thesis describes the work carried out to provide a proof of principle coupled-cavity laser measurement for blood cell analysis, using an integrated device with capillary fill microfluidics. The development of both light source and microfluidics on the same sensing platform provides complete integration and removes the dependence on external systems.

In principle, InAsP quantum dot lasers, cover a wavelength range extending into the near infrared, where the response of biological matter can provide useful diagnostic information. The suitability and limitations, of both an InAsP quantum dot and GaInP quantum well active medium, are considered for the coupled-cavity structure. A InAsP quantum dot structure with an 8 nm AlGaInP barrier between each dot layer was seen to have a slight improvement in device performance, but optical gain measurements indicated that this structure would not provide sufficient gain to overcome the high losses expected in the integrated device. Consequently, a GaInP quantum well was considered a sensible choice for a proof of principle coupled-cavity measurement.

The efficiency of an etched facet is key to overall performance in the coupled-cavity device and has been quantified using the gain characteristics of the quantum well structure. A value of facet efficiency was found to be $\eta_f = 0.37 \pm 0.04$, which is valid for all angles of etched facet. A very low facet reflectivity of $4.9\text{x}10^{-9}$ was measured for a laser with a 14.1^o etched facet.

Perturbation of the optical coupling between two laser/detector sections causes a change in the measured photo-voltage signal from the device. This effect has been employed to demonstrate detection of both 10 and 6 μm microbeads. In a coupled-cavity regime, a 22.6^o angled facet coupled-cavity laser pair has been shown to have a lower threshold current density than either of its individual sections, indicating its potential for sensing applications.

Acknowledgements

Firstly, I would like to express my sincere gratitude to my supervisor Prof. Peter Smowton for taking my on as a PhD student and giving me the opportunity to carry out this research. I would particularly like to acknowledge the invaluable guidance and encouragement I have received throughout this process. I would also like to thank my secondary supervisor, Dr Phil Buckle for the enthusiasm, continuous support and fabrication advice and knowledge during my time at the university.

I would like to give a special thanks to Dr Rob Thomas, whose experience, guidance and patience was invaluable. My PhD journey would not have been the same without him. I would also like to thank Andrew Harrison in the electronics workshop for his time and expertise, without it some of this research wouldn't have been possible. Thanks also goes to other members of technical staff including Chris Dunscombe and Dr Angela Sobiesierski for their help in the cleanroom.

Thanks to other members of the Optoelectronics group, especially Dr Sam Shutts, Dr Stella Elliot and Dr Lewis Kastein for their invaluable help over the years and Prof. Peter Blood for fuelling insightful Friday morning discussions.

Finally, a special thanks to all my friends (too many to name here but you know who you are) and parents, who provided copious amounts of encouragement, advice, coffee and alcohol!

Publications & Conferences

Conference Proceedings

P.M. Smowton, S. Shutts, R. Thomas, S.N. Elliott, A. Sobiesierski, I. Karomi, S. Gillgrass, A.B. Krysa, *"Quantum dot lasers for integrated photonics"*, ISLC Proceed., IEEE Xplore, pp. 1-3, 2016

R. Thomas, M. Holton, A. Sobiesierski, S. Gillgrass, H.D. Summers, D. Barrow and P.M. Smowton, *"Integrated III-V semiconductor flow cytometer with capillary fill micro-fluidics"*, IPC Proceed., IEEE Xplore, pp. 7-8, 2015

Conference Presentations

C.P. Allford, S. Gillgrass, M.S. Al-Ghamdi, A.B. Krysa, S. Shutts and P.M. Smowton, *"Barrier Width Effects in InAsP/AlGaInP Quantum Dot Lasers"*, UK Semiconductors, UK, 2018

S. Gillgrass, R. Thomas and P.M. Smowton, *"On-chip detection of micro-particles using an integrated coupled-cavity sensing platform"*, SIOE, UK, 2017

S. Gillgrass, R. Thomas and P.M. Smowton, *"Novel coupled-cavity sensing mechanism for on-chip detection of micro-particles"*, Photonics West, USA, 2017

S. Gillgrass, R. Thomas and P.M. Smowton, *"Identifying facet efficiency in angled facet deep-etched ridge structures"*, SIOE, UK, 2016

R. Thomas, S. Gillgrass, A. Sobiesierski, J. Piasecka, M.D.Holton, H.D. Summers, D. Barrow and P.M. Smowton, *"Reconfigurable laser arrays for integrated chip-based sensing"*, SIOE, UK, 2016

R. Thomas, M.D. Holton, S. Gillgrass, A. Sobiesierski, P.M. Smowton, H.D. Summers and D. Barrow, *"Integrated III-V semiconductor platform with capillary fill micro-fluidics for chip-based flow cytometry"*, IEEE BioPhotonics, Italy, 2015

S. Gillgrass, R. Thomas, M.D.Holton, A. Sobiesierski, P.M. Smowton, H.D. Summers and D. Barrow *"Monolithically integrated III-V semiconductor flow cytometer"*, UK Semiconductors, UK, 2015

R. Thomas, M.D. Holton, A. Sobiesierski, S. Gillgrass, P.M. Smowton, H.D. Summers and D. Barrow, *"Integrated III-V semiconductor platform with capillary fill micro-fluidics for chip-based flow cytometry"*, CYTO, UK, 2015

R. Thomas, M.D. Holton, S. Gillgrass, A. Sobiesierski, P.M. Smowton , H.D. Summers and D.

Barrow, *"Integrated III-V semiconductor platform with capillary fill micro-fluidics for chip-based flow cytometry"*, SIOE, UK, 2015

Contents

List of Figures

List of Tables

Chapter 1

Introduction

1.1 Thesis Rationale

An ever increasing world population, in part due to an increase in human life expectancy, is a cause for concern for medical professionals around the world. More time and money is needed to keep healthcare services running effectively, but with GP surgeries and hospitals, in the UK in particular, having ever lengthening waiting times, time is of the essence for those with urgent or critical needs. Paramount to this is the need for faster blood analysis and investigation of cell biology. This gives initial information about a patients health and whether further or more invasive tests are required.

The most useful tests include those concerning white blood cells (WBCs), since these are involved in the body's immune system where a change in levels can be an indicator of disease or infection. There are two categories of WBCs; granular and agranular. Granular WBCs are those with an abundance of highly visible granules, tiny fluid filled sacs, within the cell's cytoplasm. While not completely missing granules, agranular WBCs have a much smaller concentration of them and are much less visible under the microscope. Both these WBC types can be categorised further, and are shown in table 1.1. All 5 WBC types listed in table 1.1 are produced in red bone marrow, but have different functions within blood. Figure 1.1 shows the 5 main WBC types and their size comparison to each other. It also shows the difference in granularity and nucleus shape. Neutrophils are the most common of all the WBC types, and make up 50-70% WBC. They are usually 10-12 μm in diameter, with high levels being an indicator of bacterial infection. Eosinophils typically

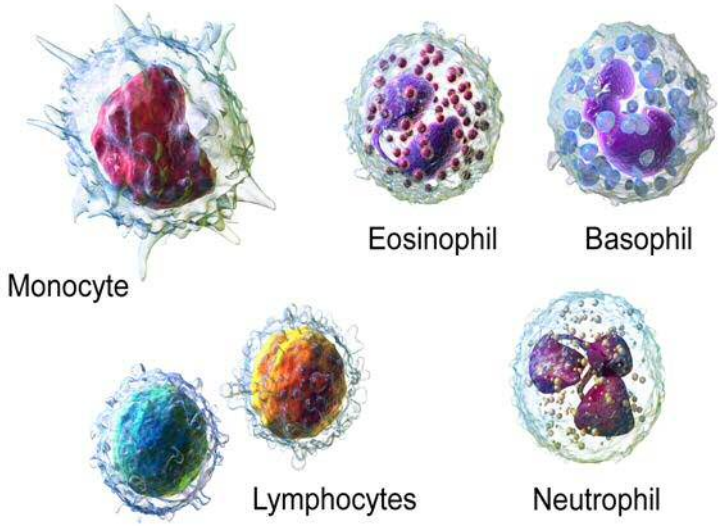

Figure 1.1: The 5 different white blood cell types [1].

represent 2-4% of the total WBC count, and are also 10-12 μm in diameter. However, the nucleus of an eosinophils is typically different in size and shape to that in a nuetrophil. High levels of this type of cell can indicate a parasitic worm infection or represent some autoimmune diseases. Basophils are the least common WBC, making up less than 0.5% of the total count, and are also smaller in diameter at 8-10 μm. High and low levels of basophils are associated with hypo and hyperthyroidism, respectively. Lymphocytes are the most common agranular WBCs, accounting for 20-30% of the total WBC count. These cells fall into two different diameter categories; 10-14 μm and 6-9 μm. The larger cells tend to have a smaller nucleus, so they are easily differentiated. Abnormally high levels of lymphocytes can be associated with some types of cancer and low levels can be caused by immunosuppression, such as that caused by HIV infection. Monocytes are the largest WBCs with diameters ranging from 12-20 μm, but make up just 2-8% of the total WBC count. High levels of monocytes are associated with some forms of leukemia.

Granular	Agranular
Neutrophils	Lymphocytes
Eosinophils	Monocytes
Basophils	

Table 1.1: Classification of white blood cells, in order of most common to least common for both granular and agranular types.

Blood analysis in the past was done using a haemocytometer (or hemocytometer). The haemocytometer was originally invented in the 19^{th} century by Louis-Charles Malassez to count blood cells, consisting of a glass chamber with an etched grid of specified dimensions [2]. This allows for the number of cells in a specific volume to be counted manually under a microscope. Although this method allows for easy enumeration, there are certain disadvantages [3]; large numbers of samples are time consuming, laborious and can potentially generate erroneous results.

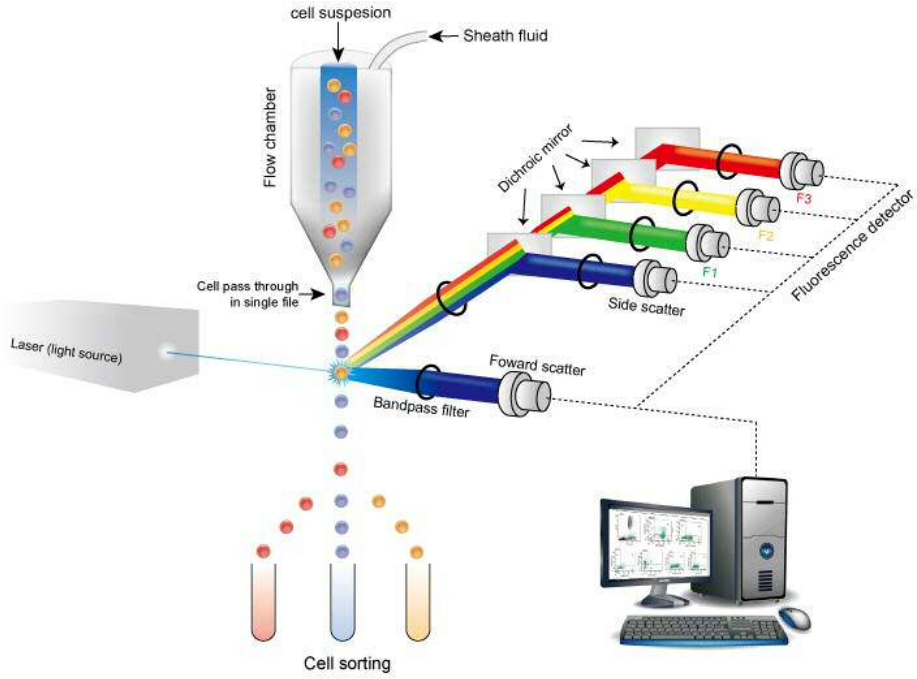

Figure 1.2: The three main components of a flow cytometer [4]; fluidics, optics and electronics, that together provide a complete system for cell analysis.

Recent advances in cytometric techniques, such as automated flow cytometry, allow rapid cell analysis and quantitative cell population measurements [5], overcoming the limitations of microscopy techniques. The four main components of a flow cytometer are the light source, fluidic system, optics and electronics (figure 1.2). The light source used is typically a laser since it can produce a high intensity monochromatic beam. The fluidic system allows for large numbers of cells, in a fluid suspension, to be processed by passing them single file through an optical system. The optical system usually comprises beam splitters and band-pass filters to allow detectors to measure both forward and side scatter light intensities and also fluorescence. The measured light intensity is converted to a photocurrent that the electronics system digitises for the user. Forward scatter is proportional to the size of the cell, and side scatter, typically measured at 90^{o} to the

laser beam, is proportional to the granularity of the cell. By analysing the forward and side scatter measurements together, cell populations can be easily distinguished based on size, shape and internal composition of the cell. This can be achieved by a cytogram, an example of which can be seen in figure 1.3. This current methodology is highly advanced in terms of data acquisition

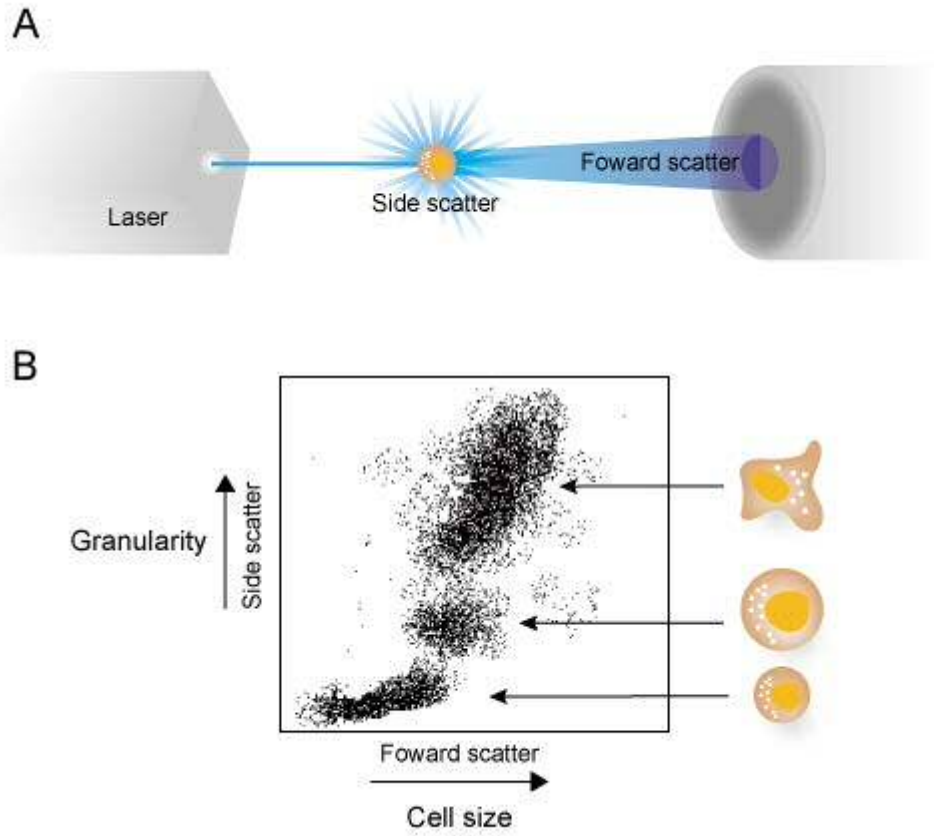

Figure 1.3: Measurement of forward and side scatter. Individual cells are divided according to the size and granularity within a population of different white blood cell types [4]

and information processing, but crude in the basic optical processes used for cell identification. Systems typically cost between $50,000 and $400,000, limiting widespread utilisation and are typically sited in specialist centres, such as hospitals, disadvantaging point of care and resource poor settings. This creates a demand for a portable, miniaturised haematology analyser for large scale distribution.

In recent years, progress has been made in a variety of research level micro-analysis systems for cell sensing with microfluidic separation and collection of WBCs [6]-[12]. However, these systems still require external light sources, detectors and other ancillary equipment in separate systems, meaning they are not truly portable and still do not offer low cost diagnostics. WBC

counting, by the Coulter method, with microfluidic electrical impedance sensors [13] are a simple way of determining cell populations and crude cell size measurements, but they suffer with result reproducibility issues from electrode damage [14], channel clogging [15] and compromised system robustness [16]. In the aforementioned microfluidic systems, bulky and relatively expensive liquid pumps, limits these devices' application to laboratory benchtop settings. Capillarity, which is the spontaneous motion of liquids due to their surface tension, allows for unaided fluid flow, removing the need for additional pumps, valves and interconnectivity. Paper (membrane) based liquid sample handling allows pump free fluid flow due to the capillary force along paper fibres [17]. These can be used with optical colourimetric or electrochemical methods to determine populations of small molecules, such as DNA [18], but the delivery systems cannot handle large particles like WBCs. Advances in paper based technology have allowed the development of smartphone enabled electrochemical sensors, using diffusion blockage effects to physically trap WBCs [19]. This method allows cell populations to be measured using a current response, with a relatively user friendly and portable device. However, the lack of cell information, such as size, from this approach leaves the door open to an integrated sensing device with a fully functional microfluidic system to be investigated.

Integration of components, including a light source and microfluidic system, by a number of different approaches, removes the dependence on external systems and is the focus of recent research [20] [21]. For capillary fill microfluidics, various lithographically definable (e.g. SU-8) or mouldable polymer (e.g. polydimethylsiloxane, PDMS) materials have been used to create these structures [22] [23]. However, it is the integration of a light source on chip that has proved the most challenging as fabrication of the fluidic and optical guiding functionality has focussed on the use of optically passive materials, e.g. PDMS, glass and silicon. Fabrication of lasers on chip has been achieved to date utilising external cavity lasers [24] and fluid dyes [25]. Although demonstrating excellent performance and sensing capabilities, they still require an external optical pump.

The use of an active III-V semiconductor platform, to integrate optofluidic sensors and systems, has been seen as offering the best solution for cost effective assembly, particularly for large scale integration. However, compromise in the performance of the system elements due to an active region that is not suitable for all functions, and defects introduced during the fabrication, have hin-

dered progress. Self assembled quantum dot (QD) material, in particular, eases these constraints and removes the barriers to the use of an active III-V platform by offering a wide range of operating wavelengths for multi parameter analysis, the possibility of relatively optimal operation of emitters and detectors fabricated on the same active material and immunity to defects created by the fabrication process due to 3-dimensional carrier localisation [26]. Commercial advantages of an active III-V integrated platform include utilising photolithography for the assembly of structural components and geometrical layout in a manufacturable manner, and the future compatibility with integrated electrical sensors and electrical data processing electronics.

We envisage a novel, capillary fill, microscale sensing instrument with integrated on-chip photonics, microfluidics and electronics for a non-technical user to access established and understood diagnostic parameters. Such a microscale system reduces the volume of blood required allowing for quasi-continuous and in-situ haematological monitoring, and can be used in emergency situations such as emergency surgery and childbirth, already seen with the commercial HemoSep® technology [27] to measure the percentage volume of RBC in blood. Further development to our approach, such as the inclusion of a radio-frequency emitter and smartphone controlled electronics, would allow for such a device to be implanted under the skin, offering a realistic route to continuous monitoring during everyday life. This is already available for patients with diabetes who require glucose monitoring, using products like the FreeStyle Libre™[28].

In this PhD, a novel, capillary driven, micro-scale microfluidic laser sensor on an active III-V substrate is proposed, in which, an analyte can flow through an etched-channel coupled-cavity laser. The analyte becomes an active element of the laser cavity and, in theory, will affect the coupling strength between the two sections of the coupled-cavity laser. In this case, perturbation in the light output of the device should be evident, advancing towards a potentially highly sensitive detection mechanism. One possible mode of operation using the cell material to change the optical loss in the gap can be accessed by using etched, angled, internal facets to tailor the reflectivity. This has the role of increasing the threshold gain for free-running lasing of the individual, isolated laser sections relative to that of the coupled-cavity operation. In the past, monolithic coupled-cavity lasers have been shown to have use in biochemical sensors, albeit through bulk sensing [29]. Also, the monolithic nature of this proposed system offers significant advantages in terms of achieving

good alignment and close proximity between the sensor and analyte.

Self assembled InP QD lasers grown on GaAs substrates cover a wavelength range of 645 nm - 750 nm [32] [33], extending the upper limits of compressively strained GaInP quantum well (QW) lasers. Longer operation wavelength can be achieved by growing larger QDs, but InP QD lasers are limited to around 750 nm at room temperature, due to difficulties with the planarisation of the epitaxial surface after growth of large dots [34]. Pushing the operation wavelength further towards the near infra-red band makes QD dot lasers a potential for bio-photonic sensing applications, where wavelengths towards 780 nm transmit deeper in blood [35], tissue and musculature [36], useful for our final vision. Incorporating arsenic into InP QDs increases the lattice mismatch to GaAs substrates whilst lowering the bandgap of the dot material. Therefore, QD structures can be engineered, by growth of InAsP QDs, to extend their operation wavelengths into the near infra-red [7]. Ultimately, InAsP and InP dot layers could be included in structures with GaInP quantum wells (QWs) to cover wavelengths from 630-800 nm if InAsP lasers can be shown to function sufficiently well.

A range of laser wavelengths is of use should measurements with fluorophores be useful in future systems. QDs grown by self-assembly inherently give rise to a fluctuation in dot size causing inhomogeneously broadened energy states, allowing gain to be achieved over a relatively wide spectral range. This characteristic of QDs can be employed to generate multi-wavelength sources [38] which are the mechanism behind many physiological measurements, such as arterial oxygen saturation [39] and blood flow [40]. The sub-linear gain characteristics of QD lasers also lend themselves to enhanced wavelength tuning [41] allowing for improved sensitivity and functionality in optical sensing measurements [42] [43].

The aim of this PhD has been to investigate epitaxial structures and angled facets for use in a novel integrated microfluidic coupled-cavity sensing mechanism. This work builds on the research of both Dr R. Thomas [30] and Dr H.H.J. Sapingi [31], both from Cardiff University, with the use of different coupled-cavity laser arrangements, the inclusion of an on-chip coupled-cavity detector, and a fully integrated 3-D microfluidic channel onto the active substrate. The advantages and disadvantages of our approach, at research level, are presented in table 1.2.

Advantages	Disadvantages
+ small	- expensive
+ portable	- complex fabrication process
+ good sensitivity	- temperature sensitivity
+ low power consumption	- self-heating (pulsed operation removes this)
+ small analyte volumes	- complex electronics
+ integrated emitter, detectors & microfluidics	
+ fast electronic reconfiguration (sub μs)	

Table 1.2: Advantages and disadvantages of our approach to an integrated microfluidic sensing mechanism.

1.2 Thesis Structure

The thesis starts (chapter 2) with some necessary background theory with respect to the context of the succeeding chapters. Chapter 3 includes an in depth discussion of the design and fabrication work that has been undertaken to develop an integrated microfluidic coupled-cavity sensor. Chapter 4 gives an account of the measurements made to determine the optical properties of InAsP/AlGaInP QD and GaInP QW materials, investigating the ideal structure to be used in the final device in chapter 6. The monolithic nature of this design requires that the laser facets of the device are created using a plasma etch process. The coupling strength, and therefore the potential sensitivity, of the device, is expected to be dependent on the efficiency of the etched facets. Therefore, etched laser facets have been characterised in terms of a facet efficiency; the results of this study are presented in chapter 5. The latter part of chapter 5, investigates angled facets as a mechanism for increasing the effective mirror loss to, theoretically, suppress the onset of free-running lasing of individual laser sections in the coupled-cavity device in the following chapter. Chapter 6 describes the characterisation and performance of a novel microfluidic coupled-cavity sensing mechanism, which is realised through developments made in the preceding chapters. Finally, chapter 7 presents the conclusion of this work and provides some suggestions for future work.

References

[1] Blausen.com staff, "Medical gallery of Blausen Medical 2014". WikiJournal of Medicine 1 (2), 2014

[2] Y. Grigoryev, *"Cell Counting with a Hemocytometer: Easy as 1, 2, 3"* https://bitesizebio.com/13687/cell-counting-with-a-hemocytometer-easy-as-1-2-3/, accessed 12/08/2018

[3] M. Absher, *"Tissue Culture: Methods and Applications"*, Chapter 1: Hemocytometer Counting, pp. 395-399, Academic Press, New York, 1973

[4] CD Creative Diagnostics, *"Flow Cytometry Guide"*, https://www.creative-diagnostics.com/flow-cytometry-guide.htm, accessed 05/04/2018

[5] H.M. Davey, *"Flow cytometric techniques for the detection of microorganisms"*, Methods Cell Sci., vol. 24, iss. 1-3, pp. 91-97, 2002

[6] X. Fan and I.M. White, *"Optofluidic Microsystems for Chemical and Biological Analysis"*, Nature Photonics, vol. 5, iss. 10, pp. 591-597, 2011

[7] J. Balsam, H.A. Bruck and A. Rasooly, "Mobile Flow Cytometry for mHealth", *Mobile Health Technologies: Methods and Protocols*, Methods in Molecular Biology, vol. 1256, pp.139-153, 2015

[8] H. Zhu and A. Ozcan, "Opto-Fluidics Based Microscopy and Flow Cytometry on a Cell Phone for Blood Analysis", *Mobile Health Technologies: Methods and Protocols*, Methods in Molecular Biology, vol. 1256, pp.171-189, 2015

[9] T.-F. Wu and Y.-H. Lo, "Optofluidic Device for Label-Free Cell Classification from Whole Blood", *Mobile Health Technologies: Methods and Protocols*, Methods in Molecular Biology, vol. 1256, pp.191-200, 2015

[10] X. Chen, D.F. Cui, C.C Liu and H. Li, *"Microfluidic chip for blood cell separation and collection based on crossflow filtration"*, Sens. and Act. B, vol. 130, pp. 216-221, 2008

[11] X. Cheng, D. Irimia, M. Dixon, K. Sekine, U. Demirci, L. Zamir, R.G. Tompkins, W. Rodriguez and M. Toner, *"A microfluidic device for practical label-free CD4+ T cell counting of HIV-infected subjects"*, Lab Chip, vol. 7, iss. 2, pp. 170-178, 2007

[12] M.T. Glynn, D.J Kinahan, J. Ducreé, *"Rapid, low-cost and instrument-free CD4+ cell counting for HIV diagnostics in resource-poor settings"*, Lab Chip, vol. 14, iss. 15, pp. 2844-2851, 2014

[13] M.D. Graham, *"The Coulter Principle: Foundation of an industry"*, J.A.L.A, vol. 8, iss. 6, pp.72-81, 2003

[14] U.D. Larsen, G. Blankenstein, J. Branebjerg, *"Microchip Coulter Particle Counter"*, Conf. Proceed. Transducers '97, pp.1319-1322, 1997

[15] D. Satake, H. Ebi, N. Oku, K. Matsuda, H. Takao, M, Ashiki and M. Ishida, *"A sensor for blood cell counter using MEMS technology"*, Sens. and Act. B: Chem., vol 83, iss. 1–3, pp.77-81, 2002

[16] U. Hassan and R. Bashir, *"Coincidence detection of heterogeneous cell populations from whole blood with coplanar electrodes in a microfluidic impedance cytometer"*, Lab Chip vol. 14, iss. 22, pp. 4370-4381, 2014

[17] J. Hu, S. Wang, L. Wang, F. Li,B. Pingguan-Murphy, T.J. Lu and F. Xu, *"Advances in paper-based point-of-care diagnostics"*, Biosens. and Bioelectron., vol. 54, pp. 585-597, 2014

[18] X. Li, K. Scida and R.M. Crooks, *"Detection of Hepatitis B Virus DNA with a Paper Electrochemical Sensor"*, Anal. Chem., vol. 87, iss. 17, pp. 9009-9015,

[19] X. Wang, G. Lin, G. Cui, X. Zhou, G.L and Liu, *"White blood cell counting on smartphone paper electrochemical sensor"*, Biosen. and Bioelectron., vol. 90, pp. 549-557, 2017

[20] M. Boyd-Moss, S. Baratchi, M. Di Venere and K. Khoshmanesh, *"Self-contained microfluidic systems: a reveiw"*, Lab Chip, 16, pp. 3177-3192, 2016

[21] M.E. Piyasena and S.W. Graves, *"The Intersection of Flow Cytometry with Microfluidics and Microfabrication"*, Lab Chip, 14, pp. 1044-1059, 2014

[22] S.-J. Kim, Y.T. Lim, H. Yang, Y.B. Shin, K. Kim, D.-S. Lee, S.H. Park and Y.T. Kim, *"Passive Microfluidic Control of Two Merging Streams by Capillarity and Relative Flow Resistance"*, Anal. Chem., vol. 77, pp. 6494-649, 2005

[23] M.S. Maria, P.E. Rakesh, T.S. Chandra and A.K. Sena, *"Capillary flow-driven microfluidic device with wettability gradient and sedimentation effects for blood plasma separation"*, Sci. Rep., vol. 7, 43457 pp. 1-12, 2017

[24] X.J. Liang, A.Q. Liu, C.S. Lim, T.C. Ayi and P.H. Yap, *"Determining refractive index of single living cell using an integrated microchip"*, Sensors and Actuators A, no. 133, pp. 349-354, 2007

[25] S. Balslev and A. Kristensen, *"Microfluidic single-mode laser using high-order Bragg grating and antiguiding segments"*, Opt. Express, vol. 13, iss. 1, pp. 344-351, 2005

[26] D. Naidu, P.M. Smowton and H.D. Summers, *"The measured dependence of the lateral ambipolar diffusion length oncarrier injection-level in Stranski-Krastanov quantum dot devices"*, Journ. Appl. Phys., 108, 043108, 2010

[27] C. Robertson and T. Gourlay, *"Development of a diagnostic sensor for measuring blood cell concentrations during haemoconcentration"*, Perfusion, vol. 32, iss. 2, pp.126–132, 2016

[28] U. Hoss and E.S. Budiman, *"Factory-Calibrated Continuous Glucose Sensors: The Science Behind the Technology"*, Diabetes Technol. Ther., vol. 19, suppl. 2, pp. S-44-S-50, 2017

[29] D.A. Cohen, J.A. Nolde, A.T. Pedretti, C.S. Wang, E.J. Skogen and L.A. Coldren, *"Sensitivity and Scattering in a Monolithic Heterodyned Laser Biochemical Sensor"*, IEEE J. Select. Top. Quantum Electon., vol. 9, pp. 1-8, 2003

[30] R. Thomas, *"Monolithic coupled-cavity laser diodes for bio-sensing applications"*, PhD Thesis, Cardiff University, 2012

[31] H.H.J. Sapingi, *"Developing coupled-cavity living laser for biological cell analysis"*, PhD thesis, Cardiff University, 2016

[32] G. Walter, J. Elkrow, N. Holonyak Jr., R.D. Heller, X.B. Zhang and R.D. Dupuis, *"Visible spectrum (645 nm) transverse electric field laser operation of InP quantum dots coupled to tensile strained $In_{0.46}Ga_{0.54}P$ quantum wells"*, Appl. Phys. Lett., vol. 84, pp. 666-668, 2004

[33] P.M. Smowton, J. Lutti, G.M. Lewis, A.B. Kyrsa, J.S. Roberts and P.A. Houston, *"InP-GaInP quantum-dot laser emitting between 690-750 nm"*, IEEE J. Sel. Top. Quant. Electron., vol. 11, no. 5, pp. 1035-1040, 2005

[34] Y. Qiu, A.B. Kyrsa and T. Walther, *"STEM imagining of InP/AlGaInP quantum dots"*, J. Phys. Conf. Ser., vol. 245, 012087, 2010

[35] A. Roggan, M. Friebel, K. Dörschel, A. Hahn and G. Müller *"Optical Properties of Circulating Human Blood in the Wavelength Range 400-2500 mn"*, Journ. of Biomed. Opt., vol. 4, no. 1, pp.36–46, 1999

[36] N. Bashkatov, E.A. Genina, V.I. Kochubey and V.V. Tuchin, *"Optical properties of human skin, subcutaneous and mucous tissues in the wavelength range from 400 to 2000 nm"*, J. Phys. D: Appl. Phys, vol. 38, pp. 2543–2555, 2005

[37] A.B. Kyrsa, J.S. Roberts, J. Devenson, R. Beanland, I. Karomi, S. Shutts and P.M. Smowton, *"InAsP/AlGaInP/GaAs QD laser operating at ∼770nm"*, J. Phys. Conf. Ser., vol. 740, 012008, 2016

[38] S. Shutts, S. Elliott, P.M. Smowton and A.B. Krysa, *"Exploring the wavelength range of InP/AlGaInP QDs and application to dual-state lasing"*, Semicon. Sci. Techno., vol. 30, iss. 4, 044002, 2015

[39] A. Zourabian, A. Siegel, B. Chance, N. Ramanujan, M. Rode and D.A. Boas, *"Trans-abdominal monitoring of fetal arterial blood oxygenation using pulse oximetry"*, J. Biomed. Opt., vol. 5, iss. 4, pp. 391-405, 2000

[40] J. Qin, R. Reif, Z. Zhi, S. Dziennis and R. Wang, *"Hemodynamic and morphological vasculature response to a burn monitored using a combined dual-wavelength laser speckle and optical microangiography imaging system"*, Biomed. Opt. Exp., vol. 3, iss. 3, pp. 455–466, 2012

[41] R. Thomas, D. Briglin, A.B. Krysa, P.M. Smowton, *"Mechanism for enhanced wavelength tuning in gain-levered InP quantum dot lasers"*, IET Optoelectron., vol. 10, iss. 2, pp. 66-69, 2015

[42] D. Choi, R. Yoshimura and K. Ohbayashi, *"Tuning of successively scanned two monolithic Vernier-tuned lasers and selective data sampling in optical comb swept source optical coherence tomography"*, Biomed. Opt. Exp., vol. 4, no. 12, pp. 2962-2987, 2013

[43] K. Numata, J.R. Chen and S.T. Wu, *"Precision and fast wavelength tuning of a dynamically phase-locked widely-tunable laser"*, Opt. Exp., vol. 20, no. 13, pp. 14234-14243

Chapter 2

Background Theory

2.1 Introduction

This chapter serves to explain the majority of topics covered in the following chapters of this thesis. It covers the fundamentals of laser diodes and how lasing action is achieved. Later in the chapter, there is a brief description of the semiconductor laser structures using quantum confinement (achieved by both quantum wells and quantum dots) that have been used in this work. The final part of this chapter discusses the mechanisms and physics behind a coupled-cavity laser.

2.2 Fundamentals of a Laser Diode

This section provides an overview of the fundamental components of diode lasers, seen in figure 2.1. These include the semiconductor gain medium that is responsible for the coherent amplification of light, the resonator that maintains a coherent lasing output and the characteristics of a p-n junction under electrical pumping.

2.2.1 Gain Medium

The diode laser design incorporates a gain medium into the resonant optical cavity. The gain medium is a critical component of a laser because it amplifies the incident radiation. Amplification rather that absorption is achieved by pumping the medium, either electrically or optically. The input of energy to the material excites electrons to a higher energy state and the amplification of the initial electrons causes a de-excitation of these higher energy electrons. The gain in light intensity is necessary in order to overcome the losses generated by the resonant cavity and for

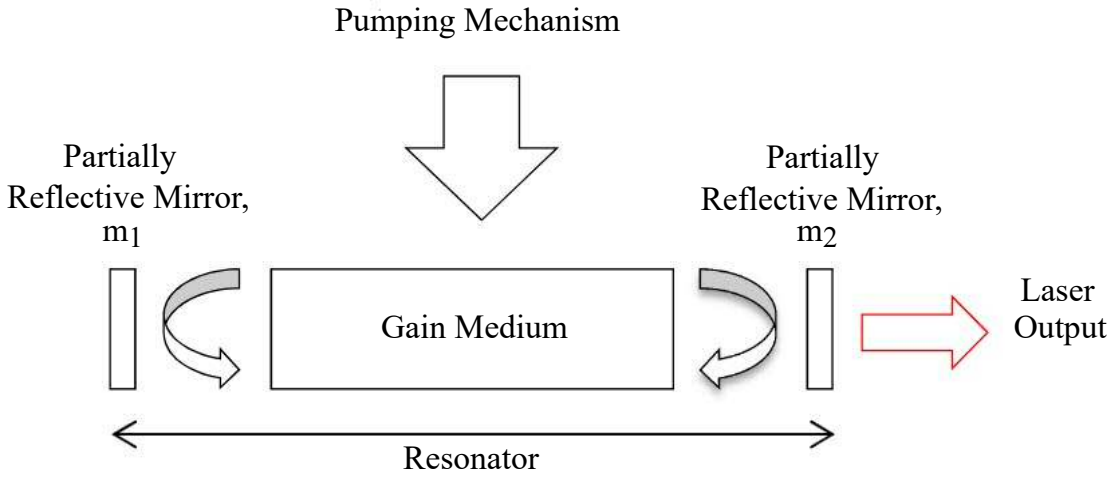

Figure 2.1: Schema of the basic components of a laser diode.

there to be any laser output [1].

Diode lasers have a gain medium that is usually made from a diamond-type lattice semiconductor. As isolated atoms are brought together, the electron wave functions begin to overlap. The solid is then formed when the discrete energy levels of individual atoms split into bands of levels (figure 2.2). This splitting is due to the outer valence electrons of one atom being allowed to be in two different states; bonding or anti-bonding [1]. The splitting of the uppermost-occupied energy level

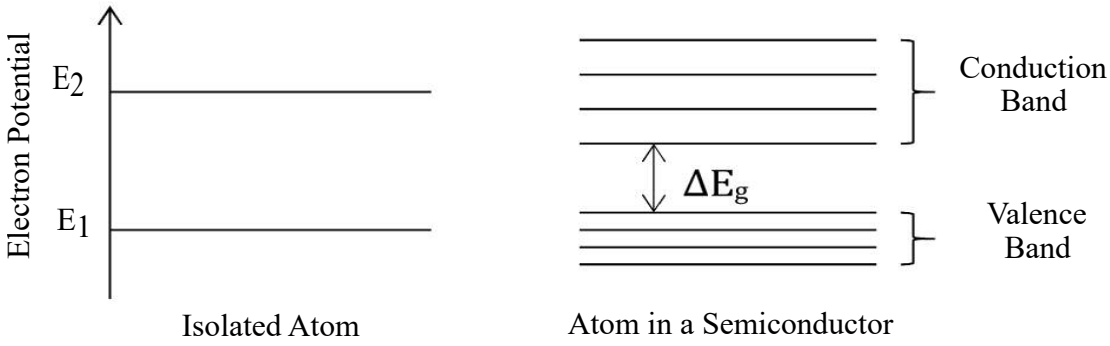

Figure 2.2: Splitting of discrete isolated atom energy levels into energy bands in a solid.

forms the valence band (VB) with a separation to the next energy level of E_g. The VB is completely filled even if there is no external field applied to it. The next uppermost energy level splits into the conduction band (CB). This level, unlike the VB, is completely empty in a semiconductor material. When an external field is applied, the gap between the VB and CB is small enough that, a small number of high-energy electrons can be excited from the VB to the CB, creating holes

in the VB. By definition in the case of a direct band-gap semiconductor, as in figure 2.3, the CB

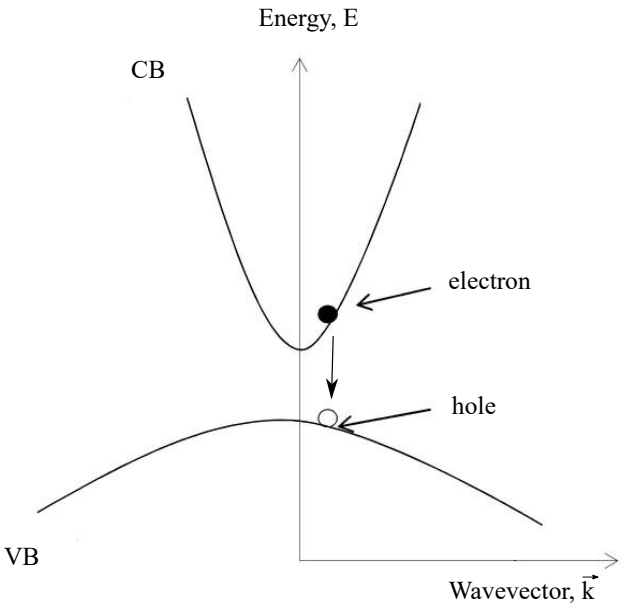

Figure 2.3: Energy versus wave vector band diagram of a direct band-gap semiconductor showing the conduction band (CB) and valence band (VB) and the radiative recombination of an electron and a hole.

minimum and VB maximum occur at the same wave vector value. Interacting photons carry negligible momentum and therefore a radiative transition between these two energy bands must occur at the same wave vector due to conservation of momentum. There must also be conservation of energy, and for a transition between two energy states, E_1 and E_2, the energy of the transition must be equal to the energy of the resulting photon with frequency ν,

$$E_2 - E_1 = h\nu \tag{2.1}$$

where h is Planck's constant (6.626 x 10^{-34} m^2kgs^{-1}).

2.2.1.1 Einstein coefficients

Within semiconductors, there are three radiative recombination processes, which are shown in figure 2.4, that involve the absorption and emission of photons. Figure 2.4(a) has an electron with energy, E_2, that falls spontaneously to the lower, empty energy state, E_1. This transition emits a photon of energy $h\nu$. If there are N atoms with energy E_2, the total population, N_2, will decrease after each spontaneous emission event. The rate of decay of the number of atoms with an electron

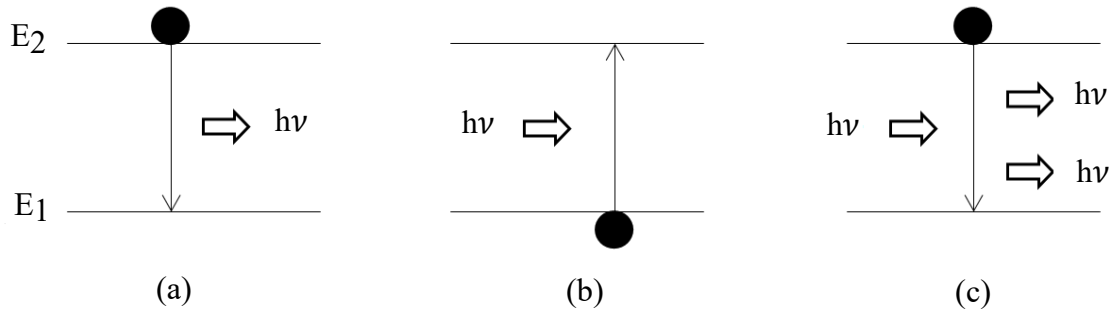

Figure 2.4: Illustration of the three radiative transitions between energy bands in a two-level system, (a) spontaneous emission, (b) absorption and (c) stimulated emission. Energy to excite or de-excite an electron is either provided by an electron or supplied to it.

of energy, E_2 can be expressed as [2]

$$\frac{dN_2}{dt} = -A_{21}N_2 \tag{2.2}$$

where A_{21} is the probability per unit time of a spontaneous event occurring.

Absorption, depicted in 2.4(b), has an electron in the lower state, that when supplied with energy, $h\nu$, it may be excited up to the excited state. In this case, there are N_1 atoms with electrons in the lower state and therefore the rate of decrease of N_1 due to all upward transitions,described by the coefficient $B_{12}^{h\nu}$ [i] is

$$\frac{dN_1}{dt} = -B_{12}^{h\nu}N_1\rho(h\nu) \tag{2.3}$$

where $\rho(h\nu)$ is the spectral photon density. This is the number of photons of energy $h\nu$ per unit volume per unit energy interval. Figure 2.4(c) shows that an incoming photon, of frequency ν and energy $h\nu$, can stimulate an electron to make a transition. This transition occurs between the excited state and an empty lower energy state, producing a photon of energy $h\nu$ to conserve energy. The emitted photon has a range of energies similar to that of the stimulating photon. Therefore, this additional photon also has the same phase and direction of travel, i.e. is coherent. In this instance, the rate of decay of N_2 by stimulated emission is

$$\frac{dN_2}{dt} = -B_{21}^{h\nu}N_2\rho(h\nu) \tag{2.4}$$

[i] $B_{12}^{h\nu}$ has the dimensions [energy]$[T]^{-1}[L]^3$

In a steady state system, the rate of all downward transitions must be equal to all upward transitions. The rate at which N_2 increases through absorption processes is the same at which atoms are lost from N_1, so by combining equations 2.2, 2.3 and 2.4, the condition for steady-state in N_2 becomes

$$\frac{dN_2}{dt} = -A_{21}N_2 - B_{21}^{h\nu}N_2\rho(h\nu) + B_{12}^{h\nu}N_1\rho(h\nu) = 0 \tag{2.5}$$

which rearranges to give

$$\rho(h\nu) = \frac{A_{21}/B_{21}^{h\nu}}{(N_1/N_2)(B_{12}^{h\nu}/B_{21}^{h\nu}) - 1} \tag{2.6}$$

Comparing equation 2.6 to the Planck law for photon density,

$$\rho(h\nu) = \rho_{mode}(h\nu)\left[\frac{1}{exp\left(\frac{h\nu}{k_BT}\right) - 1}\right] \tag{2.7}$$

shows that

$$B_{21}^{h\nu} = B_{12}^{h\nu} \tag{2.8}$$

and the coefficient for spontaneous emission, A_{21}, is related to the B coefficients for induced upward transitions via $\rho_{mode}(h\nu)$, the mode density,

$$A_{21} = \rho_{mode}(h\nu)B_{21}^{h\nu} \tag{2.9}$$

where

$$\rho_{mode}(h\nu) = \frac{8\pi n^3}{h^3c^3}(h\nu)^2 \tag{2.10}$$

2.2.1.2 Population Inversion

In thermal equilibrium the electrons and holes share a Fermi energy close to the middle of the band gap. The electron occupation probability of all CB and VB states at a temperature T can be described by Fermi statistics as

$$f(E) = \frac{1}{1 + \exp(\frac{E - E_F}{k_BT})} \tag{2.11}$$

where E_F is the Fermi energy. Since $E_g >> k_BT$, there is a vast number of electrons in the VB compared to the CB. However, net gain is only produced when the probability of the upper level, f_2, is greater than that of the lower level, f_1. This requires the populations of the CB and VB states to be inverted. This can be described in terms of Fermi functions, through substitution into the

condition $f_2 > f_1$, as

$$E_{F_2} - E_{F_1} > E_2 - E_1 \tag{2.12}$$

which can be rewritten as [3]

$$\Delta E_F > h\nu \tag{2.13}$$

where the energy between states is equal to $h\nu$, the photon energy. This expression is known as the "Bernard and Duraffourg condition" and states that for population inversion to occur, the quasi-Fermi level separation must be larger than the photon energy. This population inversion can be maintained by injecting carriers into the semiconductor material through a p-n junction.

2.2.2 p-n Junctions

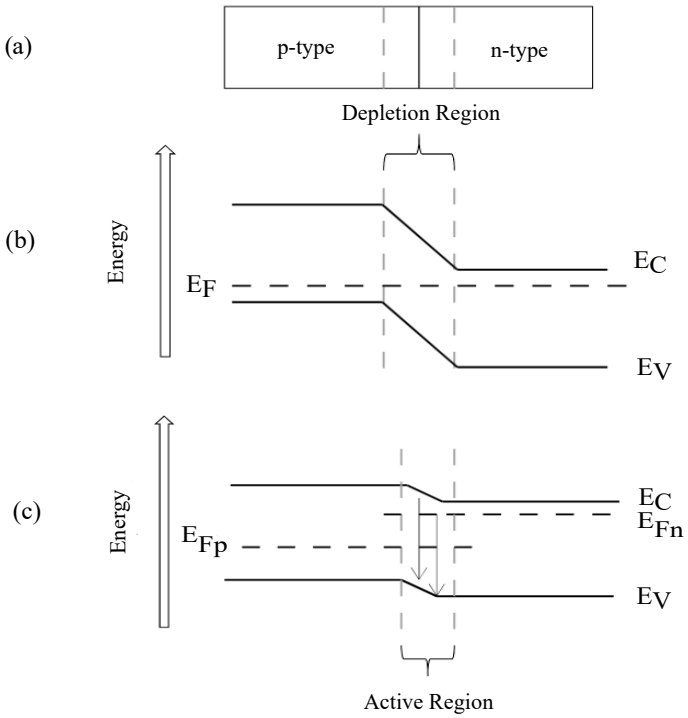

Figure 2.5: Illustration of p-n junction showing the junction of two materials (a) and the energy band diagram for a p-n junction (b) in equilibrium with the depletion region and (c) under forward bias with the active region.

A laser diode operates with the principle of electrical pumping applied to the junction where a p- and n-type material meets, in order for the gain medium to function. The intrinsic semiconductor used to create p- and n-type material is doped with acceptor and donor impurities respectively. For n-type, the Fermi level is close to the bottom of the CB and the donor impurities can donate

electrons to the CB. On the other side, the p-type Fermi level is close to the top of the VB and the acceptor impurities are able to accept holes from the VB. At first, when the two materials are brought into contact with each other, excess electrons diffuse from the n- to the p-type and holes vice versa. On each side of the junction, these excess electrons and holes annihilate each other leaving positively charged donors on the p-material side and negatively charged acceptors on the n-side. These charged donors and acceptors set up an electric field between the two sides, which creates a flow of charge in the opposite direction to that due to diffusion. Equilibrium is reached when diffusion is equal to the drift of carriers in the opposite direction. This creates a charge free region at the junction, called the depletion region. The energy band diagram in figure 2.5 has a potential barrier caused by this depletion region and acts as a barrier to effectively stop carriers diffusing from one side to the other. In equilibrium, this has the effect of bringing the Fermi level of each material to the same value. However, when a forward bias is applied, positive to the p-side and negative to the n-side, electrons are injected from the n-type layer into the active region and holes are injected from the p-type layer into the active region. The active region is defined as '*the region where recombining carriers contribute to useful gain and photon emission*' [1]. The energy band diagram illustrated in figure 2.5(c) shows an increase in the energy of the bottom of the CB on the n-side, but a decrease on the p-side, resulting in the potential barrier in the active region decreasing. Electrons and holes can now diffuse into this region and radiatively combine to produce photons. These photons are released with energy of $h\nu \cong E_g$. Population inversion is achieved when the rate of carrier injection exceeds a critical value and so the rate creates net stimulated emission [4].

2.3 Longitudinal Cavity Modes and Threshold Conditions

Considering the semiconductor diode laser shown in figure 2.1, the thin central region of the gain medium is the active region and the two partially reflecting mirrors provide optical feedback for amplification of light along the cavity. The plane wave approximation for the electrical field of a mode in the cavity is given by,

$$E = E_0 \exp(i\vec{\beta} y) \tag{2.14}$$

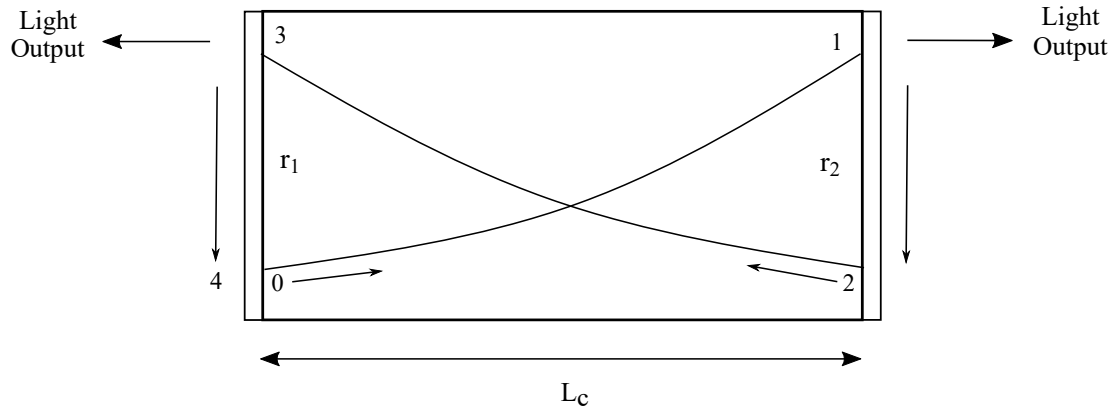

Figure 2.6: Schematic of the sustained coherent round-trip condition for laser action where the net gain over each pass of the cavity equates to the light lost at the mirrors.

if the y-direction is taken along the length of the cavity. Here, $\vec{\beta}$, the propagation constant is of the form,

$$\vec{\beta} = \frac{2\pi n}{\lambda_0} + \frac{i\alpha}{2} \tag{2.15}$$

where n is the group refractive index of the medium, α is the net absorption coefficient and λ_0 is the wavelength of light in a vacuum. The net absorption coefficient is a collective term to account for the modal gain of the material from absorption and pumping mechanism and also the internal losses that occur in semiconductor lasers, caused in most part to free carrier absorption. This coefficient can then be written in terms of modal gain, G and internal losses, α_i,

$$\alpha = -G + \alpha_i \tag{2.16}$$

Equation 2.14 indicates the electrical field oscillating in the gain medium increases exponentially along the cavity length. When the situation arises of the modal gain being greater than the sum of the losses, the optical field will increase after each round trip. However, as the intensity of the field increases, the level of the inverted carrier population starts to decrease. This has the effect of reducing the round trip amplification and the amount of light in the cavity. If however, a constant external pumping mechanism is applied to the gain medium, population inversion is quickly re-established. After several oscillations of this, the system then operates under steady-state conditions and the net change in amplitude of the electrical field after one complete round trip, where the reflection coefficient of each facet is r_1 and r_2 respectively, of the cavity is equal to 1. Figure 2.6 shows the condition for laser action, which can be described theoretically as

$$(r_1 r_2) \exp\left[2i\left(\frac{2\pi n}{\lambda} - \frac{i(G-\alpha_i)}{2}\right)L\right] = 1 \tag{2.17}$$

By using Euler's identity, the real and imaginary parts of equation 2.17 can be separated,

$$(r_1 r_2) \exp\left[(G-\alpha_i)L\right]\left[\cos\frac{2\pi nL}{\lambda}\right] = 1 \tag{2.18}$$

$$(r_1 r_2) \exp\left[(G-\alpha_i)L\right]\left[i\sin\frac{2\pi nL}{\lambda}\right] = 0 \tag{2.19}$$

Equation 2.19 is satisfied when

$$2\left(\frac{2\pi n}{\lambda_m}\right)L = 2m\pi \tag{2.20}$$

$$\lambda_m = \frac{2nL}{m} \tag{2.21}$$

where m is an integer. The multiple solutions of the condition in equation 2.20 give the wavelengths of the longitudinal modes λ_m in the cavity. Solving equation 2.18 for G,

$$G = \frac{1}{L}\ln\frac{1}{r_1 r_2} + \alpha_i \tag{2.22}$$

Equation 2.22 is more commonly written in terms of reflectivity instead of amplitude coefficients, and using the relationship $R = r^2$ it becomes

$$G_{th} = \frac{1}{2L}\ln\frac{1}{R_1 R_2} + \alpha_i \tag{2.23}$$

The first term in equation 2.23 is the mirror loss and is the fraction of light that is lost purely due to the facet reflectivity. This however, can only be seen as an approximation as the effect of spontaneous emission has been ignored, but it shows the modal gain of a laser diode is dependent on its resonator length.

2.3.1 Resonator

In the case of a diode laser, the two plane parallel mirrors, one at each end of the gain medium, make this a Fabry-Perot resonator. These two partially reflective parallel mirrors are formed, most simply, by cleaving along crystal planes, usually $\{011\}$ [4]. If light is at a normal incidence to the

mirror, the reflectance at one semiconductor-air interface, R, is given by [6],

$$R = \left(\frac{n_{sc} - n_{air}}{n_{sc} + n_{air}} \right)^2 \tag{2.24}$$

where n_{sc} is the refractive index of the semiconductor and n_{air} is the refractive index of air (n_{air} = 1). Only light perfectly perpendicular to the axis of the cavity will be propagated back and forth inside the cavity. The refractive indices in this equation can be interchanged with those of other materials depending on the type of interface involved.

2.4 Semiconductor Laser Structure

All the experimental devices in this thesis have been fabricated from either III-V multi quantum well (MQW) or 5 layer quantum dot (QD) semiconductor material. This section provides a short background to these specific types of laser structures and the related double heterostructure.

2.4.1 The Double Heterostructure

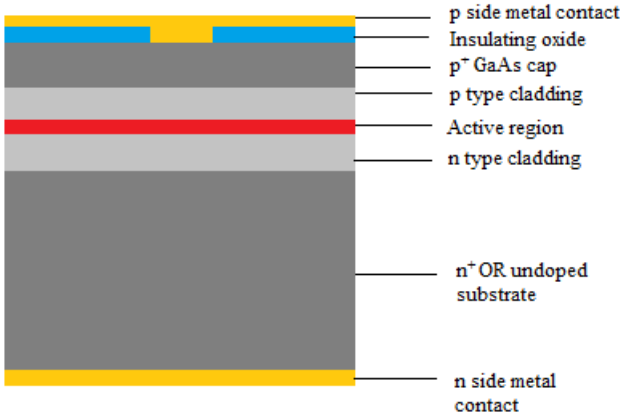

Figure 2.7: Diagram of the layer structure in a gain-guided double heterostructure semiconductor laser.

The p-n junction described in section 2.2.2 consists of a junction with the same material with different doping levels on each side. This is known as a p-n homojunction. The disadvantage to using a homojunction is that the active region is very wide ($\approx$0.01 μm) due to the lack of carrier confinement [5]. A way to improve this is to use a p-n heterostructure. Figure 2.8 shows the energy band diagram of a double heterostructure where the active region material has a smaller energy band gap and higher refractive index than each of the p- or n-type cladding layers either

side.

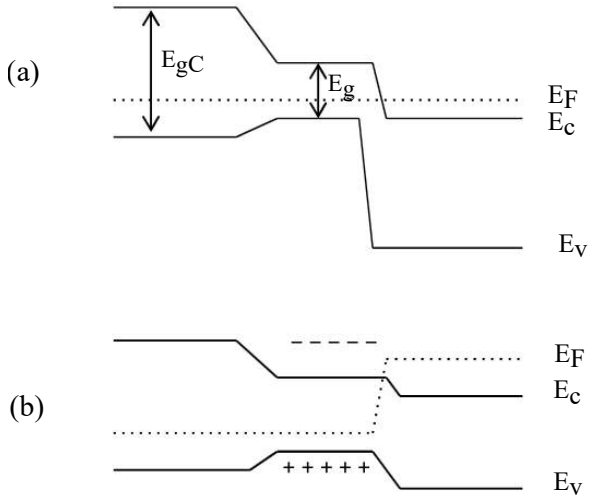

Figure 2.8: The energy band diagram of a double heterostructure semiconductor laser at (a) zero bias and (b) forward bias, with the energy band gap of the active region, E_g, and cladding layers, E_{gC}, indicated.

2.4.2 Slab Waveguide Design

A symmetric three layer slab dielectric waveguide consists of three different material layers, schematically shown in figure 2.9; layers 1 and 3 are n- and p-cladding of some semi-finite thickness with refractive index n_1. Layer 2 is the waveguide core, the thin central region of height d and refractive index n_2, surrounded by layers 1 and 3. For total internal reflection to occur at each interface, $n_2 > n_1$ and guiding within the active region occurs when the height, d, is approximately equal to the wavelength of light in the material. This is due to the electric field has its highest intensity in the centre of the layer, as shown by the intensity profile in figure 2.9. This design confines the plane wave to its starting incident angle and forces the wave to oscillate back and forth along the cavity. Each reflection off alternate interfaces has the same incident and reflection angle that allows other waves propagating in the same direction and of the same phase to be added together in phase.

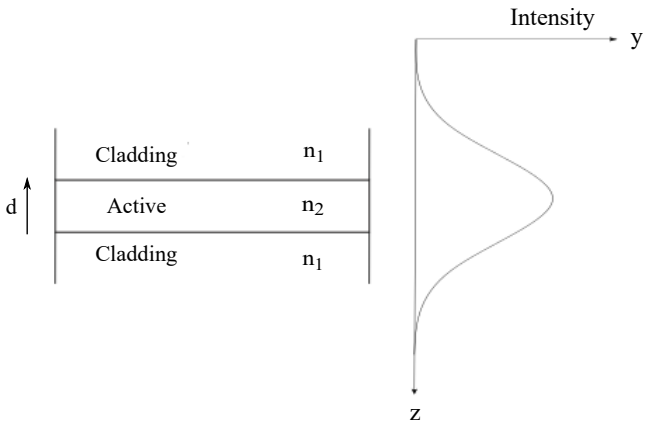

Figure 2.9: Illustration of a slab waveguide design in a semiconductor laser. The refractive indices are such that $n_2 > n_1$. Also shown is the intensity distribution of the fundamental mode as a function of distance, z.

2.5 Quantum Confinement

2.5.1 Quantum Wells

A QW is formed by a very thin layer of material where the thickness is comparable to the de Broglie wavelength of the carriers (≈10 nm) and is of a narrow-gap material between two layers of wide-gap material [2][7]. This in effect forms a potential well that restricts the motion of carriers. In this instance quantum confinement occurs in just one spatial dimension, in the z direction which reduces the number of available states to a set of discrete energy levels as seen in figure 2.10.

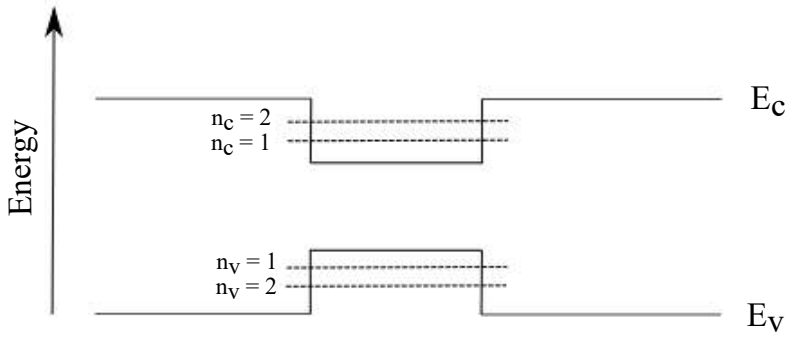

Figure 2.10: Schematic energy band diagram of the conduction and valence bands of a QW formed from layer of narrow-gap material in the centre with a wide-gap barrier either side. Also illustrated are a set of discrete energy levels.

2.5.1.1 The Finite Potential Well

Solving Schrödinger's time-independent equation for the case of an infinite potential well is not realistic for a quantum well, as electrons and holes can tunnel into the barrier. Therefore, the case where the wave-function extends into the barrier regions, as depicted in figure 2.11, must be considered. A quantum well with a finite barrier height of V_0 can be described by

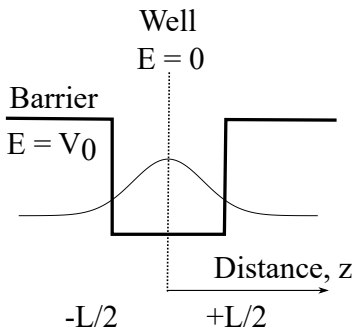

Figure 2.11: A finite potential well of depth $E = V_0$ and width L, and the wave-function of the lowest confined state.

$$-\frac{\hbar^2}{2m^*}\frac{d^2\Psi(z)}{dz^2} + V(z)\Psi(z) = E\Psi(z) \tag{2.25}$$

where the potential $V(z) = V_0$ in the barrier regions and $V(z) = 0$ in the well, m^* is the effective mass of the particle, Ψ is the particle wave-function and E is the energy. The wave-function solution of equation 2.25 for a particle in the barrier region are of the form

$$\Psi_b(z) = B\exp(\pm\kappa z) \tag{2.26}$$

The solutions of equation 2.25 for the well region can be expressed as

$$\Psi_n(z) = A\cos k_z(z) \qquad \text{when n is odd} \tag{2.27}$$

$$\Psi_n(z) = A\sin k_z(z) \qquad \text{when n is even} \tag{2.28}$$

where n is the quantum number and the wave numbers, k_z and κ_z satisfy

$$k_z = \left[\frac{2m_w^* E}{\hbar^2}\right]^{\frac{1}{2}} \tag{2.29}$$

$$\kappa_z = \left[\frac{2m_b^*(V_0 - E)}{\hbar^2}\right]^{\frac{1}{2}} \tag{2.30}$$

Here m_w^* and m_b^* represent the effective mass of the particle in the well and barrier regions respectively.

The wave-function and energies of the bound states in a quantum well can be found by applying the following boundary conditions,

$$\Psi_w(z) = \Psi_b(z) \tag{2.31}$$

$$\frac{1}{m_w^*}\left(\frac{d\Psi_w}{dz}\right) = \frac{1}{m_b^*}\left(\frac{d\Psi_b}{dz}\right) \tag{2.32}$$

i.e. the wave function, $\Psi(z)$ and particle flux, $\frac{1}{m^*}\left(\frac{d\Psi}{dz}\right)$ must be continuous at the interface between quantum well and barrier regions. For a quantum well of width L (as in figure 2.11), applying equations 2.31 and 2.32 to equations 2.27 and 2.28, results in

$$\tan\left(k_z\frac{L}{2}\right) = \frac{m_w^*\kappa}{m_b^*k} \qquad \text{when n is odd} \tag{2.33}$$

$$\tan\left(k_z\frac{L}{2}\right) = -\frac{m_b^*k}{m_w^*\kappa} \qquad \text{when n is even} \tag{2.34}$$

Equations 2.33 and 2.34 do not have analytic solutions and therefore solutions for E must be solved numerically or by graphical analysis. Due to spatial confinement in the z-direction, only k_z is quantised and particles are free to move in the plane of the well (x, y) [8]. This means that there are a range of solutions k_x and k_y can take. By separating Schrödinger's equation for each of the component wave-functions, the energy states in a QW are given by [2]

$$E = E_{xy} + E_z = \frac{\hbar^2|\mathbf{k}_{xy}|^2}{2m_w^*} + E_z \tag{2.35}$$

where E is the total energy of the particle and

$$|\mathbf{k}_{xy}|^2 = k_x^2 + k_y^2 \tag{2.36}$$

2.5.1.2 Density of States

As seen in equation 2.35, there is a large number of degenerate states with different values of k_x and k_y but the same value of $|\mathbf{k}_{xy}|$ and E_{xy}. Due to the relationship in equation 2.36, all of these states lie on a circle in the (k_x, k_y) plane with radius $|\mathbf{k}_{xy}|$. Born-von Kármán boundary conditions

can be applied to travelling wave representation of the electron motion in the plane. These cyclical boundary conditions require an integer number of wavelengths in the circumference of the circle that give allowed values of the k-vector, k, for each direction,

$$k = \pm n\left(\frac{2\pi}{L}\right) \tag{2.37}$$

and therefore the spacing of the allowed values of k_x and k_y is given by

$$dk_x = \frac{2\pi}{L_x} \qquad \text{and} \qquad dk_y = \frac{2\pi}{L_y} \tag{2.38}$$

With this restriction in k-space, only certain values of k lead to acceptable electron wave-function solutions. Each state therefore occupies an area in k-space of

$$V_{2D} = \left(\frac{4\pi^2}{L_x L_y}\right) \tag{2.39}$$

The k-space area of the annulus, depicted in figure 2.12, divided by the k-space area of each state

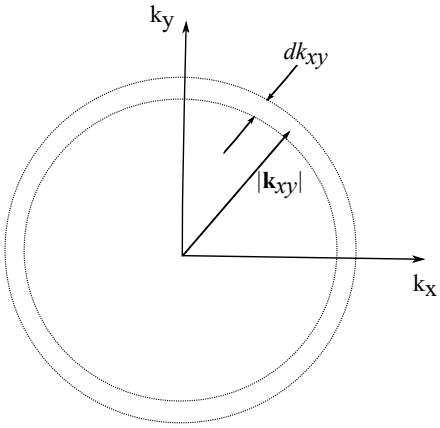

Figure 2.12: k-space diagram of allowed states associated with travelling wave representation of the in-plane motion of electrons. A number of different states have the same energy lying on a circle in the (k_x, k_y) plane. The number of available states lie in a thin annulus of radius, $|\mathbf{k}_{xy}|$ and width, dk_{xy}.

(equation 2.39) results in an expression for the number of states with energy E_{xy},

$$N_{xy} = \frac{2\pi|\mathbf{k}_{xy}|dk_{xy}}{4\pi^2/L_x L_y} \tag{2.40}$$

Expressing equation 2.40 in terms of energy leads to

$$N_{xy} = \frac{m_w^*}{2\pi\hbar^2}(L_x L_y)dE_{xy} \tag{2.41}$$

Therefore the number of states in energy E_{xy} per unit area per unit energy, $\rho(E)$, is

$$\rho(E) = \frac{m_w^*}{\pi\hbar^2} \tag{2.42}$$

Equation 2.42 above is the density of states in one sub-band for both spins and can be seen to be independent of energy. If this is then summed over all available sub-bands, a step-like function is produced as in figure 2.13 (b). As such, there are a significant amount of states immediately available. This contrasts with the density of states of a bulk semiconductor material, which is proportional to $E^{1/2}$ (figure 2.13 (a)).

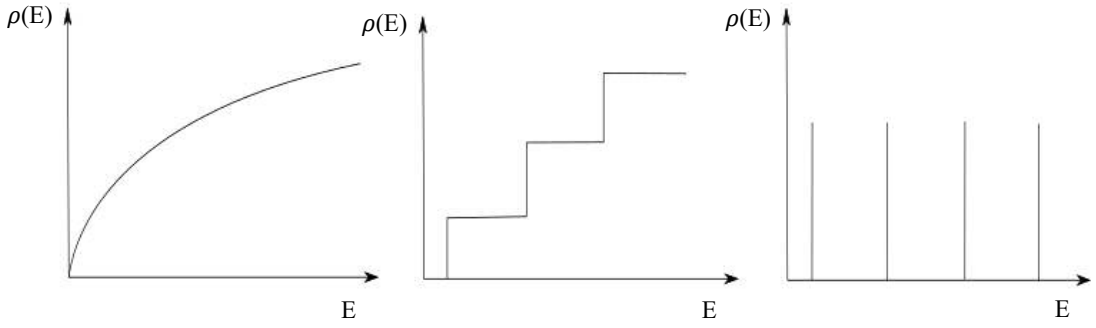

Figure 2.13: Diagram showing the density of states for (a) bulk semiconductor material with no confinement in any direction, (b) a finite QW with confinement in one direction, z and (c) a QD with confinement in all three directions, x,y,z .

2.5.2 Quantum Dots

Unlike QWs, a QD has its carriers confined to all three spatial directions, x,y,z. The confinement changes the allowed energy states and all available states occur only at discrete energies, therefore the density of states function becomes,

$$\rho(E) \propto \delta(E) \tag{2.43}$$

Theoretically the density of states is a series of delta-functions, however realistically, a distribution of dot sizes means these delta functions exist over a range of energies and homogeneously broaden

due to Coulomb interactions, causing a finite linewidth of each individual delta function.

2.6 Coupled-Cavity Lasers

Coupled-cavity (C-C) lasers have been the subject of extensive work in the past [11], [12], [13] in relation to their properties such as longitudinal mode-selectivity, electronic controllability and capability of providing spectral control. Much of the theoretical analysis of C-C semiconductor lasers was focused on establishing optimal performance through device design [14]. It was found that parameters such as gap length, l_g, and the ratio of the cavity lengths, l_1 and l_2, influenced mode selection and threshold gain of the device. However, a C-C laser is proposed in this work for use as a novel sensing mechanism for detection of WBCs, increase the sensitivity and range of optical parameters measured. The next sections cover the principles of coupling between sections of and longitudinal modes in a C-C laser and how a C-C may be used as a sensing mechanism.

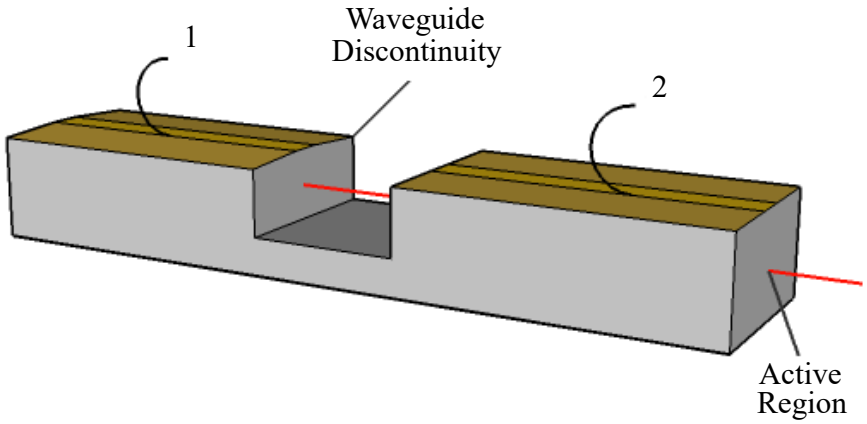

Figure 2.14: Schematic of a two section coupled-cavity laser, L_1+L_2, where $l_1 \approx l_2$.

2.6.1 The Coupling Constant

A maximum amount of coupling occurs when the gap length is of the order of the lasing wavelength [15]. This air gap forms a third Fabry-Pérot cavity, and the inter-cavity coupling of light between the two cavities is affected by the loss and phase shift of the field whilst in the gap. The scattering matrix approach [16] can be used to determine the transmission and reflection of the electric fields, E_1 and E_2 as in figure 2.15. The reflectivity coefficients r_1, $r_1^{'}$, r_2 and $r_2^{'}$ correspond

to that of cavity 1 and cavity 2 respectively. In the general case, the amplitude coefficients at the four facets may differ from one another.

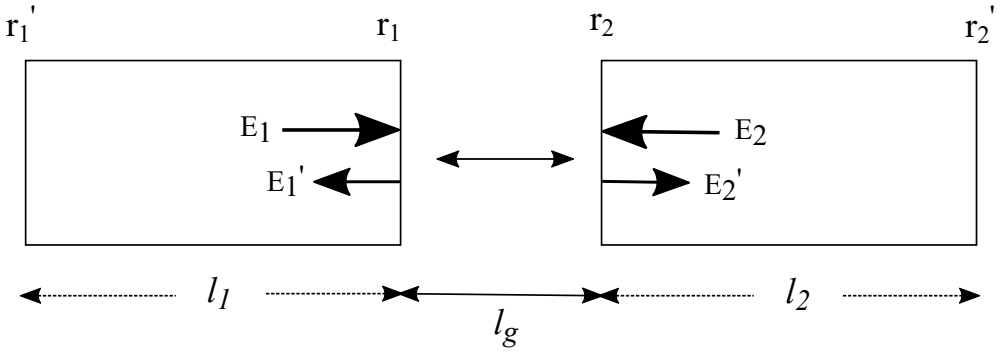

Figure 2.15: Geometry and notation used in the theoretical description of the coupling between two cavities of a coupled-cavity semiconductor laser via multiple round trips.

The electric fields in the two cavities are related by,

$$\begin{Bmatrix} E_1' \\ E_2' \end{Bmatrix} = \begin{Bmatrix} S_{11} & S_{12} \\ S_{21} & S_{22} \end{Bmatrix} \begin{Bmatrix} E_1 \\ E_2 \end{Bmatrix} \tag{2.44}$$

The reflection and transmission matrix elements can be obtained by considering the reflection and transmission of the electric field after multiple round trips inside the cavity and gap. Assuming the device is symmetrical, i.e. $r_1 = r_2 = r$, the result respectively is,

$$S_{11} = S_{22} = r - \frac{r(1-r^2)t_g}{1-r^2 t_g} \tag{2.45}$$

$$S_{12} = S_{21} = \frac{[t_g(1-r^2)^2]^{1/2}}{1-r^2 t_g} \tag{2.46}$$

where t_g is the single pass cavity transmission factor that describes the phase propagation and loss inside the gap. It is given by,

$$t_g = \exp(2ik_0 l_g)\exp(-\alpha_g l_g) \tag{2.47}$$

in which

$$k_0 = \frac{2\pi}{\lambda_g} \tag{2.48}$$

where λ_g is the wavelength of the lasing light inside the gap. The magnitude, C, and phase, ϕ, of the coupling between cavities can be defined by as the ratio of the complex reflection and

transmission coefficients complex coupling parameter;

$$\frac{S_{12}}{S_{11}} = C\exp(i\phi) \tag{2.49}$$

2.6.2 Coupled-Cavity Longitudinal Modes

Mode selectivity in a C-C laser is dominated by the diffraction losses in the gap between the two cavities. For a specific C-C mode to lase, the condition of simultaneous cavity resonances must be met. However, the wavelength of this mode must also correspond to the phase condition described in equation 2.49. A threshold gain condition associated with a C-C laser, as in figure 2.14, can be found by considering both the gain and loss of the whole system. By considering the relationship between the fields E_1 and $E_1^{'}$, as depicted in figure 2.15, the field $E_1^{'}$ at the gap is the result of the reflection of E_1 and transmission of E_2. Using equation 2.44,

$$E_1^{'} = S_{11}E_1 + S_{12}E_2 \tag{2.50}$$

Also, the round trip through cavity 1 results in

$$E_1 = r_1^{'}\exp(2i\beta_1 l_1)E_1^{'} = r_1^{'}t_1E_1^{'} \tag{2.51}$$

Applying the round trip condition imposed in equation 2.17 yields the eigenvalue equation

$$(1 - r_1^{'}t_1S_{11})(1 - r_2^{'}t_2S_{22}) = r_1^{'}r_2^{'}t_1t_2S_{12}S_{21} \tag{2.52}$$

where t_1 and t_2 are the single pass transmission factors that describe the phase propagation and loss of the field in cavities 1 and 2 respectively, and is given by

$$t_n = \exp\left(2i\left(\frac{2\pi}{\lambda_0}\right)n_n l_n\right)\exp(G_n l_n) \tag{2.53}$$

where n_n, l_n and G_n are the refractive index, length and modal gain of cavity n respectively. With increasing injected current, carrier concentration and refractive index change above threshold in C-C lasers, shifting one set of modes with respect to the other. In comparison, these quantities are pinned above threshold in single-cavity lasers. A lasing C-C laser has its carrier density linked to the current density in each cavity and the optical coupling between each cavity. If the current

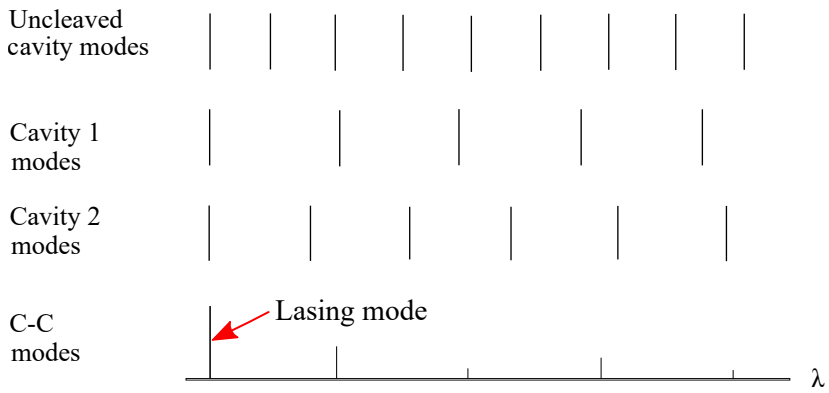

Figure 2.16: Schematic of cavity modes and relative intensities of a C-C laser with unequal cavity lengths ($l_1 > l_2$).

density in cavity 1 is increased then the rate at which photons pass into cavity 2 will increase. This causes an increased rate of stimulated emission in cavity 2, thereby suppressing the gain in the cavity. To continue lasing on the C-C mode, the net gain condition must still be met and in order to achieve this, the carrier density in cavity 1 must increase. As a result of this, C-C lasers with unequal cavity lengths provides a mechanism for wavelength tuning and mode discrimination [17, 18], as depicted in figure 2.16.

2.6.3 Operation

Our approach, to increase sensitivity and resolution, will use a C-C semiconductor laser, through which the blood cells flow. The cells become an active element of the laser cavity and therefore strongly influence the cavity gain characteristic. Cytometric signal transduction will be by a novel process of intra-cavity absorption and scattering in a regenerative (gain compensating losses) lasing process. The greater interaction with the cell makes cell discrimination easier and reduces measurement time. Measurements of the scattering cross section of a single red blood cell [19] indicate that the presence or absence of the cell can change the optical loss of a QW or QD laser operated on the saturated region of the gain-current characteristic and turn the laser on or off, or change the output power. This is depicted in figure 2.17, where the gain requirement, and subsequent threshold current density, of a C-C is shown by the dashed blue line. A passing cell between the two sections of the C-C, perturbs the gap scattering losses and increasing the overall gain requirement of the system. This can be seen by the red dotted line in figure 2.17. Although cell detection can be achieved with a laser/detector setup, a C-C sensor, with the analyte an integral

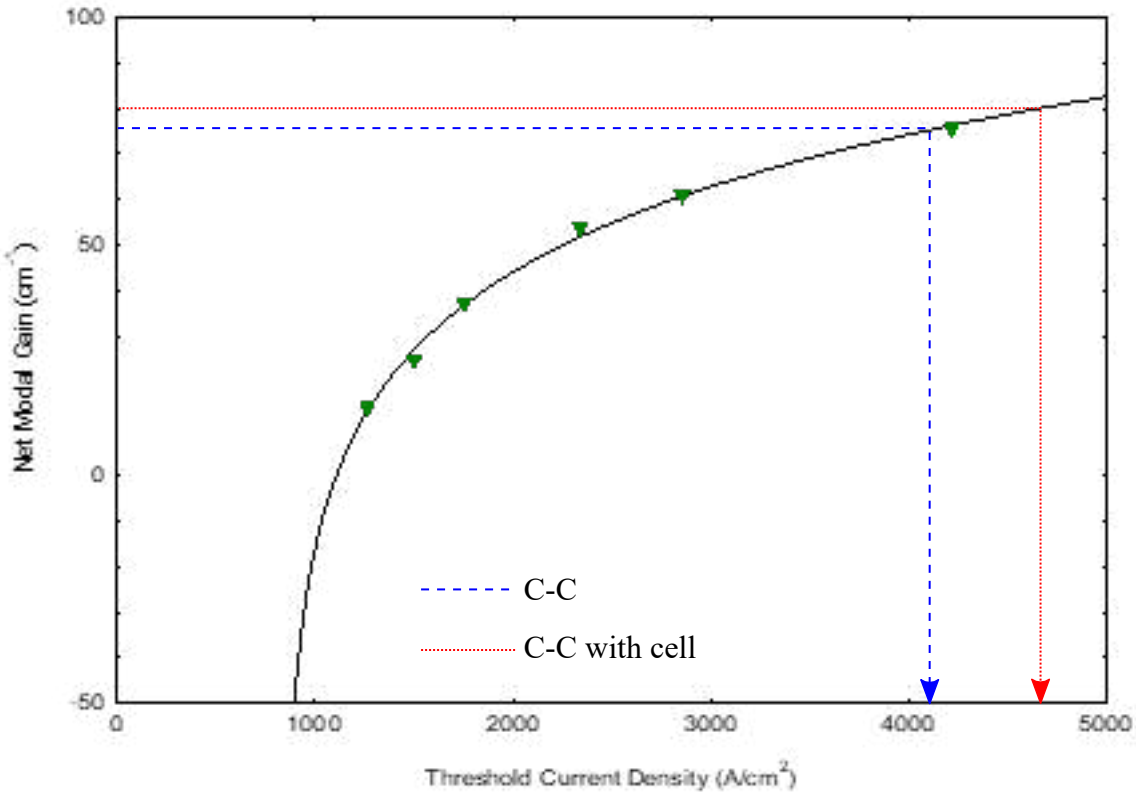

Figure 2.17: An example net modal gain versus threshold current density curve showing the increased gain requirement for the C-C laser with a passing cell in comparison to normal operation. A small change in the net modal gain requirement has a significant effect on the threshold current density due to the sub-linear gain characteristics of the material.

part of the cavity, is expected to allow more sensitive operation.

References

[1] L.A. Coldren and S.W. Corzine, *Diode Lasers and Photonic Integrated Circuits*, Wiley, New York, 1st Edition, 1995

[2] P. Blood, *Quantum Confined Laser Devices*, Oxford University Press, Oxford, 1st Edition, 2015

[3] M.G.A Bernard and G. Duraffourg, *"Laser conditions in Semiconductors"*, Physica Status Solidi, vol. 1, pp.669-703, 1961

[4] T.Numai, *Fundamentals of Semiconductor Lasers*, Springer, 1st Edition, 2004

[5] G.P. Agrawal and N.K. Dutta, *Long-wavelength Semiconductor Lasers*, Van Nostrand Reinhold, New York, 1986

[6] E. Hecht, *Optics*, Addison Weseley, 4th Edition, 2002

[7] P.S. Zory Jr., P.F. Liao, *Quantum Well Lasers: 1st Edition*, Academic Press, Inc., 1993

[8] W.W. Chow and S.W. Koch, *Semiconductor - Laser Fundamentals*, Springer-Verlag, 1999

[9] A.M. Fox, *"Optical Properties of Solids"*, Oxford University Press, Oxford, 2nd Edition, 2010

[10] C. Kittel, *"Introduction to Solid State Physics"*, John Wiley & Sons, Inc., 8th Edition, 2005

[11] L.A. Coldren, B.I. Miller, K. Iga and J.A. Rentschler, *"Monolithic two-section GaInAsP/InP active-optical-resonator devices formed by reactive ion etching"*, Appl. Phys. Lett., vol. 38, pp.315-317, Mar. 1981

[12] W.T. Tsang, N.A. Olsson and R.A. Logan, *"Stable Single-Longitudinal-Mode Operation under High Speed Direct Modulation in Cleaved-Coupled-Cavity GaInAsP Semiconductor Lasers"*, Electron. Lett., vol. 19, no. 13, June 1983

[13] L.A. Coldren, K.J Ebeling, B.I. Miller and J.A. Rentschler, *"Single Longitudinal Mode Operation of Two-Section GaInAsP/InP Laser under Pulsed Excitation"*, IEEE J. Quantum Electron., vol. QE-19, pp.1057-1062, June 1983

[14] C.H. Henry and R.F. Kazarinov, *"Stabilization of Single-Frequency Operation of Coupled-Cavity Lasers"*, IEEE J. Quantum Electron., vol. QE-20, pp.733-744, July 1984

[15] L.A. Coldren and T.L Koch, *"Analysis and Design of Coupled-Cavity Lasers-Part I: Threshold Gain Analysis and Design Guidelines"*, IEEE J. Quantum Electron., vol. QE-20, pp.659-670, June 1984

[16] L.A. Coldren, K. Furuya, B.I. Miller and J.A. Rentschler, *"Etched Mirror and Groove-Coupled GaInAsP/InP Laser Devices for Integrated Optics"*, IEEE J. Quantum Electron., vol. QE-18, pp.1679-1687, Oct. 1982

[17] W.T. Tsang and N.A. Olsson, *"High speed direct single-frequency modulation with large tuning rate and frequency excursion in cleaved-coupled-cavity semiconductor lasers"*, Appl. Phys. Lett., vol. 42, pp.650, 1983

[18] N.A. Olsson, W.T. Tsang and R.A. Logan, *"Active spectral stabilization of cleaved coupled cavity lasers"*, Appl. Phys. Lett., vol. 44, pp.375-377, 1984

[19] M. Hammer, D. Schweitzer, B. Michel, E. Thamm and A. Kolb, *"Single Scattering by Red Blood Cells"*, Applied Optics, vol. 37, iss. 31, pp. 7410-7418, 1998

Chapter 3

Device Fabrication

3.1 Introduction

A primary objective of this work is to develop and demonstrate the feasibility of an approach, combining an optically active semiconductor substrate with integrated microfluidics, to offer a micro-scale system for in-situ haematological monitoring. Micro scaling reduces required volumes, changing the way current blood-based diagnostics are used. Current approaches include microfluidics integrated onto a glass or silicon substrate [1] along with optical sensors [2] for typical "Lab-on-chip" systems [3].

Production processes in the semiconductor industry, such as photolithography, provides the necessary precision in the assembly of structural components. Using a single epitaxial wafer with industry standard approaches, allows the integration of optical sources and detectors, without time consuming and expensive manual alignment, that transferring components to a separate platform would introduce. This offers a route to manufacture low cost systems, removing the need for a single, major investment that is a current requisite for modern flow cytometers. "Pick and place" fabrication techniques [4] are less favourable in more complex systems with multiple components involving precise alignment, and therefore the monolithic integration of optical sensors, detectors and microfluidics proposed in this work, pushes the boundaries of current chip-level fabrication.

The chapter begins with an overview of photonic integration, device concept and its required capabilities. This is followed by sections detailing the design and operation of both microfluidic

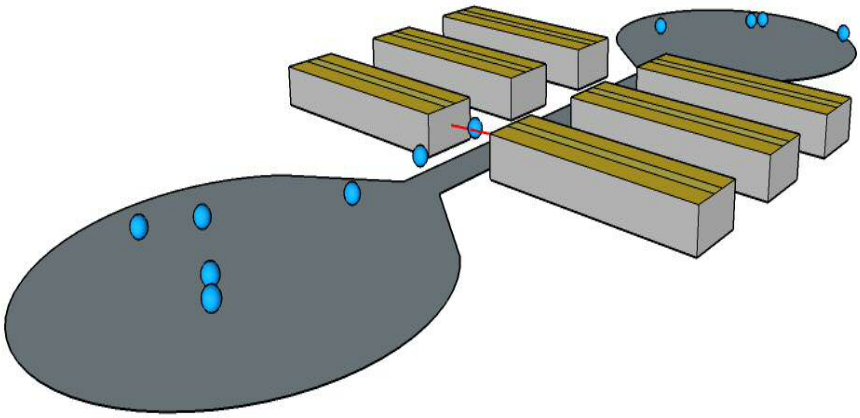

Figure 3.1: A possible device configuration showing its required capabilities. These include; a fluid delivery system with an inlet and outlet reservoir, arrayed laser sections, optical feedback provided by etched laser facets and electrical isolation provided by deep etched mesas and the fluid channel.

and optoelectronic systems. The next section includes background on select technologies used in the device fabrication. Section 3.4 follows, with detailed descriptions of processes for the fabrication of characterisation and coupled-cavity devices, and also microfluidic channels. This last part of the chapter is arranged broadly in the sequential order of the process flows.

3.2 Concept

Photonic integration provides an opportunity to scale manufacturing, whilst maintaining precise positioning with minimal increase in fabrication timescales. Increasing monolithic integration up to wafer scale creates a platform for large numbers of optical sources and detectors to be integrated [5]. The achievable alignment and density of components, adds to overall device performance and functionality. Integrated micrometric dimension designs enable greater sensitivity and resolution, critical in applications including diagnostic biosensors [6]. It also reduces the dependence on external equipment. However, electrical sensors and data processing electronics are not currently integrated alongside photonic components. The development of direct growth of compound semiconductors on silicon [7], would allow further advancement in integrated systems whilst reducing costs.

The purpose of this photonic integrated device is to provide a bench-top experimental platform

to study the influence of fluid and particles on the optical coupling between paired sections of an in-plane laser, and to provide a proof of principle coupled-cavity structure. We will use a fluid delivery system with inlet and outlet reservoirs and an interrogation region between each section of the laser. Capillary driven filling is recognised as a superior approach since it simplifies the overall integrated system and allows for bench-top and under-microscope monitoring (at research level). Precise alignment is needed for the integration of both optical and microfluidic components, which will be achieved by lithography techniques. This allows for the formation of laser facets, providing optical feedback for laser action. Etched, angled, internal facets will later be investigated as way of altering the optical loss in the gap, to create a greater cell interaction and making cell discrimination easier.

3.2.1 Microfluidics

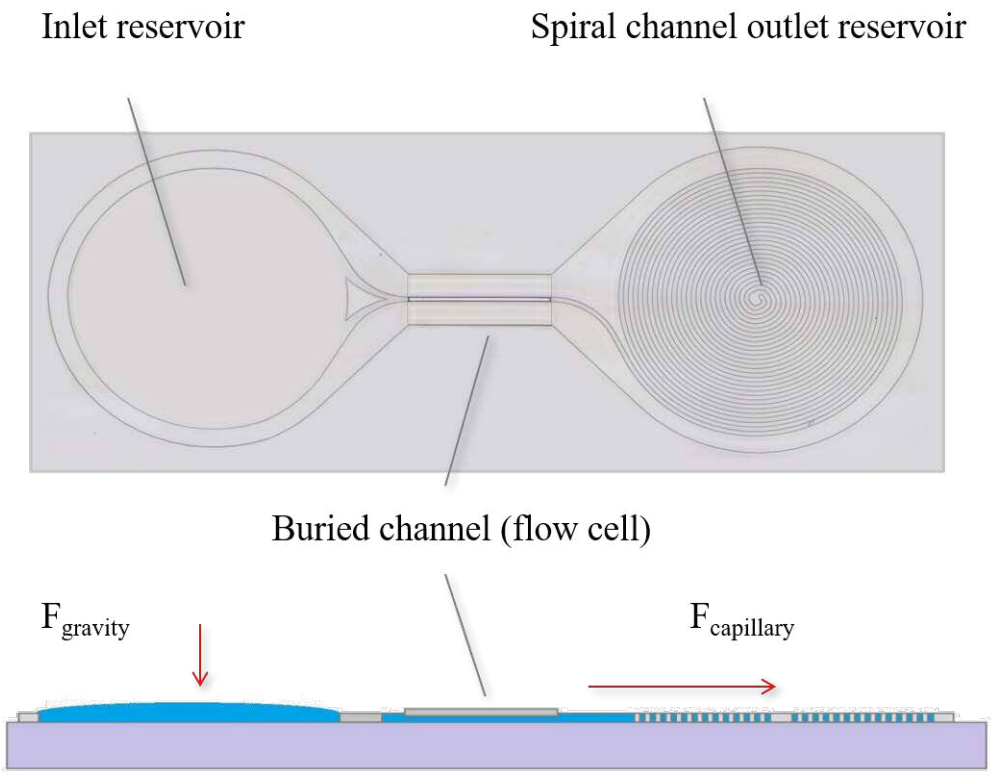

Figure 3.2: The microfluidic delivery system showing the inlet reservoir on the left and spiral channel outlet reservoir on the right. The buried channel in between the two reservoirs allows for easy interrogation of an analyte.

The microfluidic delivery system design can be seen in figure 3.2. In its simplest form the capillary fill fluid delivery system is made up of three main parts; 1) an inlet reservoir, into which sample

fluids are deposited, 2) a buried 3D channel that promotes laminar flow through the interrogation region, and 3) an outlet reservoir consisting of an open topped spiral channel that provides a sustained pull through of fluid for upwards of 30 s. However, flow rate varies depending on previous use of the device due to the wear off (over a few days) of the applied surface treatment (detailed in section 3.5). The outlet also acts as a repository for the fluid and the particles it contains, which can be utilised for subsequent analysis. The buried channel is of a length, 1410 μm, and width 50 μm, that can accommodate three laser/detector pairs to allow for multiple measurements on the same cell. This is the minimum number of repeat measurements that allow for error checking results and also allows easy calculation of cell speed. A channel longer than this would be a waste of real-estate of the III-V active substrate, increasing the final cost per device. The height of the air gap within the microfluidic channel can be adapted depending on analyte size, but in this work a standard height of 25 μm was used to allow a range of test samples to be used. The work in chapter 6 focuses on 6 and 10 μm diameter beads as these are a similar size to the smallest lymphocyte type WBCs. The inlet reservoir has been designed with the same diameter as the outlet simply for aesthetic purposes. However the small triangle at the entrance to the buried channel has been included to prevent large clumps of analyte blocking the entrance and creating a problem with future measurements and even channel cleaning.

3.2.2 Light-Source/Detector

The final device is set out as in figure 3.3 where the lasers are arranged perpendicular to the microfluidic channel. This allows for forward scatter measurements to be made on an analyte of choice. The two main methods of operation are also shown. The red highlighted sections in 3.3(a) shows a laser/detector setup, whereby section 4 acts as a laser light source and the signal is detected on section 5, across the channel, acting as a photodetector. By operating the lasers in sequence, they are effectively toggled back and forth on alternate pulses and the laser beam transit events are captured from both sides of the channel in separate but interleaved time traces.

Pumping sections 4 and 5 together, highlighted in blue in figure 3.3(b), offers the potential for C-C lasing, provided the conditions in section 2.6 are met. The channel itself becomes part of the lasing cavity and any cells introduced during measurements will affect the overall performance of the device. A change in light output can be measured in this setup, on section 6, which is the

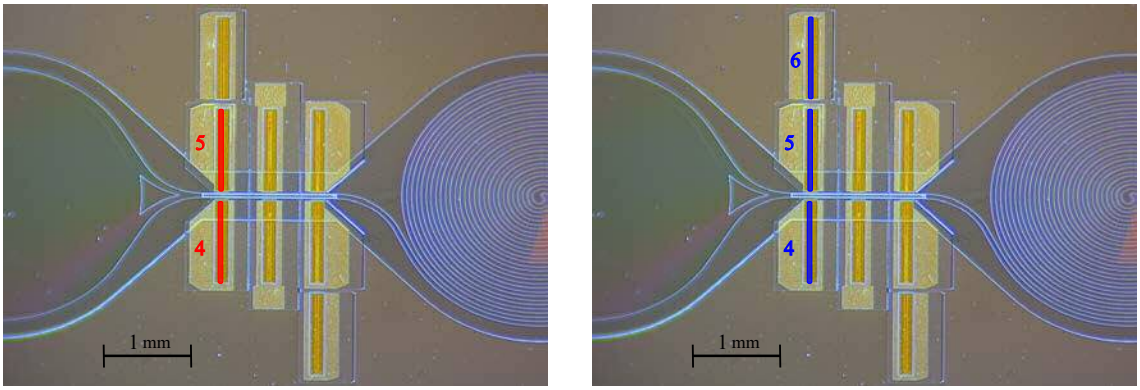

(a) (b)

Figure 3.3: Possible device configurations where (a) sections labelled 4 and 5 run as a independent laser and detector respectively or vice versa and (b) sections 4 and 5 are electronically pumped together to offer a C-C mechanism, using section 6 as an on-chip detector.

dedicated on-chip detector.

3.3 Fabrication Technologies

This section contains background on the fabrication technologies used in this work including; lithography, physical vapour deposition and metallisation, plasma-assisted etching of epitaxial layers and wet etching of GaAs.

3.3.1 Lithography

3.3.1.1 Contact Photolithography

Photolithography is a pattern transfer technique that exposes resist in a pattern that matches that on a photomask. Photomasks are usually glass with the required pattern defined by a thin film of chromium. There are a variety of different types of photolithography but contact lithography is the most commonly used in semiconductor fabrication. Figure 3.4 indicates the process behind it; resist is spun onto the substrate (wafer or smaller sample size) and the photomask is placed in close proximity to allow for alignment. Once this is achieved, the substrate is brought into 'contact' by pressing it onto the photomask for exposure. However, there are disadvantages to this technique even with its relative ease and low cost. The high defect generation, both on the sample and the photomask, mean that photomasks need to be replaced after approximately one hundred uses [8]. With contact lithography, the achievable resolution is 0.2 μm, which is limited by the diffraction of light from the UV lamp. However, in this work the smallest feature is only 4 μm. There are

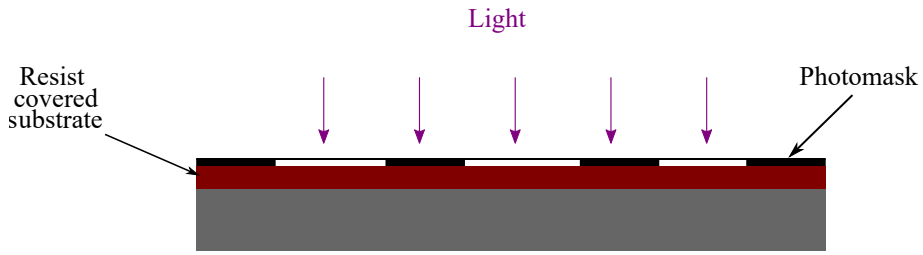

Figure 3.4: Schematic of contact lithography whereby a photomask is pressed against the resist covered substrate during exposure.

also further limitations such as scattering effects in the resist due to its finite thickness. In practise however, there are additional limitations such as non-uniformity of the photomask and sample [9] and mechanical vibrations. Resist storage and quality (from contaminants) are also crucial.

The other consideration when using contact photolithography is the type of resist used. Photoresists are energy sensitive and are either positive or negative tone. In positive resists, such as S1813, the development step removes the exposed areas and in negative resists, such as SU-8, development removes the unexposed areas. Positive resists offer higher resolution and suitable edge profiles for liftoff processes [8]. Both positive and negative resist have been used in the fabrication of the integrated device in section 3.6.

3.3.1.2 Electron-beam Lithography

Electron-beam (e-beam) lithography is a pattern transfer technique that exposes patterns directly on the sample surface. Unlike the photolithography process detailed in section 3.3.1.1, e-beam lithography uses energetic electrons (with typical energies of 10-100 kV) to expose the resist. Using this technique, features of submicron dimensions can be patterned due to the ability to focus the electron beam to spot sizes much smaller than the resolution obtained from photolithography [8]. Other advantages include the lack of defects from the photomask to degrade the exposed pattern and the ease with which patterns can be altered. However, there are two main disadvantages to this technique; (i) slow throughput makes it much slower than contact photolithography [10] and (ii) e-beam lithography tools are very expensive.

Exposure of the resist is controlled by adjusting the spot size, the beam current and the beam speed (the speed at which the beam moves over the sample). High energy electrons enter the resist and undergo scattering with atoms in the resist, thereby losing energy. This energy is transferred to the bonds in the resist, and depending on resist tone, results in either bond breaking or cross linking. Using poly(methyl methacrylate), a positive tone resist that is used in this work, results in bond breaking allowing for greater solubility of the polymer in the development process.

3.3.2 Physical Vapour Deposition

Physical vapour deposition (PVD) covers a wide range of physical deposition techniques that include two types of thermal evaporation; resistive and e-beam methods of evaporation, which are the simplest techniques for depositing thin films ($< \approx 2\ \mu$m) [11] . This section provides background on thermal evaporation for both metal and dielectric thin-films and the theoretical basis of ohmic contacts on GaAs in section 3.3.2.1.

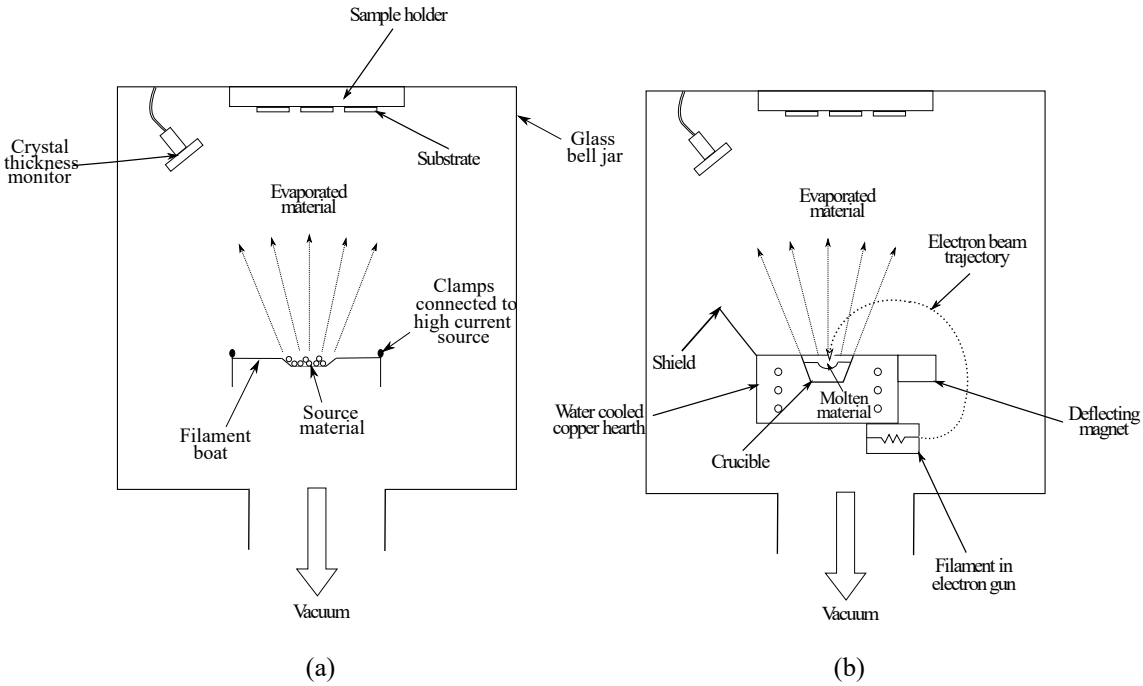

Figure 3.5: Schematic of (a) resistive and (b) electron-beam evaporation process.

In both cases, thermal evaporation involves both evaporation and condensation processes under vacuum [12]. Typical set ups are depicted in figure 3.5. On the left in figure 3.5(a), source material is evaporated by heating up material in a resistive filament or source boat by applying a current across it. Filaments and boats are usually constructed of highly resistive metals with high

melting points such as tungsten (W) or molybdenum (Mo). This differs to e-beam evaporation in (b), which uses a focussed e-beam to heat material sat in a ceramic crucible. However, both types of heating result in vaporisation of the source material which reaches the substrate in the sample holder set close to the top of the glass bell jar. It condenses back to solid state on the substrate surface, creating a thin film. The rate of particle deposition is controlled by the current applied to the filament/boat or electron gun in resistive and e-beam evaporation.

The disadvantage of resistive thermal evaporation is that W and Mo have lower melting points than certain materials, and therefore this process cannot be used for evaporating high melting point materials such as transition metals, oxides and metal oxides. E-beam evaporation also removes impurities in the thin-film as the e-beam is focussed on the material itself, only minimally heating the crucible, unlike the resistive boats. E-beam evaporation however, is a much more expensive process and therefore is only used for SiO_2 thin-films in this work, leaving evaporation of nickel (Ni), chromium (Cr), gold (Au) and gold-germanium (Au-Ge) thin-films to resistive thermal evaporation as they all have low melting points compared to Mo.

3.3.2.1 Metallisation

Ohmic contacts are required on a semiconductor to allow carriers to flow into or out of the semiconductor material. The two most important criteria (after alloying) are; linear I-V characteristics that are stable with temperature and their adhesion to the semiconductor surface. The resistance at the metal-semiconductor interface depends on the barrier height, which in turn depends on intrinsic properties of the semiconductor.

Figure 3.6 depicts the band structure of a metal-semiconductor junction that's formed when a metal is brought into contact with an n-type material. When this happens, the valence and conduction bands 'bend' to ensure thermal equilibrium can occur due to the flow of charge from the metal to semiconductor. At equilibrium, the Fermi-level is continuous across the junction. With no bias applied, the resulting potential barrier at the junction is dependant upon the work function of the metal, Φ_m, and the electron affinity of the semiconductor, χ. Therefore, the barrier to electron flow from the metal is [8]

$$\Phi_b = \Phi_m - \chi \tag{3.1}$$

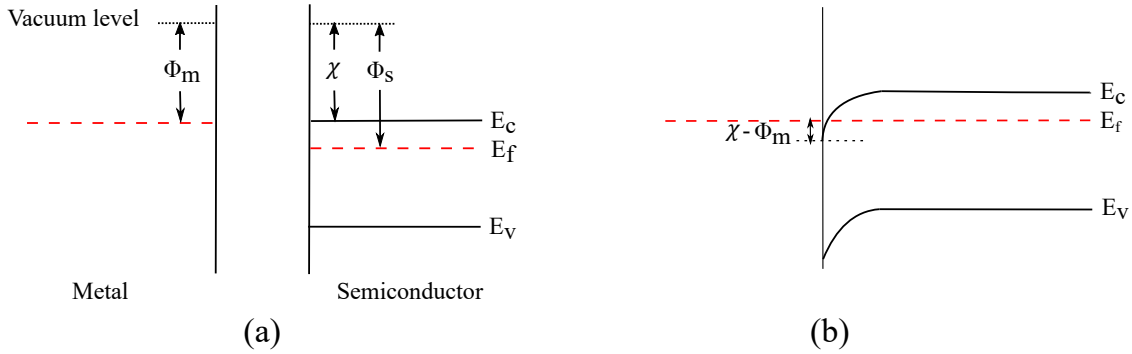

Figure 3.6: Band diagram of an idealised metal-semiconductor junction: (a) band structure of metal and n-type semiconductor before contact is made; (b) energy band diagram of alloyed semiconductor. The formation of an ohmic contact by removing the difference between the work function of the metal, Φ_m, and the electron affinity, χ of the semiconductor. This is equal to the barrier height, Φ_b.

However, in most cases the predicted barrier height is modified by surface states, and in many cases, to form an ohmic contact, the metal must be alloyed into the semiconductor surface otherwise this is an inherently rectifying junction. The result, seen in figure 3.6(b), is that χ is increased relative to Φ_m and removes the potential barrier allowing electron flow with minimal resistance.

For n-type GaAs, a AuGe/Ni/Au layered structure has been used. During alloying (around 385^{o}C), the Ga diffuses into the metal and Ge diffuses into the GaAs, acting as a dopant. Ni is used as an impurity to enhance the inter-diffusion of Ge and to act as a balling agent, to prevent balling up of the Ge metal layer [8]. For p-type GaAs, Cr/Au has been used throughout.

3.3.3 Plasma-Assisted Etching

Plasma-assisted etching, or dry etching, are techniques that use plasma to induce chemical reactions and/or ion beams to remove material. There are many characteristics of dry etching that make it advantageous over wet etching. This section provides a brief overview of the process behind the two types of plasma-assisted etching used in this work.

3.3.3.1 Reactive Ion Etching

Reactive ion etching (RIE) is a process whereby the material is chemically etched in the vicinity of the plasma by the reactive ion species which it contains. The etching of the substrate is enhanced by the kinetic energy of the ions in the plasma; this is referred to as a kinetically assisted chemical reaction. This type of etching is both chemical and physical in nature.

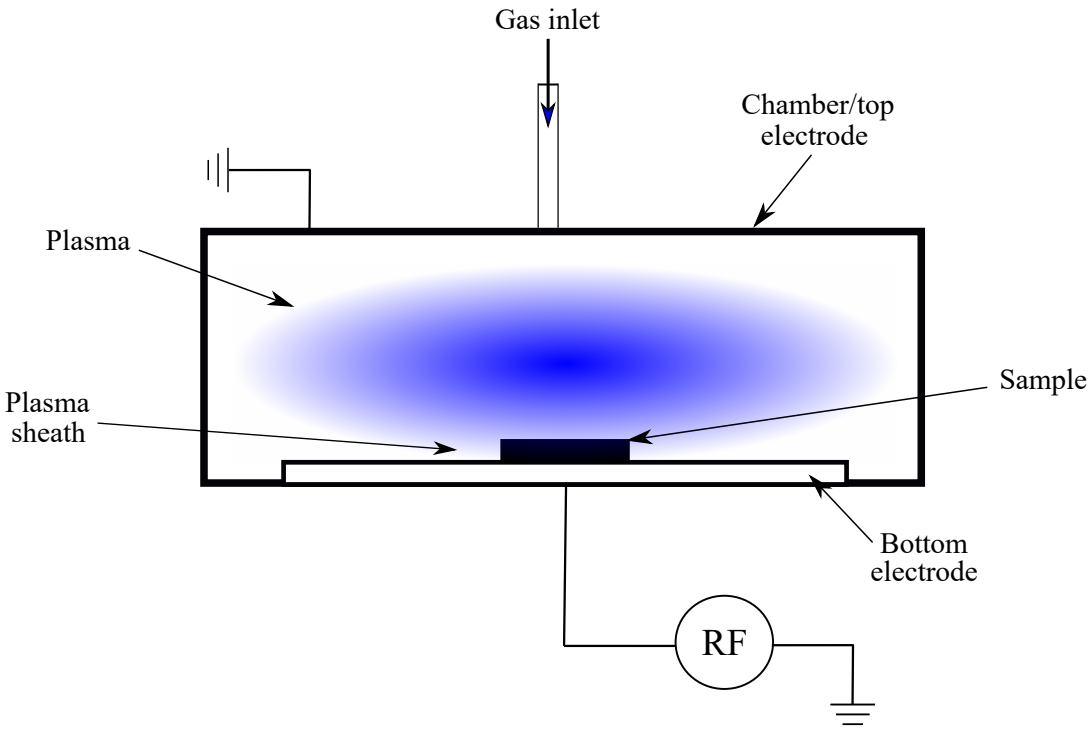

Figure 3.7: Schematic of an RIE chamber configuration showing plasma between the two parallel plate electrodes when RF power is applied to the bottom electrode.

Figure 3.7 shows a simplistic configuration of an RIE system, whereby two electrodes, one often being the entire chamber, are driven at radio frequency (RF) and ionise a small fraction of the gases released in the chamber to form a plasma. The electrode, or table, the sample sits on is RF driven and the other electrode is grounded. There is a region just above the bottom electrode where the plasma does not extend to, referred to as the plasma sheath [8]. An electric field across the plasma sheath causes ions in the plasma to be accelerated across the plasma sheath and onto the surface of the sample. A negative DC self-bias forms on the lower electrode and its magnitude determines both the density and kinetic energy of the ions bombarding the sample. Kinetically assisted chemical reactions combine the effects of purely physical sputtering and chemical etching to produce vertical profiles. The directional ion bombardment on the surface enhances the chemical etch rate by 'freeing up' the atoms of the semiconductor and also allows for the removal of the etch product, which would otherwise redeposit on the surface. Due to the perpendicular acceleration of the ions to the sample surface, the horizontal etch rate is not kinetically assisted and therefore makes it a highly anisotropic etch mechanism.

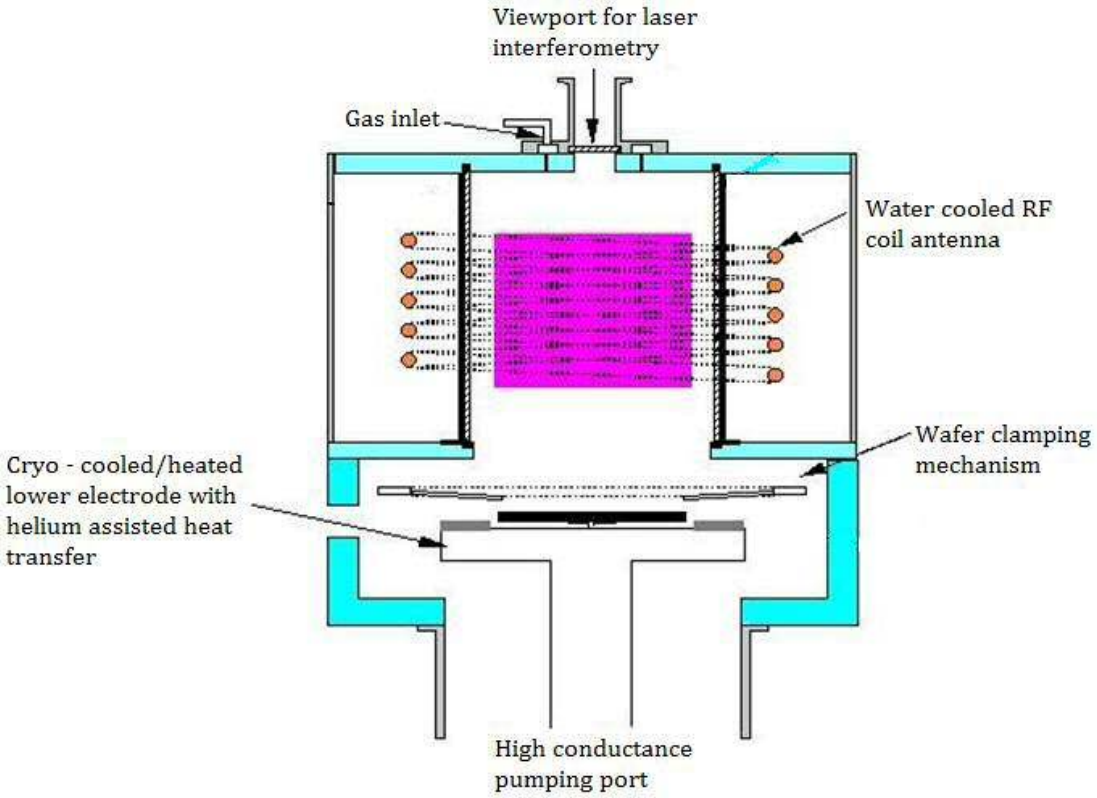

Figure 3.8: Schematic of Oxford Instruments ICP chamber layout [13].

3.3.3.2 Inductively-Coupled Plasma Etching

In an inductively-coupled plasma (ICP) system, a greater control of the etch is achieved due to the independent control of the density and kinetic energy of the ions. This allows for high etch rates to be achieved but with control over the selectivity and the damage to the sample. A schematic of an ICP chamber is shown in figure 3.8.

Unlike in a RIE system described in 3.3.3.1, an RF power is applied to an induction coil placed around a ceramic tube. A high density plasma is produced by the ICP power which is coupled inductively to a low pressure gas mixture. The energy of the ions is controlled by the RIE part of the chamber, by a forward RF power applied to the stage or lower electrode the sample sits on. This energy can be monitored by measuring the DC bias generated on the stage.

An Oxford Instruments ICP PlasmaPro 100 with a ICP180 chamber design (as in figure 3.8) has a camera and laser interferometer for monitoring samples and measuring the etch depth. Light from a laser diode, of wavelength 670 nm, is focussed onto the sample and the intensity of the reflected

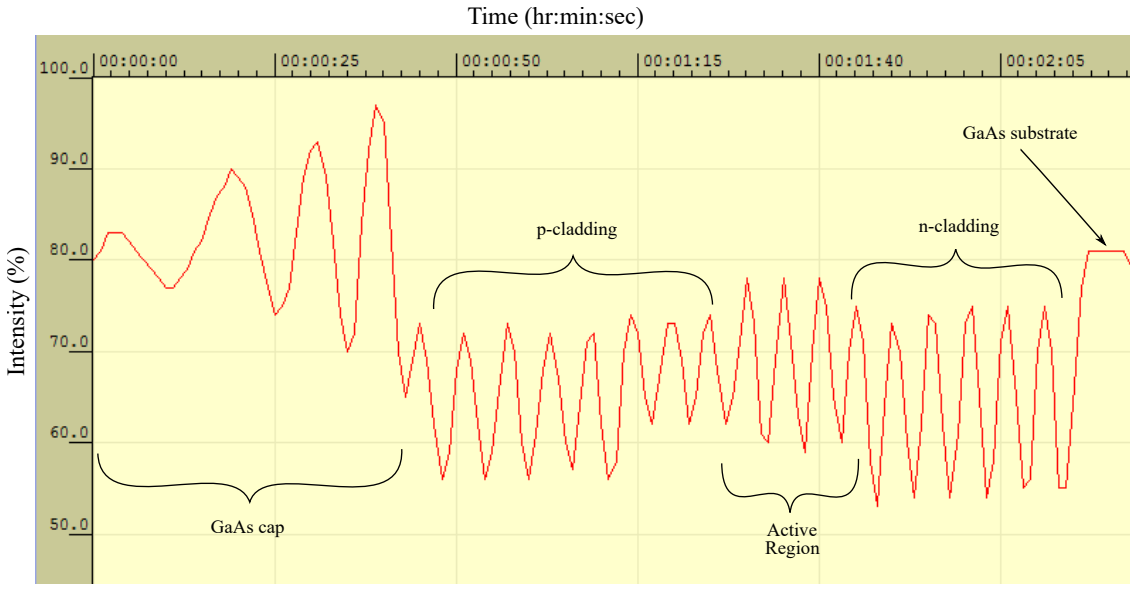

Figure 3.9: Laser interferogram obtained when etching a III-V epitaxial structure on a GaAs substrate.

laser light is measured. During the etch, the intensity of this reflected light changes due to the change in refractive index at each epitaxial layer interface. The etch rate can be monitored using the sinusoidal variation in the interference (between constructive and destructive interference) from the interference pattern it produces, allowing the etch to be stopped at a certain point or layer in the epitaxial structure. An example interferogram from etching QW material is shown in figure 3.9, where the layers in the structure can be identified. The etch depth, d, can be calculated for one period, T, by [14]

$$d = \frac{\lambda}{2n_\lambda} \tag{3.2}$$

where n_λ is the refractive index of that layer, at a lasing wavelength λ. Therefore the etch rate, ζ, can be expressed as

$$\zeta = \frac{d}{T} \tag{3.3}$$

3.3.4 Wet Etching

The GaAs semiconductor surface must be etched to create a foundation for the microfluidic channel to sit upon. It is etched to a depth of approximately 20 μm in between the coupled-cavity sections to allow for the anticipated size of particles carried by the fluid. This is achieved by an isotropic chemical wet etch which is adequate to achieve the required depth. Sidewall verticality at this stage is not crucial and removes the need for a potentially mesa-damaging plasma etch.

Without using an applied current, GaAs etchants perform in two steps; oxidation of the GaAs surface and then removal of this oxide [15]. Therefore etchants comprise an oxidising and dissolving agent, either acidic or alkaline. Hydrogen peroxide (H_2O_2) is the most popular oxidising agent for use in GaAs etching and is used along side dissolving agents such as sulphuric acid (H_2SO_4), hydrochloric acid (HCl), and ammonium hydroxide (NH_4OH) [16]. HCl's tendency to mostly form curved etch profiles and the very rapid and hence potentially unpredictable etch rate of H_2SO_4 [8] make them unsuitable for this application. Selectivity of an NH_4OH/H_2O_2 solution makes it advantageous for deep etching GaAs and therefore, the etch rate of this alkaline system has been considered.

A photoresist mask is applied to samples having n-type or semi-insulating (S-I) GaAs substrates followed by a post development bake. This ensures perfect adhesion which can otherwise affect the

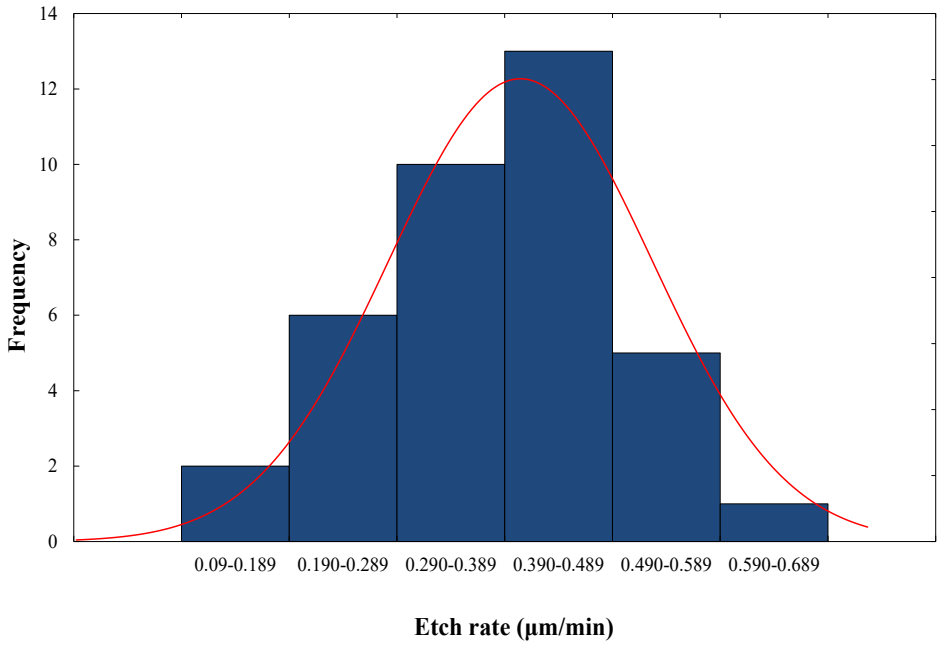

Figure 3.10: Etch rate distribution (blue bars) of GaAs samples etched in a NH_4OH/H_2O_2 GaAs etchant overlayed with a normal probability distribution (red line) of the same data.

resultant etch profile. The initial concentration of H_2O_2 used is 35%, diluted to a NH_4OH:H_2O_2:H_2O ratio of 19:1:1. To ensure a controlled reproducible etch rate each time, the solution is left for an hour at room temperature after initial mixing. This is due to the exponential decrease in etch rate because of the loss of peroxide over time. Each sample is then etched to a maximum depth of

around 25 μm, at room temperature, above which de-lamination of the photomask is observed. The samples in this study have been etched to depths ranging from 12 to 22 μm, with the depth measured every 10 minutes using a Veeco Dektak 3 surface profiler. Using a sample size of 38 fabricated samples, the etch rates of each sample has been plotted in figure 3.10. The normal probability distribution of the data gives a mean etch rate, μ, of (0.39 $\pm$ 0.11) μm/min, with the standard deviation, σ, quoted as the error. It was also found that there was no measurable difference between the etch rates for n-type and S-I substrates.

3.4 Device Fabrication

The following fabrication sections detail the main post growth processes that were carried out in a class 1000 cleanroom, and class 100 nanobooth for optical lithography, at Cardiff University.

3.4.1 Characterisation Devices

Several types of lasers and non-lasing (segmented-contact) devices have been explored during this work, which have been based on either oxide-isolated stripe or ridge waveguide type geometries. This section provides details on the process steps and developments used to fabricate devices based on oxide-isolated stripe structures only, since the latter type were not used in the final integrated device.

All samples described in sections 3.4 and 3.6 are subjected to the following sample preparation steps. A sample, typically between 10x10 or 12x12 mm^2, is cleaved from the required semiconductor wafer and the (001) crystallographic plane is found. This ensures the alignment of the oxide stripes are parallel to [111] (due to the substrate being orientated 10° to this plane), allowing the cleaved facets of the device to be perpendicular to the oxide stripe. Any debris and contaminants on the surface of the sample are removed with a multi-step solvent clean involving; methanol, acetone and isopropanol. The sample is left in each solvent for 5 minutes at 80^{o}C before being transferred to the next. This is followed by a surface de-ox using a dilute NH_4OH solution.

3.4.1.1 Multi-Section Devices

Segmented-contact edge-emitting devices have been used to analyse the single-pass amplified spontaneous emission (ASE) of different material structures to extract their modal gain and ab-

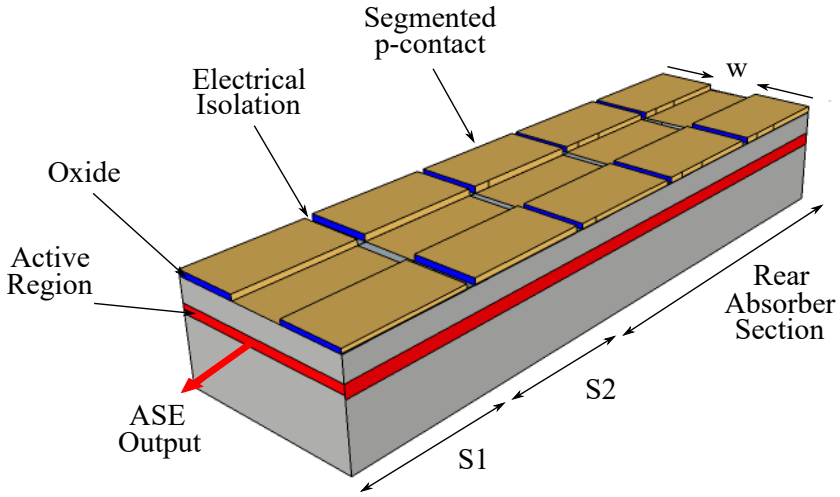

Figure 3.11: Schematic of a multi-section device used to measure ASE, where the width of injection area, $w = 50\mu m$, is defined by the removal of an insulating oxide to allow an ohmic contact to form on the p-doped GaAs surface. This p-contact is patterned into 300 μm long sections with contact wires attached to two of these, S1 and S2, along with a variable length rear absorber section.

sorption spectra. Although there are a set of standardised fabrication processes for devices described in both this section and the next (3.4.1.2), the process flow in this work has been adapted to allow for a different p-contact system to be used. This then allows a more direct comparison of the results from the characterisation devices to those obtained from the final integrated device in section 3.6.

Step 1: Forming the oxide stripe

Defining an area for current injection involves depositing 120 nm of a dielectric material, in this case SiO_2, as in figure 3.12(a) using an electron-beam evaporator.

To create a photoresist etch mask, the first step is to spin coat the substrate with photoresist. In this instance the photoresist used is Microposit S1813 which is used in conjunction with an adhesion promoter, Hexamethyldisilane (HMDS). HMDS is used to improve the adhesion to the GaAs and SiO_2 surfaces [17] due their low adhesiveness. The photoresists are deposited onto the sample in liquid form and then distributed in a thin layer across the surface using a photoresist spinner (figure 3.12(b)). HMDS is applied with a spin speed of 6000 rpm for 45 seconds and immediately followed by S1813 with the same recipe. The photoresist is then baked at 97^{o}C for 3 minutes to re-

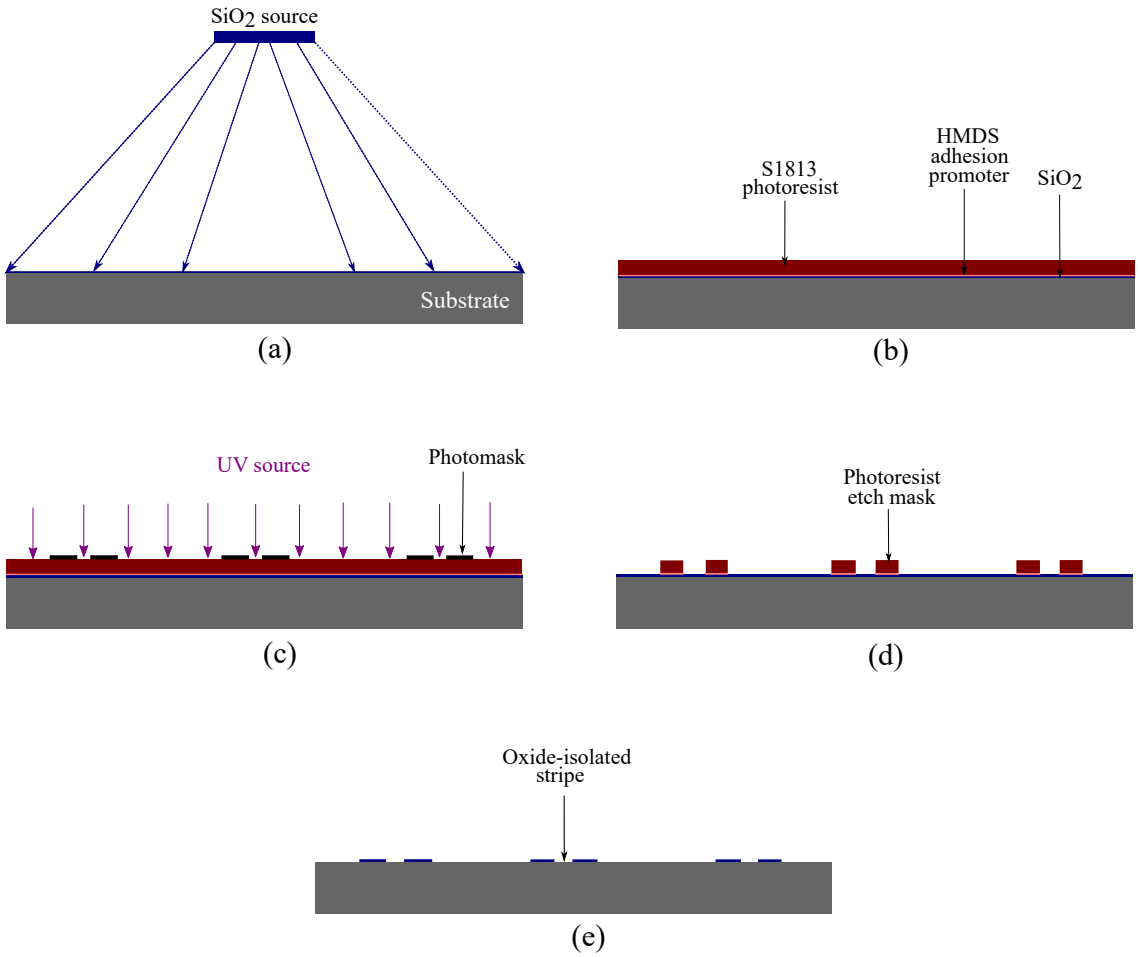

Figure 3.12: Schematics of the main process steps involved in defining an oxide stripe for a multi-section device or oxide-isolated stripe laser. (a) Thin film deposition of SiO_2 using an electron-beam evaporator. (b) Application of adhesion promoter and S1813 photoresist. (c) Exposure of the photoresist using an ultraviolet (UV) mercury lamp and a photomask patterned with opaque metal. (d) The photoresist profile after exposure and development. The sample is baked at this point to form a mask that will withstand chemical wet etching. (e) The resultant profile of the patterned SiO_2 following the removal of the unwanted dielectric material and photoresist.

move any solvent in the resist. With the photoresist applied and baked, the combination of sample and optical photomask is exposed with an ultra-violet (UV) mercury lamp. The opaque metal on the mask blocks the light reaching the photoresist underneath (figure 3.12(c)). The alignment of the photomask to the sample and exposure was done with a Karl Suss MJB3 UV400 mask aligner, with the sample exposed for 6 seconds and then developed in Microposit MF-319 developer for 30 seconds. To withstand the following wet etch, the patterned photoresist is baked again at 97^{o}C for 3 minutes (figure 3.12(d)). The typical thicknesses of the baked S1813 is around 1.5 μm.
To remove the unwanted SiO_2, the sample is immersed in a dilute hydrofluoric acid (1:4 47-50% HF:H_2O) solution for only 7-8 seconds due to the relatively thin layer of material to be removed. The acid removes the oxide but leaves the photomask and GaAs surface unharmed. The etch results in a typical undercut of 3 μm under the resist mask. Following the removal of the photoresist, the SiO_2 has the profile as seen in figure 3.12(e). The window opened up in the oxide is for the formation of an ohmic p-contact on the GaAs surface in the next step of the fabrication process. Please note, this etch solution is extremely hazardous and several safety precautions but be taken before use including training and additional personal protective equipment.

Step 2: p-Contact

Chrome-gold (Cr-Au) over the standard zinc-gold contact system has been identified as the best contact system for use in the final device and therefore a liftoff process is used. Section 3.6 will discuss in more detail the reasoning behind this.

For a successful metal lift-off, two photoresists are used to create a bilayer resist process to provide a suitable resist profile [18]. The desired profile is seen in figure 3.13. In this instance the two photoresists used were PMGI SF6 and Microposit S1813 on top of HMDS. HMDS is applied as in step 1 and immediately followed by SF6 spun at 5000 rpm for 20 seconds. The sample is then baked on a hotplate for 10 minutes at 97^{o}C. The second layer of photoresist, this time S1813, is applied using the same procedure but baked at a lower temperature of 80^{o}C for just 5 minutes. Typical thicknesses of the baked S1813 and SF6 are 1.5 μm and 600 nm respectively. The exposed S1813 photoresist is removed in the developer and leaves a profile whereby the SF6/HMDS layer undercuts the S1813 layer above. This is because the SF6 and HMDS do not need exposing to UV light to be removed. This type of resist profile is useful for metal deposition to prevent a

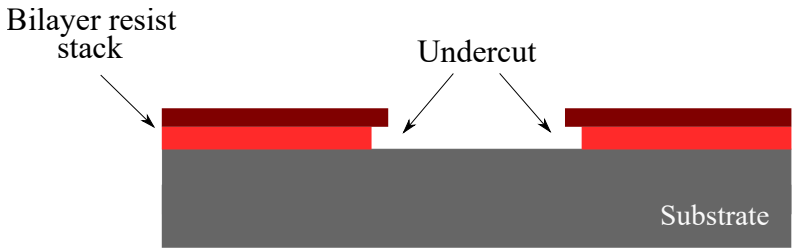

Figure 3.13: The desired profile of a bilayer resist stack after exposure and development. The undercut is necessary to for an improved yield in lift-off processes and can be controlled by resist type and both exposure and development times.

continuous metal film from forming which would then be extremely hard to remove. For ohmic p-contacts, 10 nm Cr and 300 nm Au are thermally evaporated onto the GaAs and resist surfaces.

To maximise electrical isolation and minimise current spreading between sections, there must be a 6 μm gap in the contact pattern to allow the highly conductive p-doped GaAs cap to be etched. The aforementioned GaAs etch in section 3.3.4 is used but in this instance only the thin cap layer is to be removed (typically 200-300 nm depending on wafer specifications).

Step 3: Electrical Isolation

After removing the unwanted metal films and resist on the sample, the resulting p-contacts are again coated in HMDS/S1813 (following the same procedure as in step 2). This time a 4 μm window is patterned inside the 6 μm window previously opened up in the p-contact to allow both the 50 μm wide SiO_2 stipe and GaAs cap to be etched. Once the SiO_2 has been removed (as in step 2) this etch mask is also removed and HMDS/S1813 is applied once again. This time 50 μm wide windows are opened up in the resist, in between and parallel to the previously patterned 50 μm stripes, to etch the Au from these regions. This allows for a much cleaner cleave of individual devices once all the process steps have been completed. Unlike in section 3.3.4, the GaAs is etched here with the Cr-Au acting as the etch mask. For these purposes, the metal p-contact is then annealed in a JetFirst rapid thermal annealer (RTA) to form low resistance ohmic contacts where the Cr and gallium (Ga) can inter-diffuse and prepare it for the GaAs etch step. Here, only the cap is removed (200 - 300 nm depending on epitaxial structure).

Step 4: n-Contact

The sample must first be thinned, typically to 100 μm, so that it can be cleaved into individual segmented-contact devices. This is done by lapping the reverse side of the wafer with a rotating silicon-carbide disc. As the devices will be mounted epitaxial-side up and GaAs being a poor thermal conductor, the lapping process also improves heat extraction from the device. This is followed by a polishing step, to smooth the surface and remove abrasions, using polishing products on a rotating disc.

Following lapping and polishing, a blanket coating of gold-germanium (Ge-Au), nickel (Ni) and Au is deposited on the freshly lapped side of the substrate with thicknesses of 100, 28 and 300 nm respectively. This thickness of Au is required to ensure the metal surface is suitable for wire bonding, and also improves the sheet resistance of the contact.

3.4.1.2 Oxide-Isolated Stripe Lasers

(a) With Cleaved Facets

This type of laser is the easiest and quickest to fabricate, which holds benefits for simple epitaxial wafer characterisation measurements. An oxide-isolated stripe laser is similar to that shown in figure 3.11, following the same fabrication steps set out in section 3.4.1.1. However, as seen in figure 3.14, the p-contact is continuous allowing for electrical connection anywhere along the cavity length. This means that steps 2 and 3 detailed above are changed somewhat to account for the now unnecessary isolated sections, but step 4 for patterning the n-contact remains the same. After annealing and lapping, the sample can be cleaved into individual devices of a chosen length.

(b) With Etched Facets

The monolithic nature of the device design described in section 3.2 requires each of the laser sections to have etched facets. This can be done either by a chemical wet etch, which involves submerging the sample in a solution of ethchant, or by a dry etch, which exposes the sample to a bombardment of ions using a plasma. In this work, all etched laser facets have been fabricated exclusively using an inductively coupled plasma (ICP) etch, the process of which is described in this section. An ICP dry etch is preferred over a chemical wet etch due to the need to create high-aspect-ratio structures with vertical sidewalls that are etched all the way through the epitaxial

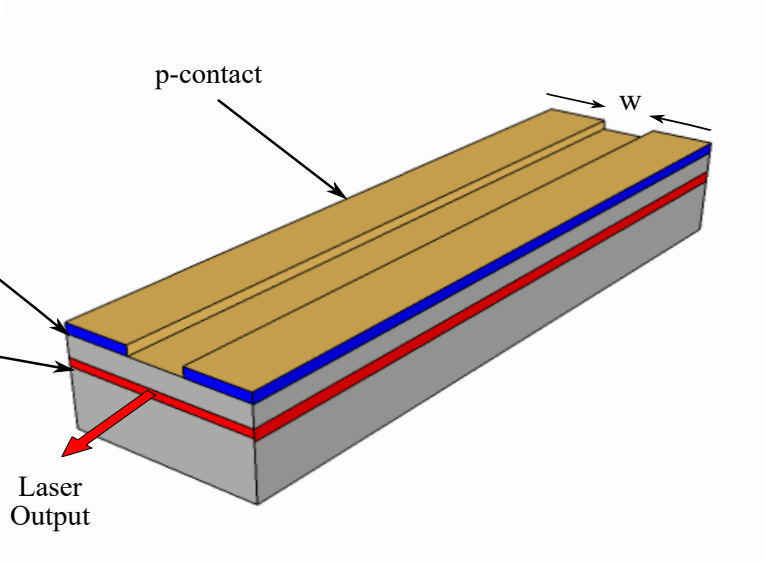

Figure 3.14: Schematic of an oxide stripe laser with two cleaved facets. The width and formation of the injection area, *w*, is as in figure 3.11. However here, the p-contact is continuous and an electrical connection can be made anywhere along the length of the cavity.

growth layers to reach the highly doped gallium arsenide (GaAs) (typically 2.7-3.4 μm). With this etch depth required, a dry etching technique is more directional and creates facets with a smaller root mean squared (rms) roughness value [19].

Step 1: Etch mask patterning

A 250 nm thick layer of PMMA positive resist is spun onto the sample (figure 3.15(b)) at 5000 rpm for 45 seconds and baked at 180^{o}C for 3 minutes. The laser facet pattern is applied to the resist by direct write exposure using a Raith eLINE electron-beam lithography (EBL) machine. Exposing the resist to the electron beam changes the solubility of the resist by breaking the long polymer chains into smaller fragments. This enables the selective removal of the exposed resist in a methyl isobutyl ketone: isopropanol (MIBK:IPA) solution (figure 3.15(c)). EBL creates a high contrast and near-vertical step resist profile, which is important for the following two process steps so as not to diminish the resulting facet efficiency.

Step 2: Etch mask preparation

60 nm of nickel is deposited thermally on top of the sample (figure 3.15(d)) and following a lift-off process, metal is left as an etch mask to create mesas with etched facets (figure 3.15(e)). Ni was selected as the etch mask material for this work to overcome terracing effects and sloped sidewall

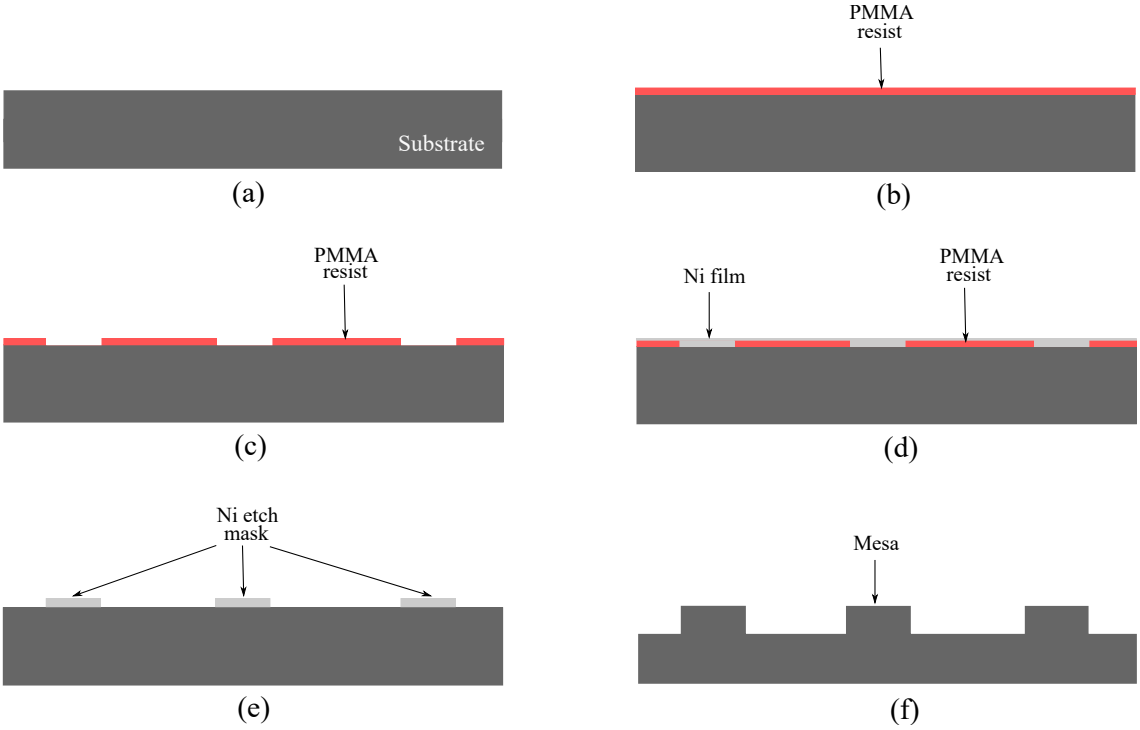

Figure 3.15: Schematics of the main processes involved in the fabrication of etched laser facets. (a) The semiconductor substrate before any fabrication has started. (b) Application of PMMA EBL resist. (c) The resist profile after exposure to the electron beam and development for use in a following lift-off process. (d) Thermal evaporation of a nickel (Ni) film onto the sample and resist surfaces. (e) The etch mask on the substrate surface following the removal of excess metal and resist. (f) The resultant profile of the etched mesa, hence etched facets following a high temperature ICP dry etch and removal of Ni by a wet etch.

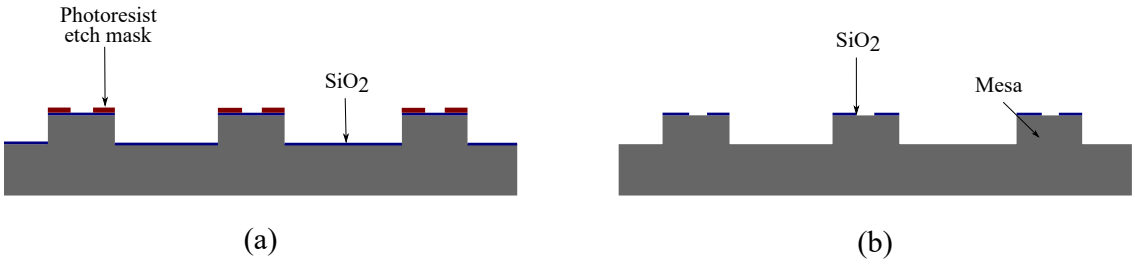

Figure 3.16: (a) The photoresist profile after exposure and development. The sample is baked to form a mask that will withstand chemical wet etching. (b) The resultant profile of the patterned SiO_2 on the GaAs surface following the removal of the unwanted dielectric material and photoresist.

profiles typically seen when using silicon dioxide (SiO_2) masks [20] [21].

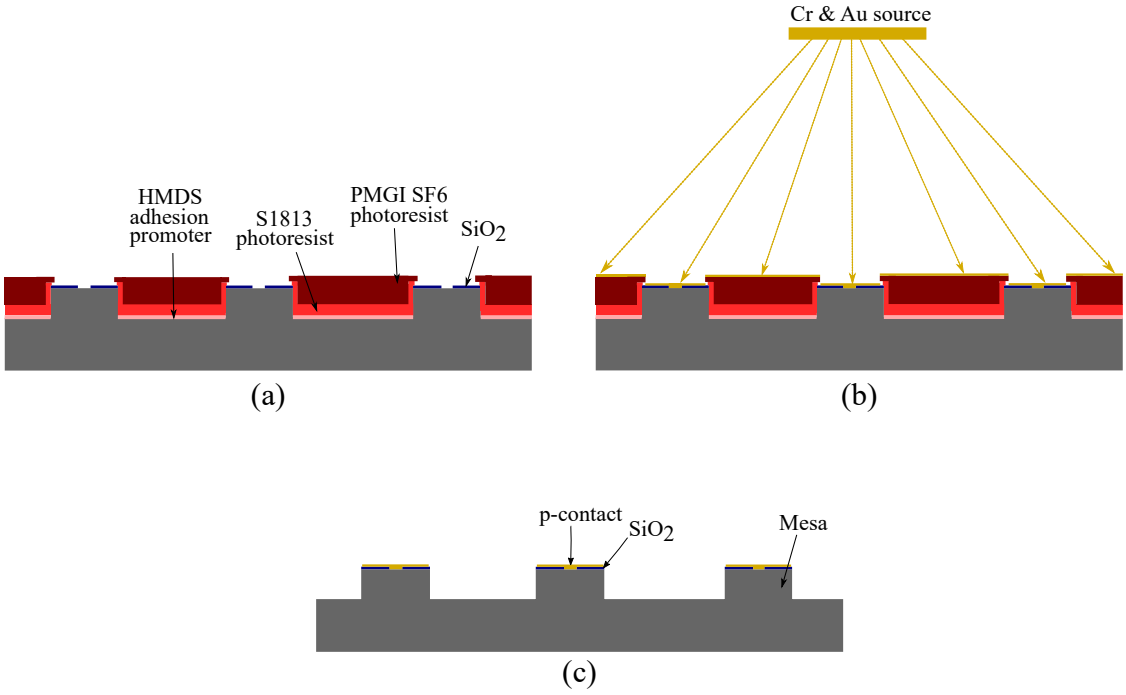

Figure 3.17: Schematics of the main processing steps involved in the fabrication of p-contacts using a bilayer process. (a) Application and exposure of an adhesion promoter and a bilayer resist. (b) Thermal evaporation of Cr and Au films onto the sample and resist surfaces. (c) The resultant profile of the AuGe/Ni/Au n-contacts and positioning relative to the mesa structures after removal of the unwanted resist and metal.

Step 3: Plasma etching

The etch mask is then used to transfer the original EBL pattern into the semiconductor crystal using a chlorine/argon (Cl_2/Ar) ICP etch [22] with a gas ratio of 1:9. This is done at high temperature to effectively etch the AlGaInP cladding layers [23] in the wafers used for this work with RIE and ICP powers of 200W and 500W respectively . Once the Ni mask is chemically etched away, the mesa structure has a profile as in figure 3.15(f).

Step 4: Formation of oxide stripe

The formation of the oxide stripe follows the procedure set out in step 1 of section 3.4.1.1. However, the etch mask is such that the oxide is removed from the whole sample surface except for an area on top of the etched mesa (figure 3.16(a)), leaving a profile like in figure 3.16(b).

Step 5: Ohmic Contacts The same steps here apply as before; Cr/Au p-contacts are patterned

(figures 3.17 (a) and (b)) and annealed to the GaAs surface on the tops of the mesas (figure 3.17 (c)) and a AuGe/Ni/Au coating is evaporated onto the lapped reverse side of the substrate.

3.4.2 Coupled-Cavity Lasers

Section 2.6 along with figure 2.14 explains the necessary device geometry to achieve C-C lasing. The waveguide discontinuity is achieved by etched facets and patterning a gap between the two sections. The whole process is the same as in section 3.4.1.2 (b), but to provide complete controllability and isolation, each section has co-planar n-contacts. These are patterned in the same way to the p-contacts with a bilayer process and is described in figure 3.18.

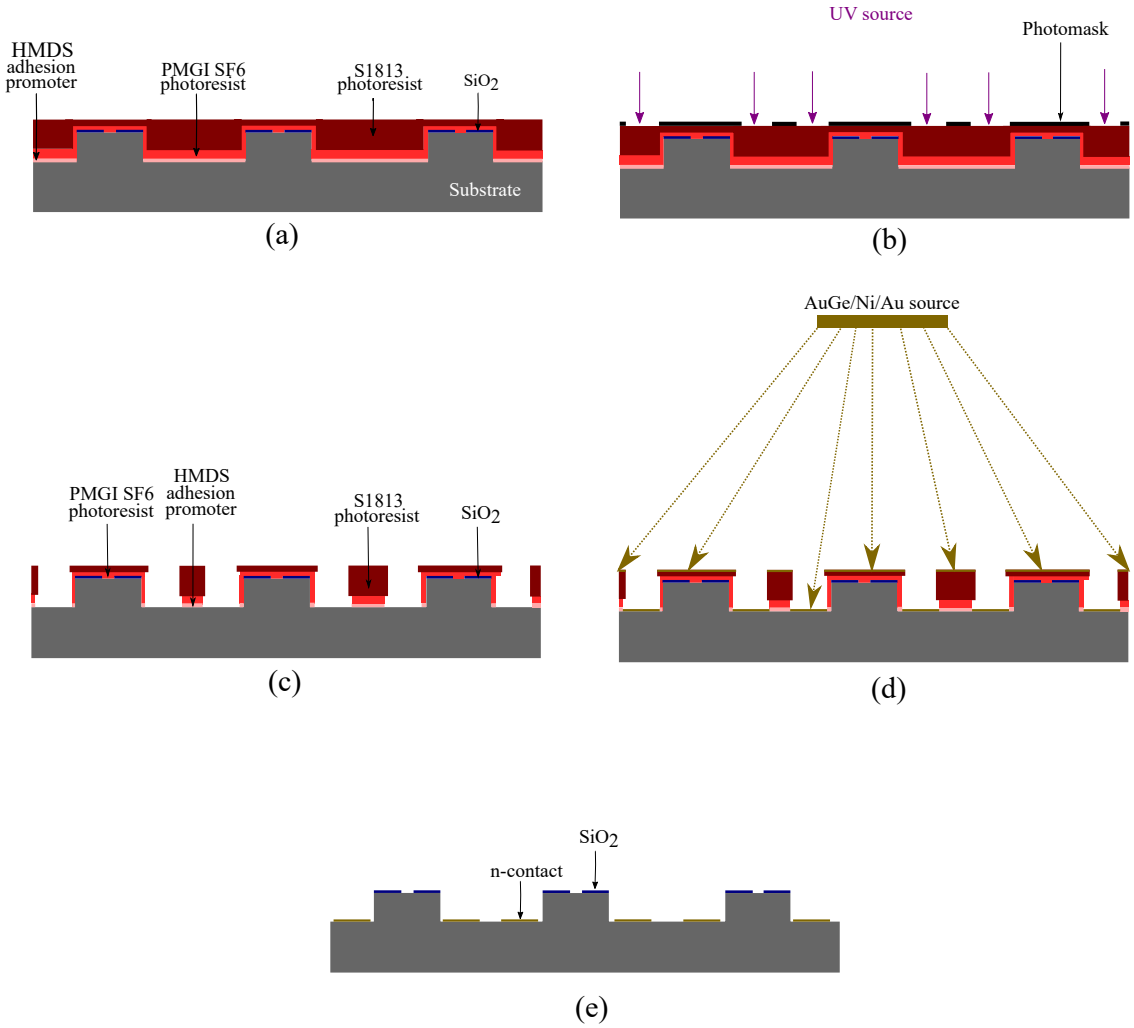

Figure 3.18: Schematics of the main processing steps involved in the fabrication of patterned co-planar n-contacts using a bilayer process. (a) Application of an adhesion promoter and a bilayer process of PMGI and S1813 photoresists. (b) Exposure of the photoresist using an ultraviolet (UV) mercury lamp and a photomask patterned with opaque metal. (c) The photoresist profile after exposure and development for use in a metal lift-off process either side of the etched mesa. (d) Thermal evaporation of AuGe, Ni and Au films onto the sample and resist surfaces. (e) The resultant profile of the AuGe/Ni/Au n-contacts and positioning relative to the mesa structures after removal of the unwanted resist and metal.

3.5 Microfluidics Fabrication

3.5.1 Deep-etched channel

To achieve an interrogation region where an analyte is detected in the same plane as the active region of the laser, a deep-etched channel must be incorporated between the laser sections. This is achieved using a photoresist mask consisting of HMDS and S1813. It is as such that all laser sections are covered individually by the photoresist leaving the rest of the GaAs surface of the sample exposed, including a 30 μm wide channel between the etched facets of the patterned mesas. This allows for not just electrical isolation across the channel but also reduces electrical pickup in neighbouring detector sections. The cross-section in figure 3.19 indicates a non-vertical side wall of the etched channel, but verticality is not crucial here as it just serves as a foundation for the following SU-8 layers.

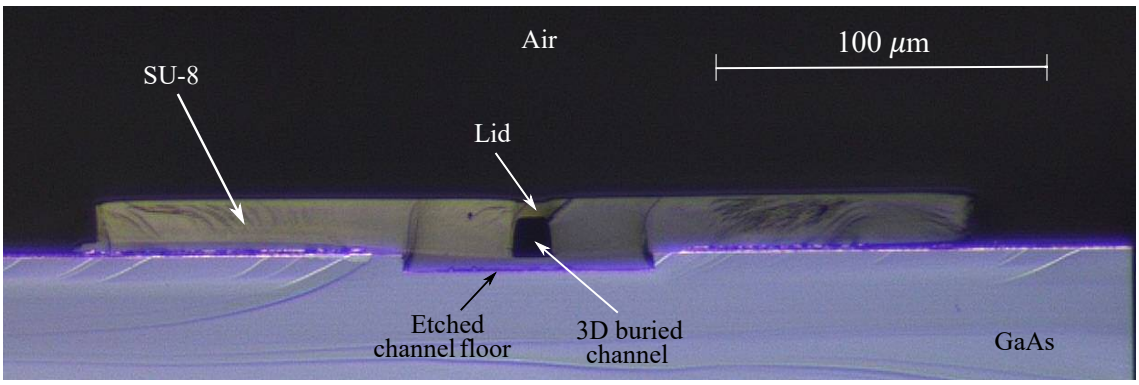

Figure 3.19: Optical microscope image of an etched GaAs channel and integrated buried microfluidic channel. The etched channel floor in the GaAs substrate creates a foundation for the SU-8 and buried channel to sit on.

The configuration of the integrated microfluidics

3.5.2 Microfluidic channel

The integrated microfluidics fabricated in this work have been achieved using layers of the polymer SU-8. SU-8 has become very popular in recent years in the MEMS field for several reasons; it is a negative tone photoresist that cross-links with standard near-UV photolithography, chemically resistant, suitable for biomedical applications and has almost 100% optical transmittance at visible wavelengths [24], [25], [26].

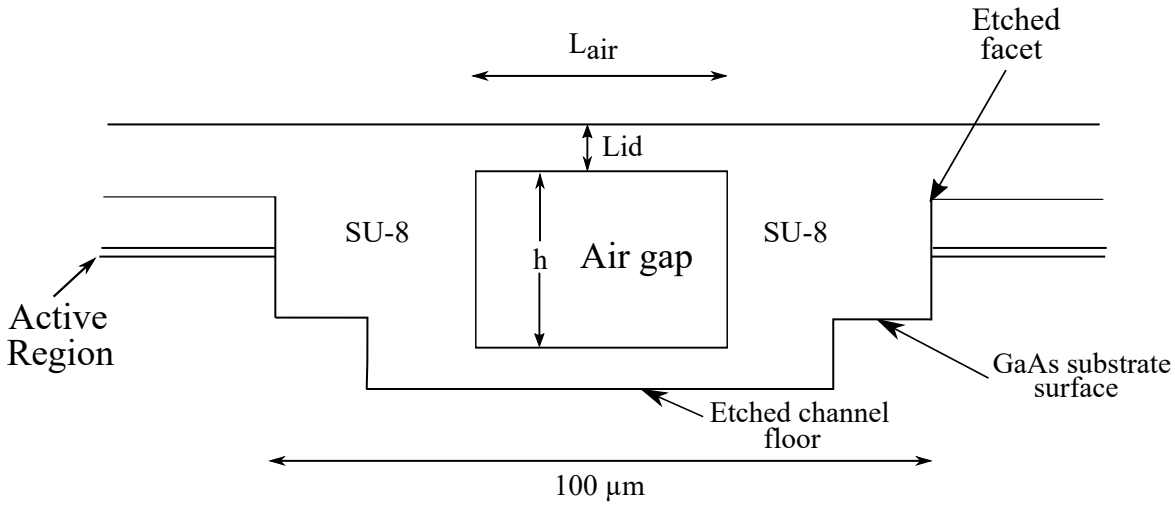

Figure 3.20: Schematic of an etched channel in the GaAs substrate and the buried microfluidic channel between a pair of etched facet lasers. The air gap should sit in the etched channel so that the active region of the laser will interact with the analyte at the central point of the microfluidic channel. The distance between the etched facets is 100 μm. The width, L_{air}, and height of the air gap and the thickness of the lid can be changed by simply altering the exposure pattern and spin speed of the SU-8 respectively.

To create a foundation layer on the previously etched GaAs surface, a 2 μm thin layer of SU-8 2002 is spun onto the sample. This also acts as an adhesion layer for the next layer of SU-8 due to the poor adhesion of this polymer to both Au and SiO_2 [27]. After exposing and hard baking this foundation layer, the next step is to spin coat the sample with a 20-25 μm thick single layer of SU-8 2050 (figure 3.21(a)). This defines the sidewalls and height of the channel. A technique, as reported in [28], using a dual wavelength exposure [29], creates 3D microfludic channels using only this single layer of polymer and a double UV exposure. A 370 nm long pass filter used in conjunction with a photomask, patterns the walls of the structure (figure 3.21(b)) and is then immediately followed by a second exposure to define the channel lid; a covered section of the microfluidics. This second exposure uses a 340 nm band pass filter to single out the 334 nm emission line of the mercury lamp. SU-8 is highly absorbing at this wavelength so the light can only expose a short way down into the polymer, as in figure 3.21(c). This is in contrast to the exposure at 370 nm, since at this wavelength light is only partially absorbing so it can reach all the way down to the bottom of the SU-8 layer. The final structure in figure 3.21(d) is completed after cross-linking of the polymer by a post exposure bake and development in Microposit EC solvent. Figure 3.19 shows a optical microscope image of the cross-section of the SU-8 buried channel and lid on a GaAs substrate.

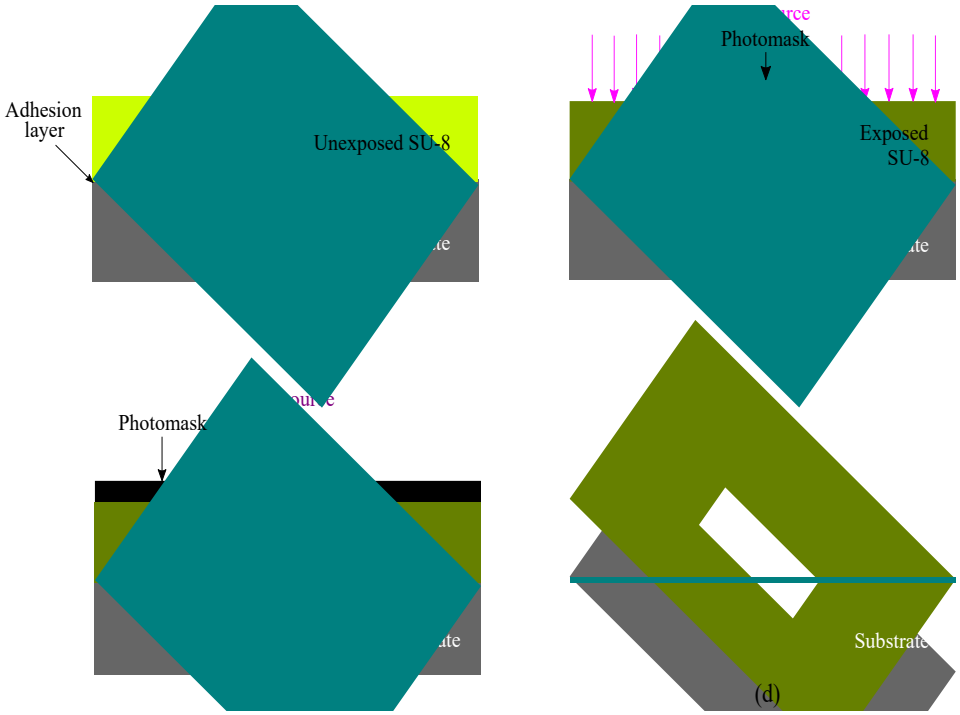

Figure 3.21: Schematics of the processing steps in the fabrication of microfluidic channels. (a) Application of both an adhesion layer and SU-8 negative tone photoresist onto the semiconductor substrate. (b) Exposure of the SU-8 using an ultra-violet (UV) mercury lamp, a long-pass filter and a glass photomask patterned with opaque metal to define the channel walls. (c) Immediately after (b), the SU-8 is exposed again with a shorter wavelength (using the same UV lamp as in (b)) and a photomask to pattern a lid over the channel. (d) The microfluidic channel profile after the post exposure bake and development.

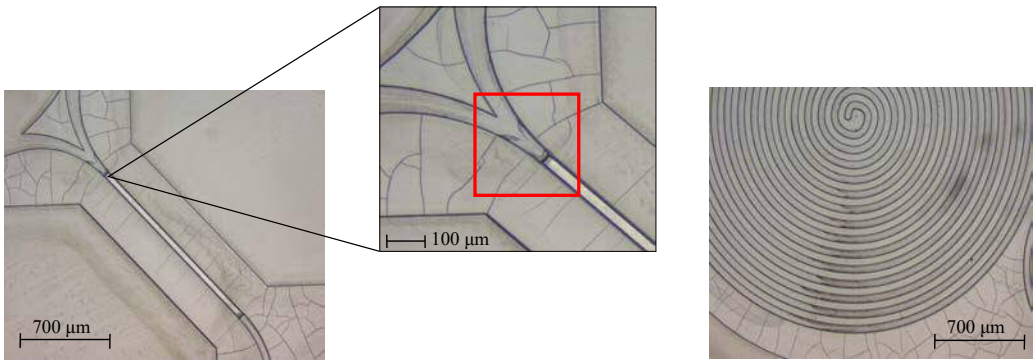

Figure 3.22: Optical microscope image of an SU-8 microfluidic channel and lid, (a), after 15 minutes development time. (b) and (c) show large amounts of SU-8 blocking the channel inlet and spiral.

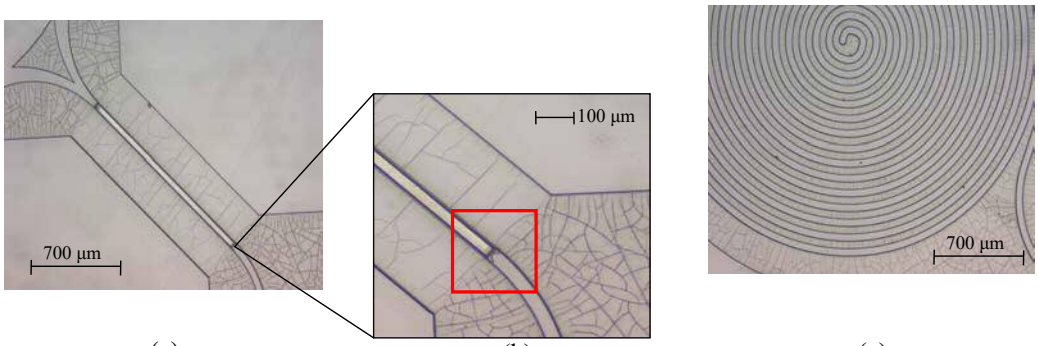

Figure 3.23: Optical microscope image of an SU-8 microfluidic channel and lid, (a), after 30 minutes development time with a clear channel inlet. (b) shows only a small amount of SU-8 left at the channel outlet and (c) a now completely clear spiral.

The complexity of the pattern and differing density of material to be developed across the sample due to the mixture of open and buried channel, results in a significant difference in minimum development time. Development times range from 15-45 minutes for different parts of the microfluidics and requires systematic checking that development is successful across the whole sample before hard baking. A range of development times of the channel were tested and figures 3.22, 3.23 and 3.24 show different times and the success at each point of SU-8 microfluidic channels patterned on glass substrates. After 15 minutes, thinner layers of SU-8 are removed from the inlet reservoir (top left corner of figures 3.22 (a) and (b)), but the channel inlet (highlighted in red) and majority of the outlet spiral are undeveloped. Improvement is seen after a further 15 minutes (30 minutes in total) in the developer and with the outlet spiral now completely clear of unexposed SU-8. However, there is still a small amount at the channel outlet highlighted in red in figure 3.23 (b). Figure 3.24 is a channel after 45 minutes in developer, which now shows no SU-8 around the channel outlet. The development of the inside of the channel is checked by being able to focus on both the channel base and then the lid separately and using a pipette to drop a small amount of IPA in the reservoir and checking it can pass through the buried channel to the spiral outlet. The aim of this microfluidic fluid delivery system is to enable lab-on-chip sensing without the need for external pumps. The surface of SU-8 on its own however, is insufficiently hydrophilic to provide capillary flow of fluids such as DI water and phosphate-buffered saline (PBS). These fluids make up the majority of the content in samples containing WBCs for flow cytometry. It has been shown that a two-stage surface treatment to SU-8 can provide long term hydrophilocity [30]. Although [30] details both a first stage hydrophilic treatment and second stage stabilisation treatment, only

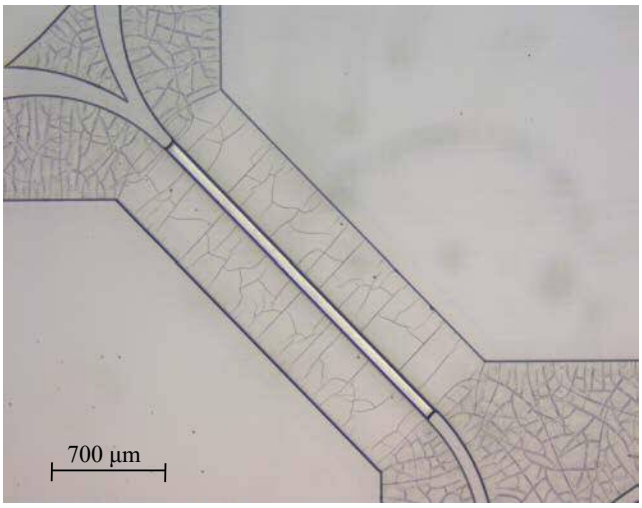

Figure 3.24: Optical microscope image of a completely developed SU-8 microfluidic channel after 45 minutes in developer.

the first stage plasma treatment has been used on the samples as there is no need for a long term solution at this stage. An RIE kit was used to apply an oxygen plasma with an etching power of 100 W to the sample for 1 minute. This treatment along with the spiral outlet design provides us with up to 60 seconds of fluid flow for interrogation.

3.6 Final Device

The final fabricated device in figure 3.25 shows the two main components; a monolithic laser/detector array and a microfluidic fluid delivery system, integrated on an optically active GaAs substrate. The array of 30 μm wide oxide isolated stripe laser pairs patterned on 150 μm wide etched mesas are set 100 μm apart either side of the 3D microfluidic channel. The lasers themselves are fabricated as in section 3.4.2 with Cr/Au p-contacts. This metallisation system was chosen over zinc-gold and titanium-gold for its superior adhesion to both SiO_2 and GaAs. The channel used in this work is 50 μm wide and 1410 μm long, patterned onto a 20 μm deep channel in the GaAs substrate. On two of the C-C laser pairs, there are specific on-chip detectors (first and third pair in the array in figure 3.25). This allows these two pairs to be configured as either a laser-detector pair using simply the sections directly either side of the channel or a C-C/detector system using the two sections around the channel as a C-C and then the third section simply as a detector. This

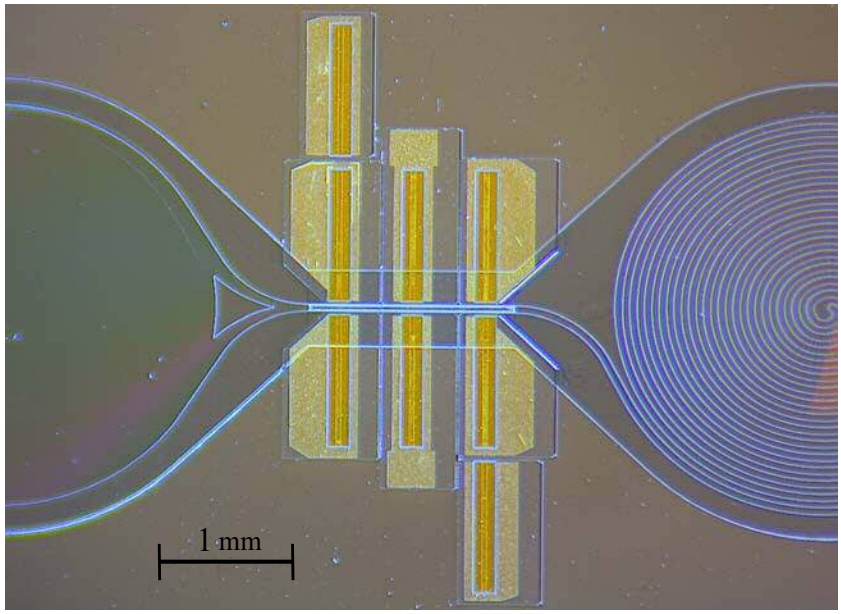

Figure 3.25: Integrated coupled-cavity lasers and on-chip detectors with capillary fill microfluidics. This optical microscope image shows the an inlet reservoir on the left, the 3D microfluidic channel in the centre between the laser sections, and the spiral outlet on the right.

enables the ability to contrast and compare the two detection mechanisms.

3.6.1 Packaging

The 12 x 12 mm^2 sample that the design in figure 3.25 is patterned onto, is cleaved to remove any unnecessary and unused substrate before mounting. This is to prevent excessive overhang on the copper header that the device is mounted directly to, as seen in figure 3.26(b). This would otherwise make forming electrical connections to the printed circuit board (PCB) extremely difficult. This copper header is mounted onto a flat copper block which is attached to the PCB via small screws. The purpose of the 3 mm high copper header is to allow for external measurements to be taken, such as lasing wavelength, without the top of the 12 way connector pins reducing measured signals or enhancing scattered light.

3.7 Summary

This chapter has provided an overview of the integrated design concept and process steps which constitute the fabrication of characterisation devices and also, an integrated coupled-cavity laser and microfluidic device for proof of principle measurements. Included in this are details of some developmental studies made to incorporate deep etched GaAs channels and 3D SU-8 microfluidic

(a) (b)

Figure 3.26: A full packaged device showing the integrated semiconductor chip mounted on a copper header and the electrical connections made to the printed circuit board from above (a) and from the side (b).

channels. Using a 5% NH_4OH/H_2O_2 etch solution, results show a mean etch rate of (0.39 ± 0.11) μm$(\text{min})^{-1}$ when used on either n-type or S-I GaAs substrates. Microfluidic channels have been fabricated on an optically active III-V substrate using a double exposure and only a single layer of photo-patternable polymer. In terms of development times of the SU-8 channels, a minimum of 45 minutes is needed to completely clear out the photoresist from the channel under the lid and channel inlet and outlet.

References

[1] H. Becker and L.E. Locascio, *"Polymer microfluidic devices"*, Talanta, vol. 56, issue 2, pp.267-287, Feb. 2002

[2] D. Schafer, E.A. Gibson, E.A. Salim, A.E. Palmer, R. Jimenez and J. Squier, *"Microfluidic cell counter with embedded optical fibers fabricated by femtosecond laser ablation and anodic bonding"*, Opt. Express, vol. 17, no. 8, pp.6068-6073, Apr. 2009

[3] G. Luka, A. Ahmadi, H. Najjaran, E. Alocilja, M. DeRosa, K. Wolthers, A. Malki, H. Aziz, A. Althani and M. Hoorfar, *"Microfluidics Integrated Biosensors: A Leading Technology towards Lab-on-a-Chip and Sensing Applications"*, Sensors (Basel), vol. 15, no. 12, pp.30011–30031, Dec. 2015

[4] S.W. Kettlitz, S. Valouch, W. Sittel and U. Lemmer, *"Flexible planar microfluidic chip employing a light emitting diode and a PIN-photodiode for portable flow cytometers"*, Lab Chip., vol. 12, no. 1, pp. 197-203, 2012

[5] R. Nagarajan, M. Kato, J. Pleumeekers, P. Evans, S. Corzine, A. Dentai, S. Murthy, M. Missey, R. Muthiah, R.A. Salvatore, C. Joyner, R. Schneider, M. Ziari, F. Kish and D. Welch, *"InP Photonic Integrated Circuits"*, IEEE Journ. Sel. Top. Quant. Electron., vol. 16, no. 5, pp. 113-1125, 2010

[6] D. Pérez-Calixto, R. Zamarrón-Hernández, A. Cruz-Ramírez, M. Hautefeuille, J. Hernández-Cordero, V. Velázquez and M. Grether, *"Fabrication of large all-PDMS micropatterned wveguides for lab on chip integration using a rapid prototyping technique"*, Opt. Mat. Expr., vol. 7, no. 4, pp. 1343-1350, 2017

[7] S. Chen, W. Li, J. Wu, Q. Liang, M. Tang, S. Shutts, S.N. Elliot, A. Sobiesierski, A.J. Seeds, I. Ross, P.M. Smowton and H. Liu, *"Electrically pumped continuous wave III-V quantum dot lasers on silicon"*, Nat. Photonics, vol. 10, no. 5, pp. 307-311, 2016

[8] R.E. Williams, *"Gallium Arsenide Processing Techniques"*, Archtech House, Boston, 2nd Edition, 1984

[9] H. Kirchauer, *Photolithography Simulation*, PhD Thesis, Institute for Microelectronics, TU Vienna, 1998

[10] M.A. McCord & M.J Rooks, *Micromachining and Microfabrication Volume 1: Microlithography*, SPIE Handbook of Microlithography, Chapter 2, 1997

[11] K. Wasa, M. Kitabatake and H. Adachi, *Thin Film Materials Technology: Sputtering of Compound Materials*, Springer-Verlag GmbH, Heidelberg, 2004

[12] D.A. Jameel, *Thin Film Deposition Processes*, Int. J. of Mod. Phys. and Apps., vol. 1, no. 4, pp.193-199, Sept. 2015

[13] AZO Materials, *Nanoscale Etching in Inductively Coupled Plasmas*, https://www.azom.com/article.aspx?ArticleID=7532, accessed 19/06/2018

[14] D. Johnson, D. Geerpuram, C. Johnson, L. Martinez and J. Plumhoff, *"The Use of Optical Emission Interferometry for Controlled Etching of III V materials"*, Conf. Proc., CS MANTECH Conference, Oregon, USA, pp.167-170, 2010

[15] J.J. Kelly, J.E.A.M. van den Meerakker, P.H.L. Notten and R.P. Tijburg, *"Wet-chemical etching of III-V semiconductors*, Philips Technol. Review, 1988

[16] C. Bryce and D. Berk, *"Kinetics of GaAs Dissolution in H2O2-NH4OH-H2O Solutions"*, Ind. Eng. Chem. Res., vol. 35, no. 12, pp 4464–4470, 1996

[17] P. Lamarre and R. McTaggert, *A Positive Photoresist Adhesion Prometer for PMMA on GaAs MESFET's*, IEEE Trans. on Electron. Devices, vol. 37, no. 11 , Nov. 1990

[18] J. Golden, H. Miller, D. Nawrocki and J. Ross, *"Optimization of Bi-layer Lift-Off Resist Process"* CS MANTECH Conf. Proc., 2009

[19] B. Cakmak, *"Fabrication and characterization of dry and wet etched InGaAs/InGaAsP/InP long wavelength semiconductor lasers"*, Opt. Exp., vol. 10, no. 13, pp.530-535, 2002

[20] M. Fikry, *"Investigations of Processing Methods for GaN-Based Laser Diodes"*, Annual Report, Institute of Optoelectronics, Ulm University, pp.27-34, 2008

[21] H.H.J. Sapingi, *"Developing coupled-cavity living laser for biological cell analysis"*, PhD thesis, Cardiff University, 2016

[22] K. Liu, X. Ren, Y. Huang, S. Cai, X. Duan, Q. Wang, C. Kang, J. Li, Q. Chen and J. Fei, *"Inductively Coupled Plasma Etching of GaAs in Cl_2/Ar, Cl_2/Ar/O_2 Chemistries with Photoresist Mask"*, App. Surf. Sci., vol. 356, pp.776-779, 2015

[23] G.T. Edwards, A. Sobiesierski, D.I. Westwood and P.M. Smowton, *"Fabrication of High-Aspect-Ratio Sub-Micron Gratings in AlGaInP/GaAs Laser Structures using a BCl_3/Cl_2/Ar Inductively Coupled Plasma"*, Semicond. Sci. Technol., vol. 22, pp.1010-1015, 2007

[24] F.J. Blanco, M. Agirregabiria, J. Garcia, J. Berganzo, M. Tijero, M.T. Arroyo, J.M. Ruano, I. Aramburu and K. Mayora, *"Novel three-dimensional embedded SU-8 microchannels fabricated using a low temperature full wafer adhesive bonding"*, J. Micromech. Microeng., 14, pp.1047-1056, 2004

[25] H. Lee, Y. Liu, D. Ham and R. M. Westervelt, *"Integrated cell manipulation system—CMOS/microfluidic hybrid"*, Lab Chip, 7, pp.331-337, 2007

[26] MicroChem Corp., *"SU-8 2000 permanent epoxy negative photoresist processing guidelines"*, Data sheet, 2015

[27] M. Nordström, A. Johansson, E. Sánchez Noguerón, B. Clausen, M. Calleja and A. Boisen, *"Investigation of the bond strength between the photo-sensitive polymer SU-8 and gold"*, Microelec. Engin., vol. 78-79, pp.152-157, 2005

[28] R. Thomas, A. Harrison, D. Barrow and P.M. Smowton, *"Photonic integration platform with pump free microfluidics"*, Optics Express, vol. 25, 20, pp.23634-23644, 2017

[29] J.M. Dykes, D.K. Poon, J. Wang, D. Sameoto, J.T.K. Tsui, C. Choo, G.H. Chapman, A.M. Parameswaren, B.L. Gray, *"Creation of Embedded Structures in SU-8"*, Proc. of SPIE Vol. 6465, pp.N-1-N-11, 2007

[30] A. Sobiesierski, R. Thomas, P. Buckle, D. Barrow and P.M. Smowton, *"A Two-Stage Surface Treatment for the Long-Term Stability of Hydrophilic SU-8"*, Surf. Interface Anal., vol. 47, pp.1174-1179, 2015

Chapter 4

Characterisation of the Active Medium

4.1 Introduction

This chapter describes the work which was carried out to establish an epitaxial structure suitable for creating an integrated microfluidic III-V coupled-cavity laser device. An epitaxial laser structure that exhibits maximum gain at a low current density and a low internal optical mode loss is advantageous, whilst a broad gain spectrum would be desirable for wavelength tuning applications in the future. However, it is essential for the performance of the coupled-cavity laser in chapter 6, that the expitaxial structure provides sufficient gain to overcome the considerable cavity losses, inherent in etched facet formation and the device design.

In principle, InAsP quantum dot (QD) structures cover wavelengths from 730 nm to 800 nm and beyond [1] [2], extending the upper limits of both compressively strained GaInP quantum well (QW) and InP QD lasers. These wavelengths cover regions of the spectrum where the optical response of blood and blood cells can provide established and understood diagnostic information, like in figure 1.3. Longer wavelengths, towards 780 nm, transmit deeper in blood [3] and microvascalature [4], and therefore has the potential for non-invasive biophotonic applications. For example, capillary blood flow measurements [5] using a similar active region can be performed at deeper depths within the human body. Relatively broad gain spectra, a characteristic of QDs, can support multi-wavelength sources that are regularly employed in physiological measurements such as arterial oxygen saturation [6].

Here we examine the suitability and limitations of different active regions, both QD and QW, for the coupled-cavity structure and select the best option to support proof of principle coupled-cavity measurements. The work carried out in this chapter builds on the recent advances that have been made using a InAsP QD structure [7], but due to device design and the inherent facet damage from fabrication required for integration, it is expected that the InAsP QDs are unlikely to achieve a net gain high enough to overcome the cavity losses. Calculations of threshold net gain for an individual laser section, using a previously published etched facet efficiency of η_f=0.48 [8], indicate that for a laser of cavity length, L=990 μm, R_1=0.28 and R_2=0.12, G_{th}-α_i=24.6 cm^{-1}. This however, does not include any additional losses that may occur in practise in the final device. It is therefore likely that the epitaxial structure will need to achieve net gain values in excess of 25 cm^{-1} for a similar laser. QWs are known to achieve higher gain magnitudes [9], and therefore may be the choice for the coupled-cavity structure.

The chapter starts with a description of the methods used in the chapter and the measurement principle behind the segmented contact method. In the following section, a description of the InAsP QD layer structures used, in terms of compositions and dimensions, where the distinction between each structure investigated is defined. This section also contains the description of the commercially available GaInP/AlGaInP QW epitaxial structure. Following on from this, results are presented on the effect of barrier width for InASP QD structures that are otherwise nominally the same, using threshold current density measurements made on corresponding edge-emitting laser devices. This is in addition to optical gain and loss measurements. The latter part of the chapter considers the optical gain measurements of the QW material and its benefit for coupled-cavity measurements in chapter 6.

4.2 Experimental Methods

4.2.1 Current-Voltage-Light-Temperature Measurements

An experimental setup, built by Dr C. Allford, was used to perform computer automated measurements of current-voltage-light (I-V-L-T) characteristics as a function of temperature. The device is placed inside an evacuated cryostat comprising of a cold finger and heating element, which allows the temperature of the device to be varied from 250-400 K. The I-V-L-T measurement uses an oscilloscope where the gates are set, to coincide with the current/light pulse of the laser device on test. The resulting I-V-L-T measurements, with a current pulse width of 1000 ns and a repetition rate of 1 kHz, applied with a pulse generator, are all recorded by the computer which increments the current supplied to the device. This is repeated until the applied current reaches a preset limit. A neutral density filter is used in conjunction with a silicon photo-detector to ensure linearity over the wavelengths measured. When the kit is used for measurements at different temperatures, the device is cooled down using liquid nitrogen, which cools the cold finger, attached to the sample. Temperatures above room temperature are achieved using a resistive heater embedded in the cold finger.

4.2.2 Segmented Contact Method

The segmented contact method is a characterisation technique whereby the single pass amplified spontaneous emission (ASE) from an edge emitting diode is measured as a function of length [10]. With round trip amplification suppressed, this method is used to characterise the net single pass modal gain, (G-α_i), modal absorption, A, and also the internal optical mode loss, α_i of both InAsP QD and GaInP QW structures.

A segmented contact structure has a single oxide stripe with a segmented p-contact along its length, seen in figure 3.11, allowing each section to be driven independently. With electrical connections to S1 and S2, the light collection is fixed as the length of the stripe is varied.

4.2.2.1 Measurement Principle

This section provides the mathematical determination of gain and absorption spectra by the segmented contact method using two identical sections. i.e. they are of equal length.

If the total spontaneous emission rate in the active region is I_{spon}, then the emission rate from an element of thickness Δx that has travelled a distance x along the active region is

$$I(x) = \beta I_{spon} \exp[(G - \alpha_i)x]\Delta x \tag{4.1}$$

where β is the fraction of spontaneous light coupled back into the waveguide, G is the modal gain and α_i is the internal optical mode loss. It can be assumed that that I_{spon} is uniform in the x direction along the stripe, and then the total ASE per unit stripe width from a length l of pumped material internally on the facet is

$$I(l) = \int_0^l \beta I_{spon} \exp[(G - \alpha_i)x]dx = \beta I_{spon} \frac{\exp[(G - \alpha_i)l] - 1}{G - \alpha_i}. \tag{4.2}$$

Equation 4.2 is the ASE on the internal facet. Externally measured ASE is given by $I_{meas} = CI(l)$, where C is an extraction factor that accounts for transmission across the semiconductor-air interface, light collection geometry and the calibration of the system. An expression for the net modal gain can be derived from equation 4.2 by solving for for l = L and l = 2L and dividing one expression by the other, giving

$$(G - \alpha_i) = \frac{1}{L} \ln\left(\frac{I_{meas}(2L)}{I_{meas}(L)} - 1\right). \tag{4.3}$$

It is possible to use similar arguments to express the net modal absorption of the unpumped gain medium, A. With section 2 pumped alone (i.e. section 1 left unpumped), this section provides ASE of the form $I_2(L)$, which is absorbed by section 1. The ASE measured externally from the facet, denoted as $I_{meas}(2)$, is

$$I_{meas}(2) = C\exp[(-A - \alpha_i)L]I_2(L) \tag{4.4}$$

Since the emission from section 1 alone, $I_{meas}(1)$ is $C(1 - R)I(L)$ and $I(L) = I_2(L)$ then

$$(A + \alpha_i) = \frac{1}{L} \ln\left(\frac{I_{meas}(1)}{I_{meas}(2)}\right). \tag{4.5}$$

Figure 4.1 shows an example of three different measured ASE spectra, all at the same current density of 167 Acm^{-2}. Using equations 4.3 and 4.5, modal gain and absorption spectra can be

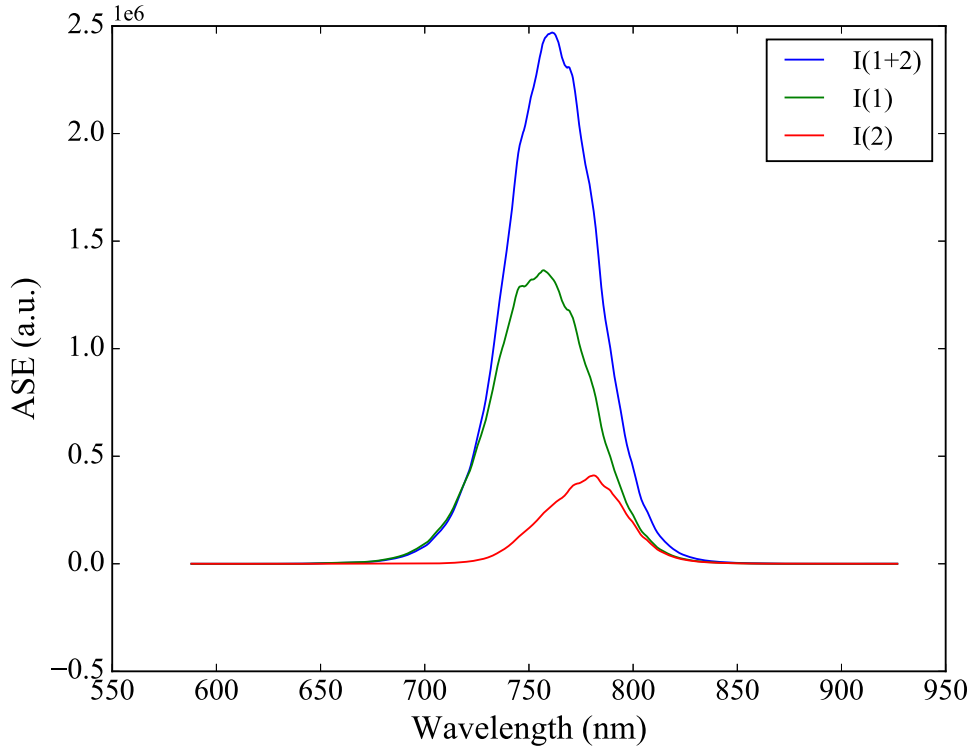

Figure 4.1: Example of measured ASE spectra for the case of pumping; section 1 on its own (green), section 2 on its own (red) and section 1 and 2 together (blue) of an InAsP QD segmented-contact device at a fixed current density. The gain spectrum derived from this data, along with other current densities, is shown in figure 4.15.

derived for a structure.

4.2.2.2 Experimental Procedure

The experimental setup in figure 4.2 used to measure ASE spectra was originally set up by Dr G.M. Lewis [11]. A 50 μm wide, oxide-isolated stripe segmented contact device, with six 300 μm long sections, is mounted onto a transistor header and placed onto a translation stage to allow for optical alignment to the spectrograph. This device is connected to a switch box and pulse generator to allow each individual section to be driven (pulsed) or grounded. Sections 1 and 2 only, the front two sections, were used for current injection in this investigation. A typical device is pulsed at 0.1 % duty cycle with a pulse width of 1000 ns. The rear absorber section of the device is grounded to suppress the round-trip amplification that would otherwise undermine the validity of the measurement. An objective lens is used to focus the ASE collected from the front facet of the device onto the entrance slit of the spectrograph through a polariser (this allows for collection of either TE and TM polarised ASE spectra depending on polariser orientation). The

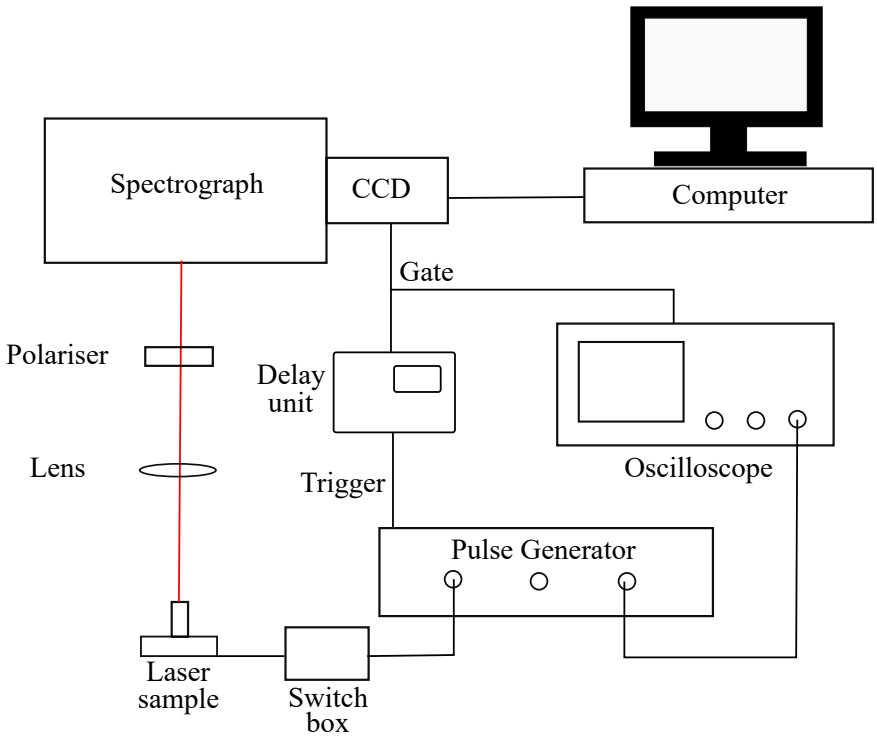

Figure 4.2: Diagram of the experimental set up to measure ASE spectra as a function of current density for segmented contact devices.

spectral components of the light incident on the spectrograph are spatially dispersed onto a charge coupled device (CCD) array with an image intensifier. This intensifier is electronically shuttered for a gated measurement by switching its accelerating voltage on and off. The measurement gate is triggered by the pulse generator via the delay unit. This must be synchronised to the drive frequency. The charge accumulated over 500 exposures, each with an exposure time of 0.1 s is read out and recorded by the computer. Before data is taken, wavelength calibration files are loaded to ensure the spectrograph is set up correctly for the specific centre wavelength to be used. Once this is completed, a background response of the spectrograph is used to correct the final data set.

4.2.3 Emission Spectrum Measurements

To measure a wavelength emission spectrum for each laser, the set-up shown in figure 4.3 was used. Each sample was pumped at a current 10% above its lasing threshold current using a pulse generator and the resulting optical signal is focussed onto an optical fibre. This signal is recorded by an optical spectrum analyser, using a resolution of 0.05 nm. An example spectrum is shown in figure 4.4, where the emission wavelength is obtained as the x-coordinate at the peak of the

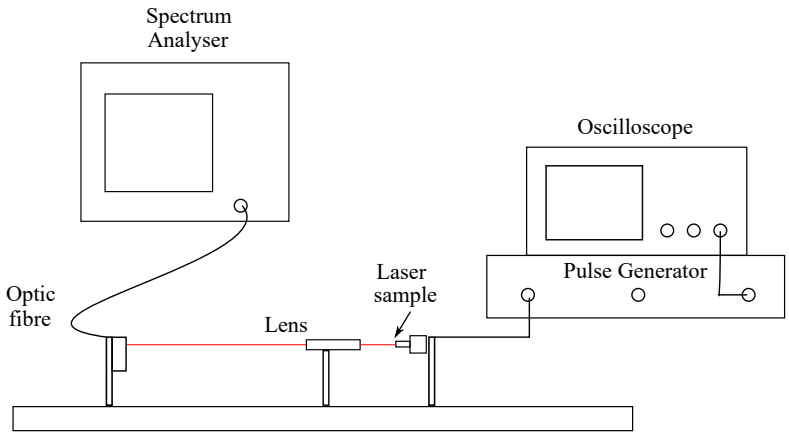

Figure 4.3: Diagram of the experimental set up to measure emission wavelength spectra.

intensity, in this case 654.8 nm.

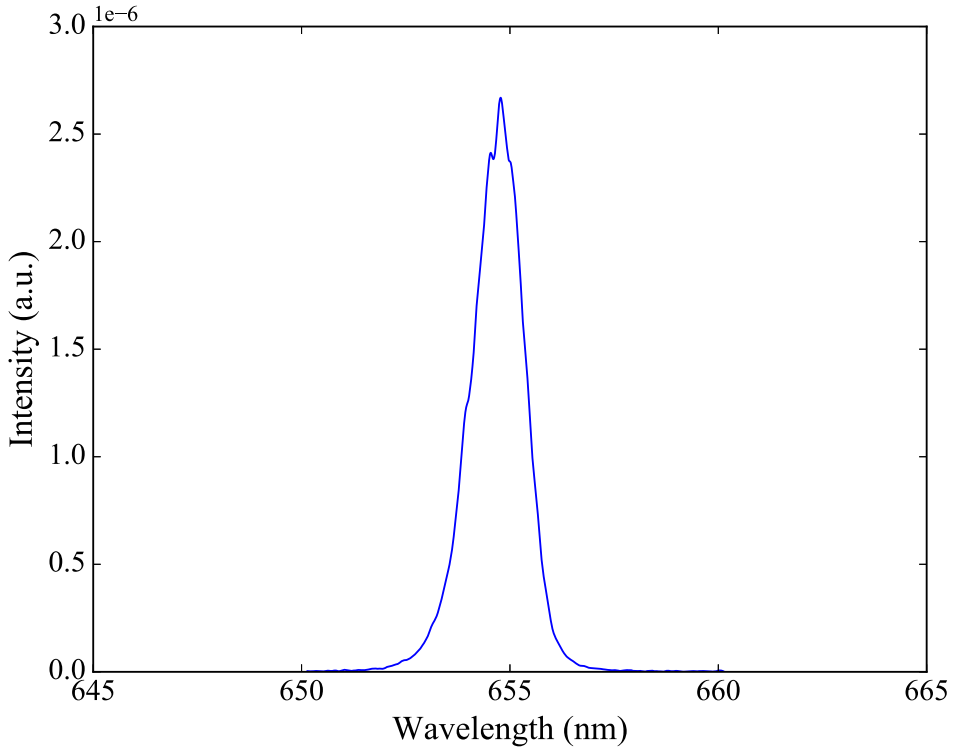

Figure 4.4: An example wavelength emission spectrum.

4.3 Epitaxial Structures

4.3.1 InAsP QDs

The self-assembled InAsP QD structures were grown by metalorganic vapour phase epitaxy (MOVPE) at the EPSRC National Epitaxy Facility in Sheffield. The epitaxial layers were grown on n-type GaAs (100) substrates orientated 10 ^{o} off toward <111>. During the growth of the core regions, the flow of phosphine was kept constant at 300 sccm and an arsine flow of 8 sccm was introduced during the growth of the InAsP layers, at a temperature of 730 ^{o}C. The active region consists of 5 InAsP QD layers with a tensile strained $Ga_{0.56}In_{0.48}P$ quantum well of a thickness of 8 nm grown above each QD layer and separated by a $(Al_{0.3}Ga_{0.7})_{0.52}In_{0.48}P$ barrier of either 8, 16, or 24 nm. The width of the active layer in the 8 nm, 16 nm and 24 nm samples is 396 nm, 428 nm and 460 nm respectively. The rest of the waveguide is composed of 900 nm wide $Al_{0.52}In_{0.48}P$ cladding layers. A schematic of this structure is shown in figure 4.5.

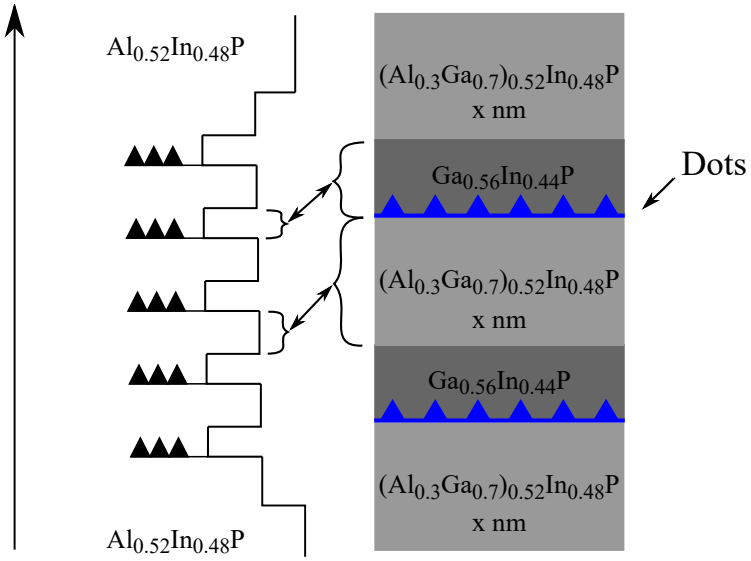

Figure 4.5: Schematic of the epitaxial growth structure with growth direction in the vertical plane. The triangular shapes represent the quantum dots within the GaInP quantum wells. The width, x, of the AlGaInP barrier is equal to 8, 16 and 24 nm in the three comparison structures respectively.

4.3.2 GaInP QWs

The GaInP/AlGaInP QW structure investigated in this chapter was from a commercially available wafer aquired from IQE plc. The epitaxial layers are on n-type GaAs (100) substrates orientated

10^{o} off toward <111>. The active region consists of 3 compressively strained $Ga_{0.46}In_{0.54}P$ QWs, each being 6.5 nm thick and separated by a 7 nm $(Al_{0.5}Ga_{0.5})_{0.51}In_{0.49}P$ barrier. The width of the active layer in this structure is 403 nm. A schematic of this structure is shown in figure 4.6.

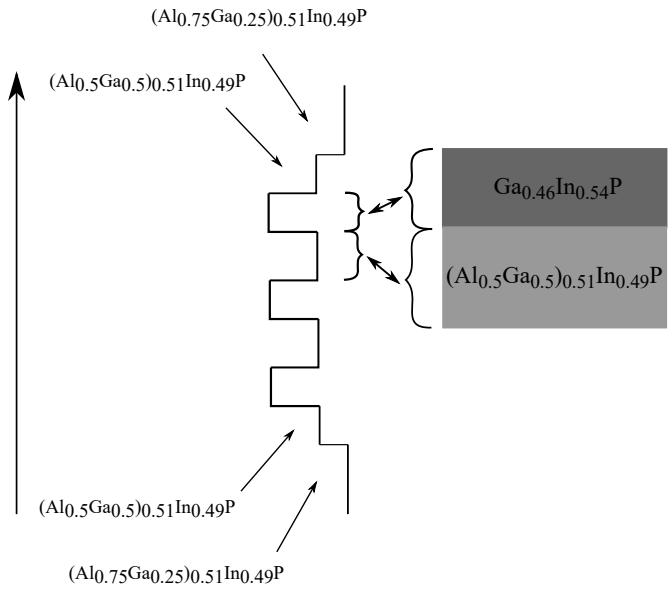

Figure 4.6: Schematic of the epitaxial growth structure of the GaInP quantum well wafer with growth direction in the vertical plane.

4.4 Effect of Barrier Width

Comparison of barrier widths between dot layers has previously been done in the well studied InP/AlGaInP material system [12]. However, the lattice mismatch to GaAs that is introduced by the incorporation of arsenic to InP QDs, brings about smaller dots than InP alone, and therefore the effect of barrier widths, and potentially dot states, on this size of dot is unknown.

This section quantifies the effect of varying the barrier width, using 8 nm, 16 nm and 24 nm wide barriers between layers of InAsP QDs; the structures of which are detailed in section 4.3.1. Results presented show the lasing threshold current density as a function of temperature, the lasing wavelength, the modal loss, net modal gain and internal optical loss of each barrier width.

4.4.1 Threshold Current Density

Measurements are presented on the temperature dependence of threshold current density, J_{th}, for lasers with a 2 mm cavity length, as a means to compare the performance of each laser material. This section attempts to explain the origin of the temperature dependence of J_{th} in InAsP QD lasers of varying barrier width. The three laser structures, with 8 nm, 16 nm and 24 nm wide barriers, described in section 4.3.1, were cleaved into 2 mm long devices, with multiple devices being mounted for experimental testing. To calculate the J_{th} of each device, the measured threshold current is divided by the product of the device length and the mode width. The mode width, w, of each of the devices has been calculated by measuring the full width half maximum values of the near-field intensity distributions across the facet of the device. The length, L, of each device has been measured using a calibrated optical microscope. Current-voltage characteristics were taken before any other measurements to ensure they were suitable for further analysis. This ensures the electrical contacts on the device are ohmic, to ensure lasing action can be achieved. J_{th} as a function of temperature for each structure is presented in figure 4.7.

Table 4.1: A summary of lasing threshold current densities as a function of barrier width at 300 K for a 2 mm long laser cavity.

Barrier Width (nm)	Threshold Current Density (Acm^{-2})
8	207
16	323
24	318

A QD laser has the potential to offer a J_{th} independent of temperature based on an idealised dot structure, where all ground states are at the same energy and the excited states are far enough away in energy not to be populated. However, in a real QD system, this is not realised. The super-linear behaviour of J_{th} with temperature in all structures in figure 4.7 above 300 K is observed because of the increase in non-radiative recombination current density due to thermal spreading across the inhomogeneous distribution [13]. The high density of states in the wetting layer (or quantum well) can also increase J_{th} by limiting the available gain from the QDs, where the leakage of carriers from the QDs to states in the QW depends exponentially on temperature. The non-radiative re-

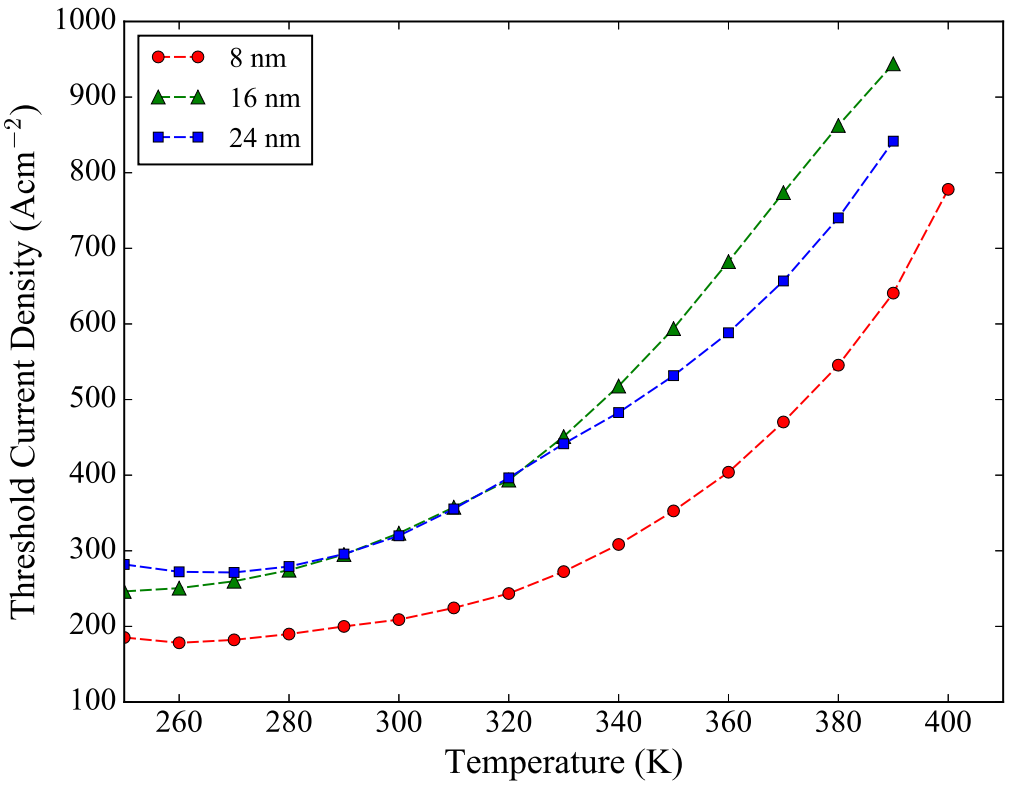

Figure 4.7: Threshold current density as a function of temperature (250-400 K) for 2 mm long lasers with different barrier widths; 8 nm (red circles), 16 nm (green triangles), 24 nm (blue squares).

combination is further increased due to the population, and subsequent recombination, in excited dot and wetting layer states [14]. Below 300 K there is a more linear temperature dependence due to recombination within the quantum dots. Table 4.1 summarises J_{th} for each laser device at 300 K; J_{th} increases as the barrier width is increased, but 16 and 24 nm barriers have very similar J_{th} values. This is seen to be consistent for the 280 to 330 K temperature region in figure 4.7.

Historically, the temperature dependence is represented by the relation [15]

$$\frac{1}{T_0} = \frac{1}{J_{th}} \frac{dJ_{th}}{dT} \tag{4.6}$$

where T_0 is the characteristic temperature [16] and can be extracted from a log-plot of J_{th} versus temperature, T. However, this relationship applies to an exponential increase in J_{th} with T [13], which is not seen in the characteristics of figure 4.7. T_0 can be measured over a specific T interval, but values can vary depending on the chosen interval and therefore, a single T_0 can not be found for these InAsP QD lasers.

To investigate temperature dependence of J_{th} on T further, and to identify the origin of the rate-limiting loss mechanism from the InAsP QD system above 300 K, the activation energy, E_a, for each barrier width can be calculated. Typically, the loss mechanism in red-emitting lasers comes from the loss of carriers from the well to the barrier. With the addition of QDs to the structure, however, it is unclear as to whether the loss mechanism is still QW to barrier or QD to QW or even a combination of both. E_a can be calculated by following the method set out in [17]. Essentially, an excess current density at high temperatures can be obtained by subtracting a linear extrapolation of J_{th} between 200 K and 280 K (the straight line region) by use of a straight line fit, as seen in figure 4.8.

Here, the Boltzmann approximation can be used to model the carrier density in the barrier in equilibrium with the well, due to the Fermi level separation being much smaller than the band gap of the barrier material. The recombination rate for a "bulk" barrier material is given by

$$R_b = CT^{3/2} \exp\Big(-\frac{E_{gb} - \Delta E_F}{k_b T}\Big) \tag{4.7}$$

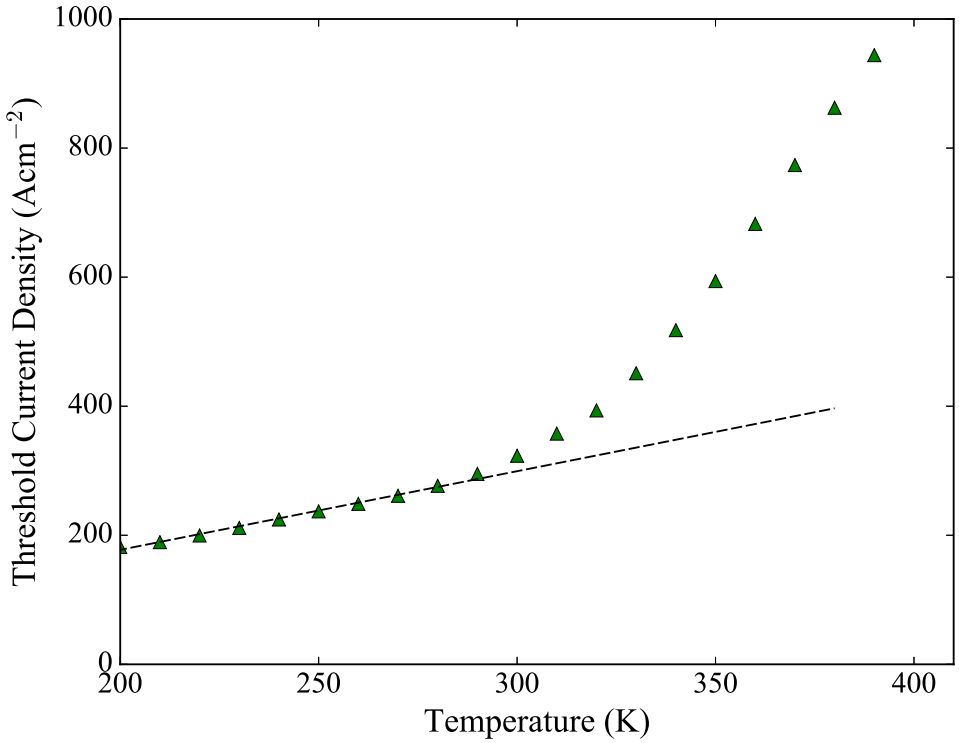

Figure 4.8: Straight line fit (black dashed line) between 200 and 280 K to allow analysis of leakage of carriers from the quantum well by subtracting this linear extrapolation at higher temperatures.

where E_{gb} is the barrier material band gap, ΔE_F is the quasi-Fermi level separation, T is the temperature, k_b is the Boltzmann constant and C is factor containing temperature-independent terms.

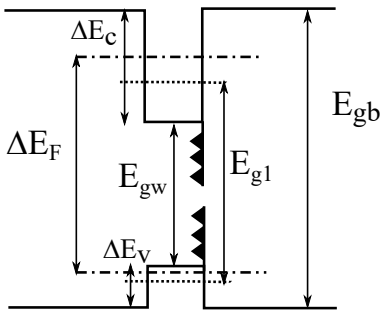

Figure 4.9: Schematic showing the energy gaps of the barrier (E_{gb}), the well (E_{gw}) and the n=1 sub-band (E_{g1}) and the quasi-Fermi level separation (ΔE_F) and the dots in the well (triangles).

Since the effective density of states of the barrier is proportional to $T^{3/2}$ an Arrhenius plot of $\ln(J/T^{3/2})$ versus $1/k_bT$ gives an activation energy theoretically equal to $E_{gb} - \Delta E_F$ from its gradient. A plot of this is found in figure 4.10. Activation energies are found to decrease with an

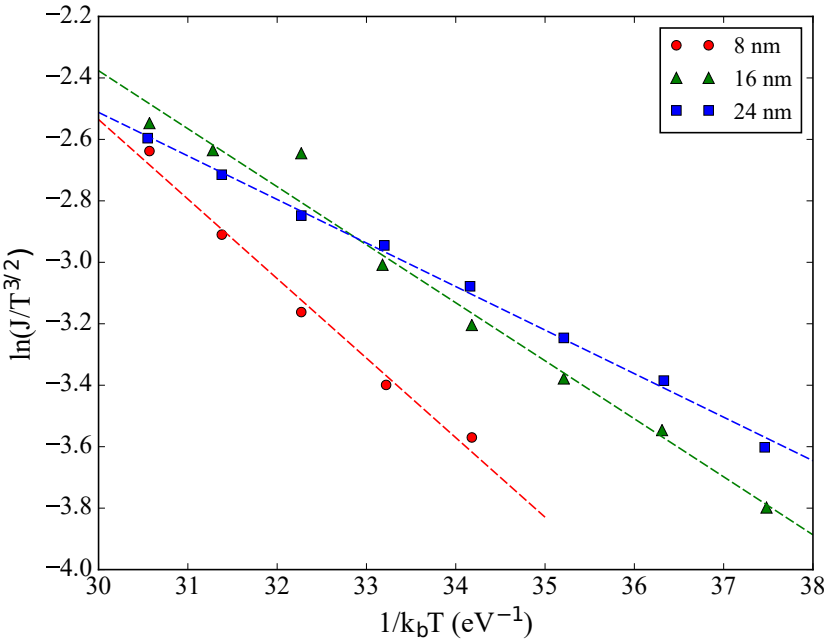

Figure 4.10: Arrhenius plot of the form $J/T^{3/2}$ versus $1/k_bT$, where J is the excess current density after the straight line extrapolation is removed, in order to extract the activation energies from a least squares fit of the data.

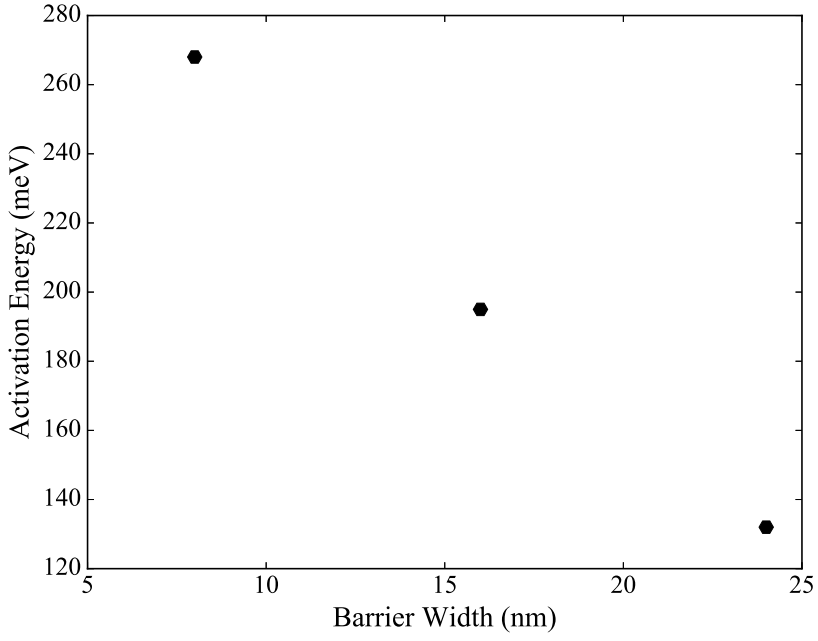

Figure 4.11: Activation energies as a function of barrier width from the Arrhenius analysis (in figure 4.10) of the excess threshold current density at high temperatures.

increasing barrier width. Energies, plotted in figure 4.11, decrease from 268 meV for 8 nm to 132 meV for 24 nm barrier widths. The magnitude of the 8 nm barrier width sample's activation

energy is consistent with the loss of carriers from the InAsP QDs to the GaInP QW. It is likely that with this barrier width, the QWs have a higher degree of coupling than in wider barrier width structures, with the 24 nm barrier width potentially acting as 5 single QWs. This increase of coupling would result in a larger splitting of energy levels, depicted in figure 4.12, resulting in a lower ground energy state. This is consistent with a higher activation energy due to the now increased barrier height for carriers to escape to the barrier, indicated by the red arrow in figure 4.12.

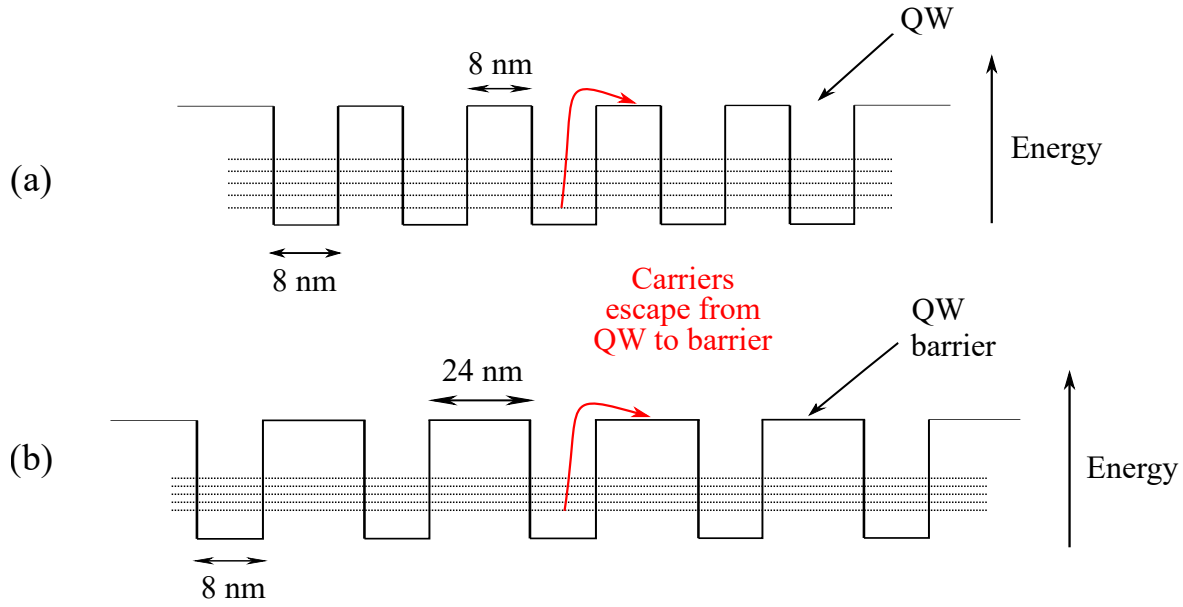

Figure 4.12: Band diagram schematic of an active region with 5 8 nm wide QWs with (a) 8 nm and (b) 24 nm wide barriers between each QW. The dashed lines indicate the energy level splitting in each case, where the increased coupling in (a) creates larger energy level separations and a lower ground state energy level than (b). The red arrow indicates the path of escaping carriers from the QW to the barrier, where the barrier height is determined by the energy difference between the QW ground state and the barrier. This is smaller in the case of (a), the smaller barrier width.

4.4.2 Wavelength

The emission spectra for lasers with varying barrier width were measured using the experimental set up shown in figure 4.3. Figure 4.13 shows that the lasing wavelength is blue-shifted with an increase in barrier width, with exact values summarised in table 4.2. The longer lasing wavelength of the 8 nm barrier coincides with the lower J_{th} value at 300 K in table 4.1. However, from J_{th} alone, it would be expected for the 16 nm barrier laser to have the shortest wavelength due to its higher, albeit only slightly, J_{th} over the 24 nm barrier laser. There is a 7 nm blue shift of the wavelength between 8 and 16 nm barrier widths, and a further 3.5 nm shift for the 24 nm sample.

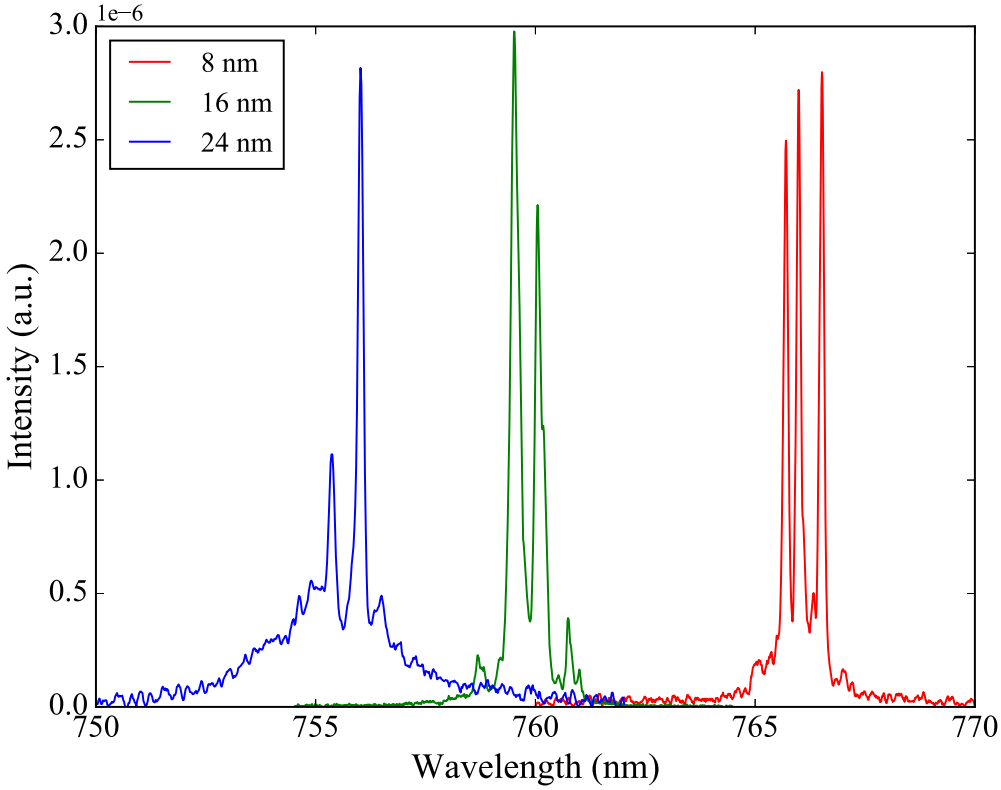

Figure 4.13: Wavelength emission spectra at 300 K for 2 mm long lasers with barrier widths of 8 nm (red line), 16 nm (green line) and 24 nm (blue line).

4.4.3 Gain and Absorption Measurements

To understand how the barrier width affects the optical properties of the epitaxial structure, it is necessary to measure the optical loss and gain using the segmented contact method detailed in 4.2.2.

4.4.3.1 Net Modal Absorption

The spectra obtained using the experimental procedure in section 4.2.2.2 and equation 4.5 for the InAsP QD structures are in figure 4.14. The modal absorption is a function of available transitions between states in the material when the epitaxial structure is unpumped and figure 4.14 shows the difference in these states between structures with 8 nm, 16 nm and 24 nm wide barriers at 300 K. The results shown in figure 4.14 indicate broad spectra for all barrier widths. This broadening is consistent with a large variation in dot sizes that has been previously observed in TEM images of InAsP QDs [18]. Although the 8 nm sample appears to be featureless, slight features at longer wavelengths can be seen in the 24 nm and 16 nm barrier width samples. The feature around 760

Table 4.2: A summary of lasing wavelength and energy as a function of barrier width at 300 K for a 2 mm long laser.

Barrier Width (nm)	Wavelength (nm)	Energy (eV)
8	766.5	1.644
16	759.5	1.637
24	756.0	1.622

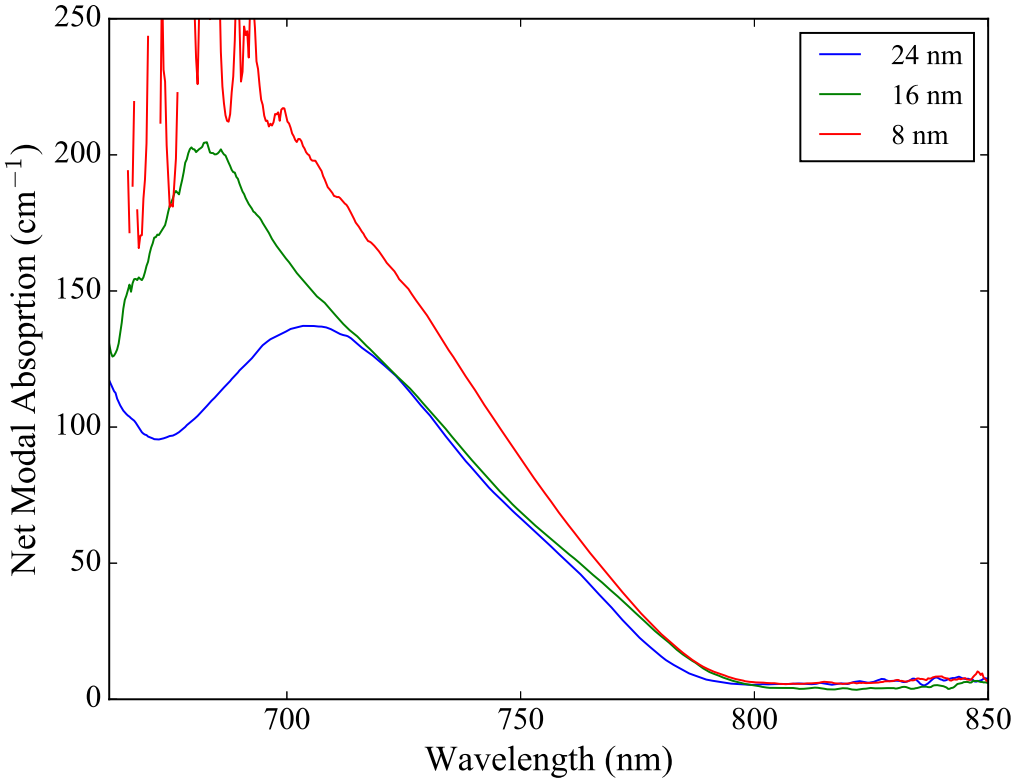

Figure 4.14: The positive net modal absorption for InAsP/AlGaInP QD structures with barrier widths of 8 nm (red line), 16 nm (green line) and 24 nm (blue line).

nm corresponds to the inhomogeneously broadened ground state of the large dot subset [19]. As the barrier width decreases, the absorption spectrum becomes appreciably broader and the ground dot states shift to lower energies (or longer wavelength as in figure 4.14). The magnitude of this wavelength shift is consistent with the effect of barrier width on lasing wavelengths previously seen in figure 4.13. The broader spectrum of the 8 nm sample is indicative of an increase in dot density, but the change in wavelength of the large dot subset ground state could also indicate an

increase in dot size. The increase in absorption for the 24 nm sample at short wavelength (around 660 nm) is the onset of the absorption from the $Ga_{0.56}In_{0.44}P$ QW. It is unclear whether the absorption edge is affected by a change in the barrier width as either the measured signal was too small for analysis or not within the measured wavelength range.

Although the narrower 8 nm barrier means that a larger number of dot layers can be deposited for the same active layer thickness, it is likely that this width is insufficient to prevent one dot layer from influencing the formation of the next [20]. The absorption spectrum below the band edge tends towards the value of α_i and extracted values indicate an internal optical mode loss, α_i of (6.1 $\pm$ 0.3) cm^{-1}, (4.1 $\pm$ 0.4) cm^{-1} and (5.6 $\pm$ 0.2) cm^{-1} for 8 nm, 16 nm and 24 nm samples respectively. α_i appears not to be significantly affected by varying the width of the barrier, indicating that the inter-layer effect is less pronounced than seen with InAs dots [21].

4.4.3.2 Net Modal Gain

Optical gain spectra of the different barrier width structures are also studied at 300 K using the segmented contact method by means of equation 4.3. The TE polarised net modal gain as a function of photon energy is plotted in figures 4.15 (a), (b) and (c), for the 8 nm, 16 nm and 24 nm wide barrier InAsP QD samples respectively.

In general, as can been seen in figures 4.15 (a), (b) and (c), an increase in the injected current causes a peak-gain shift to higher energies, or a blue-shift in the wavelength. This is a consequence of inhomogeneously broadened dot states that occur due to the statistical fluctuation in dot size [22] and the resultant state-filling effect. The peak-gain also shifts to higher magnitudes with an increase in injected current, due to injected carriers now being able to now fill higher energy states. To illustrate the wavelength dependence of InAsP QDs on peak-gain magnitudes, the peak net modal gain versus spectral position is plotted in figure 4.16. It is clear from figure 4.16 that the variation of peak gain wavelength with barrier width depends on the magnitude of the peak net modal gain. The 8 nm barrier sample shows a more rapid change in spectral position at higher injection levels (higher magnitude of peak net modal gain) above 8-10 cm^{-1}. This rate of change of the peak net modal gain, seems to reflect the steepness of the absorption edge in figure 4.14. The 8 nm barrier sample achieves the highest peak net modal gain, but below 6 cm^{-1} it is comparable to the 24 nm sample. The samples with 16 nm and 24 nm barriers appear to have a

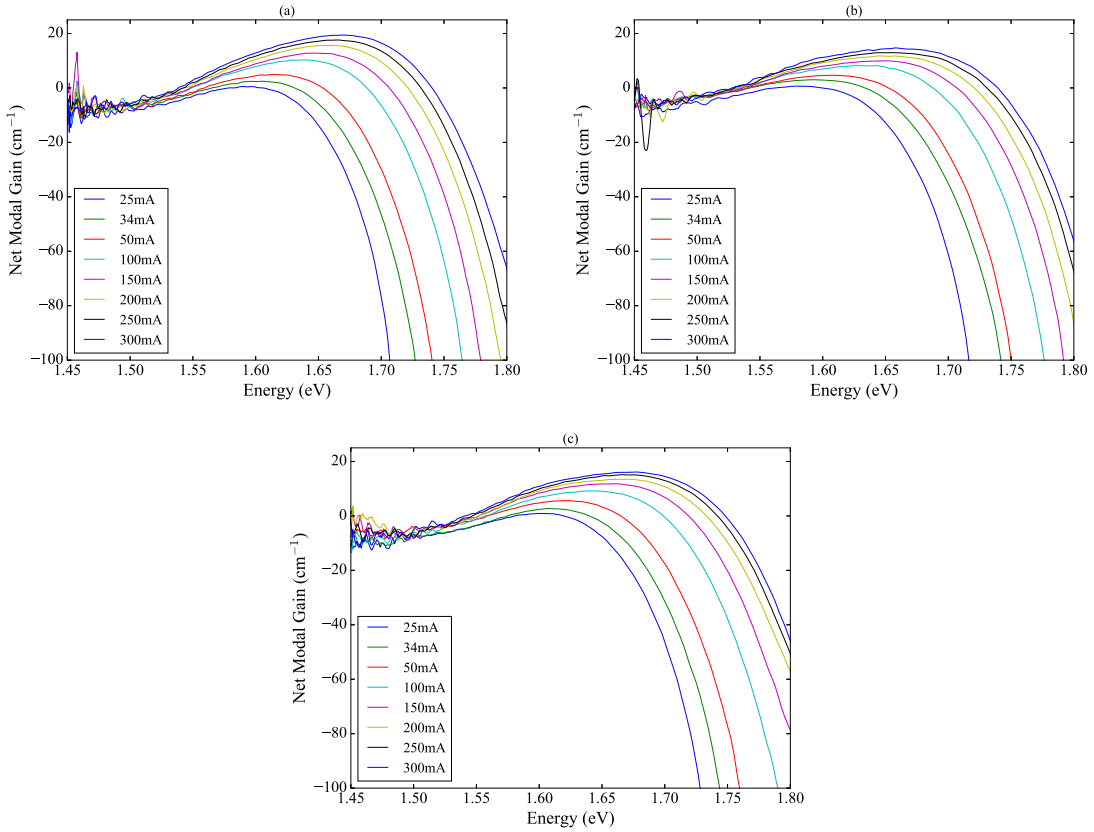

Figure 4.15: Net modal gain spectra at 300 K, for increasing injection current using the segmented contact method with a InAsP/GaInP QD sample with (a) 8 nm, (b) 16 nm and (c) 24 nm wide barriers.

relatively constant gradient at all injection levels, indicating the peak-gain wavelength is relatively unaffected by injection level. Above 7 cm^{-1} the 16 and 24 nm samples have an almost identical change in spectral position, only differing at longer wavelengths.

The peak net modal gain for each barrier width at 300 K, from figures 4.15 (a), (b) and (c), are plotted against current density in figure 4.17. At low current densities, the gain is dominated by ground state transitions of the large dot subset, but as the current density is increased, there is a clear change in the gain-current density dependence. This is a result of a significant contribution from excited state transitions with a higher density of states and therefore higher saturated gain [23]. The results for the 8 nm sample (red points) in figure 4.17 correlates to what was seen in figure 4.16, with more gain available from the ground state. It reaches a higher magnitude of net modal gain at all injected current densities above 500 Acm^{-2}. A higher gain requirement means that the level of inversion must be increased by injecting more carriers. What is apparent is that

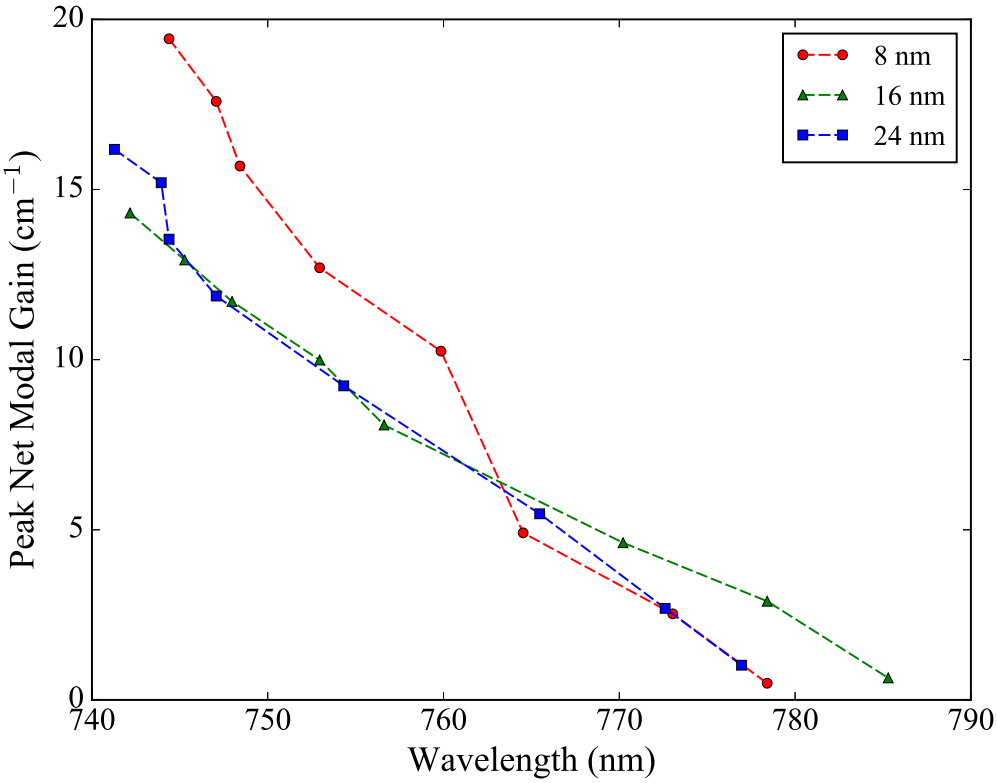

Figure 4.16: The relationship between the magnitude of the peak net modal gain and its spectral position with a variation in barrier width at 300 K.

all three barrier widths have very similar characteristics, especially at low net modal gain values (≤ 6 cm^{-1}). Each curve is fitted using the empirical relation [24]

$$G_{pk} = G_0 \left\{ 1 - \exp\left[\frac{-\gamma(J - J_{tr})}{J_{tr}} \right] \right\} \tag{4.8}$$

where G_{pk} is the peak gain level, G_0 is the saturation gain level and J_{tr} is the transparency current density. The γ factor in equation 4.8 is an additional parameter related to the linear gain region. In an ideal system, i.e. an ideal QD ensemble, γ is 1, and a value less than this is indicative of excited state or wetting layer recombination [**?**]. However, this relation only gives a reasonable representation of net modal gain at either low or high current densities, as seen by the low current density fit in figure 4.17 indicated by dashed lines. Table 4.3 gives the ground state gain parameters extracted, for samples with varying barrier width, from fitting equation 4.8 to the experimental gain-current density relationship in figure 4.17. As expected, G_0 is the highest for the 8 nm sample due to its higher achievable net peak modal gain, related to the higher number of transitions apparent in its absorption spectrum. The value of J_{tr} decreases as barrier width is increased from

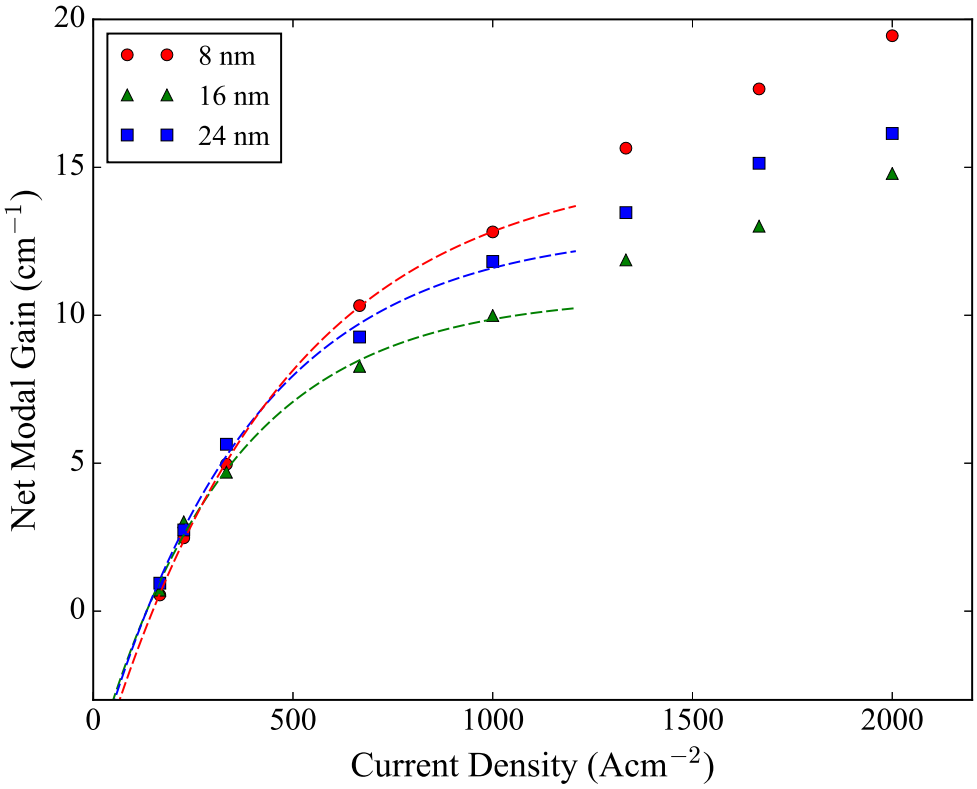

Figure 4.17: Peak net modal gain as a function of current density obtained from segmented-contact measurements in figures 4.15 (a), (b) and (c), comparing the effect of barrier width. The dashed lines represent the curve fits at low current density for 8 nm (red dashes), 16 nm (green dashes) and 24 nm (blue dashes) wide barriers using equation 4.8.

Table 4.3: Gain parameters estimated by fitting the experimental gain-current density ground state relationship of InAsP/GaInP QD lasers at 300 K to equation 4.8.

Barrier Width (nm)	G_0 (cm^{-1})	γ	J_{tr} (Acm^{-2})
8	15.2	0.32	149
16	10.7	0.40	134
24	13.0	0.35	134

149 Acm^{-2} for 8 nm to 134 $^{-2}$ for both 16 nm and 24 nm, which is consistent with a decreasing number of states with increasing barrier width as seen in the absorption spectra of figure 4.14. The non-ideality parameter, γ, is lowest for 8 nm indicating that either excited dot states, QW states or both lead to gain saturation. Since current density includes both radiative and non-radiative processes, it is unclear at this stage as to the cause of higher J_{th} and γ values for 24 nm compared

to 16 nm. The quasi-Fermi level separation, ΔE_F, can be extracted as an effective measure to indicate the relative performance expected without non-radiative processes. ΔE_F is equal to the photon energy at which the material gain is zero (net gain = -α_i), i.e. transparency. To compare the intrinsic performance, the peak modal gain is plotted against ΔE_F for each barrier width in figure 4.18.

In figure 4.18, the gain at low values of quasi-Fermi level separation are very similar and the magnitude of peak modal gain of 8 nm is higher than that of 16 nm or 24 nm, which are both consistent with results previously seen. This behaviour is consistent with the larger number of transitions at lower energy indicated by the absorption spectra of figure 4.14.

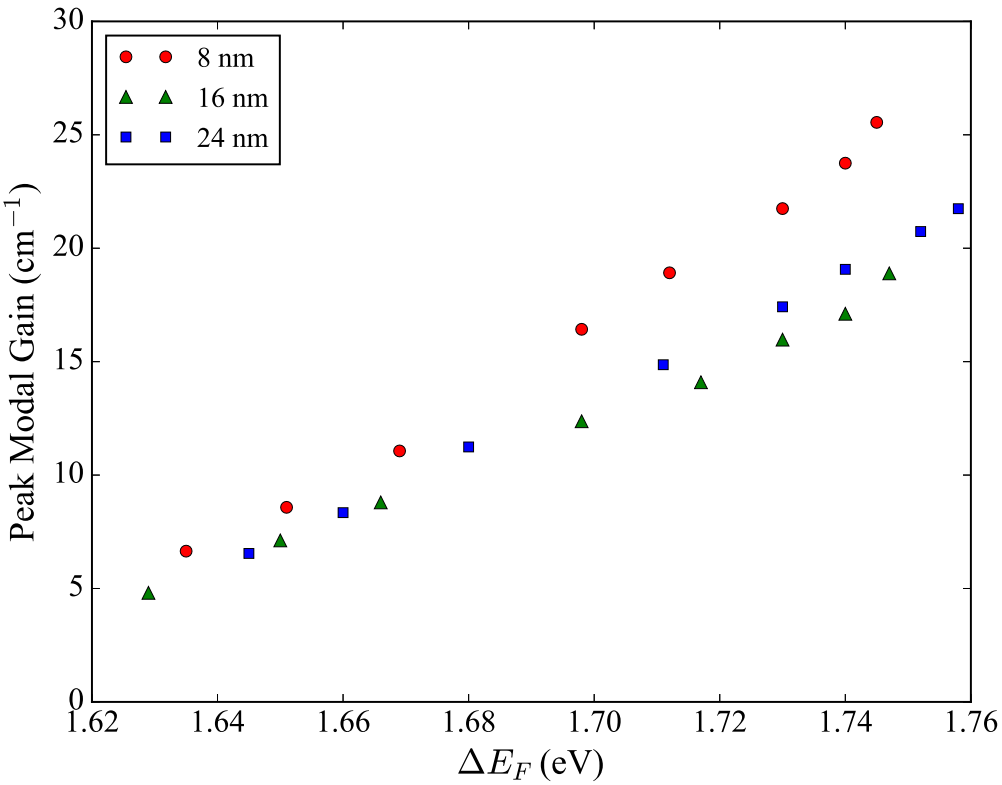

Figure 4.18: Peak modal gain (Net $G = \alpha_i$) as a function of quasi-Fermi level, ΔE_F, for 8 nm (red circles), 16 nm (green triangles) and 24 nm (blue squares) barrier widths.

4.5 Optical Gain Properties of Quantum Wells

It is expected each individual laser section will require a threshold net gain in excess of 25 cm^{-1} (incorporating previously investigated etched facet efficiencies [8]). Although the QD structure

with 8 nm barriers would be the most appropriate for a coupled-cavity proof of principle, this works shows that net gain values of this magnitude would be hard to achieve from the InAsP QDs. On account of this, this section investigates optical gain measurements of the QW structure described in 4.3.2.

The same experimental procedure as described in section 4.2.2.2 is applied to the QW segmented-contact samples, and by means of equation 4.3, the TM polarised net modal gain is calculated for each injection current from ASE spectra, such as those presented in figure 4.1. This is presented in figure 4.19. For all injected currents at lower energies (<1.85 eV), the gain spectra converge in this instance, to a net modal gain of (-5.7 $\pm$ 2) cm^{-1}. Figure 4.19 illustrates some typical differ-

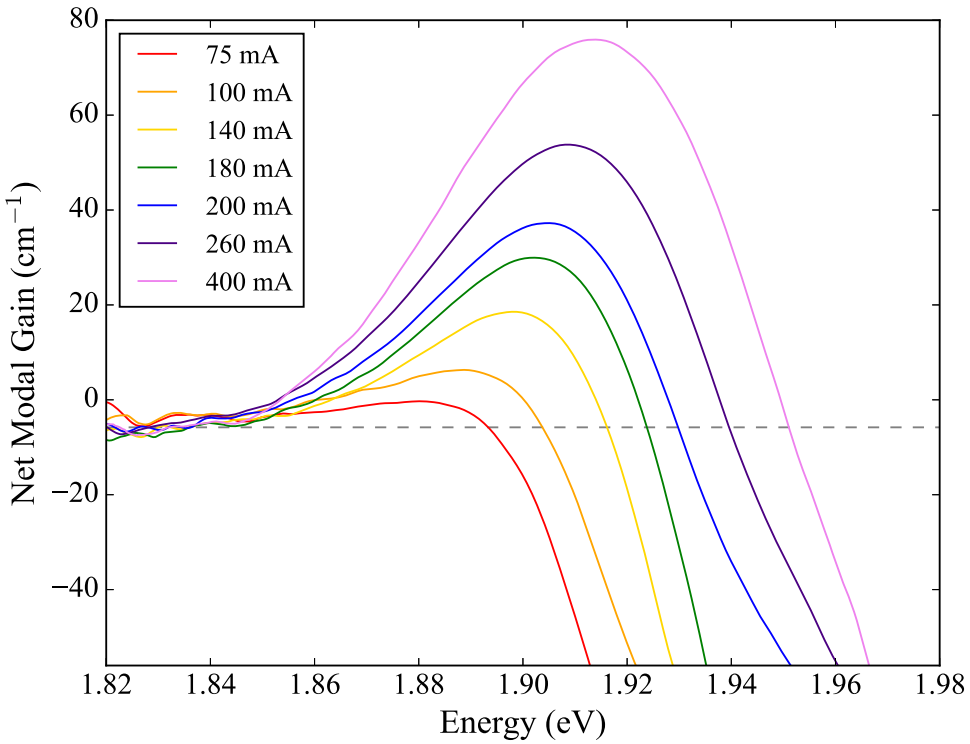

Figure 4.19: The measured net modal gain spectra for a GaInP/AlGaInP MQW structure at (300 $\pm$ 6) K, showing how the internal optical mode loss is found at low energies (dashed grey line). For this material structure, α_i = (5.7 $\pm$ 2) cm^{-1}.

ences between QW spectra and the QD spectra previously seen in figure 4.15 (a). The QW spectra are narrower, but still broaden with increasing injected current due to the heterogeneity of QW widths [25] and an increasing contribution of higher energy states [26]. Comparison of peak-gain magnitudes (with figure 4.15 (a)) demonstrate increased values for the QW, with a difference of

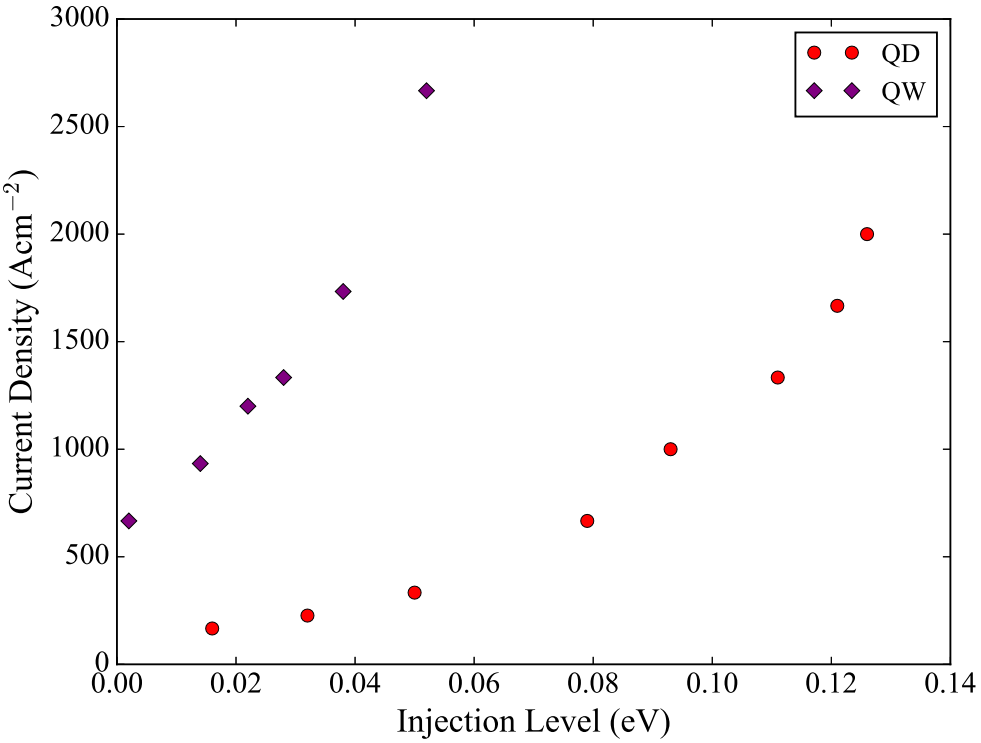

Figure 4.20: Current density versus injection level for both GaInP QW (purple diamonds) and InAsP QD (red circles) samples.

21 cm^{-1} between samples at the same current (200 mA). The applied current density for both QW and QD sample is plotted against injection level in figure 4.20. Here, the injection level is quantified by measuring the transparency point with respect to the absorption edge, i.e. Injection Level = Transparency Point - Absorption Edge. The condition that gain can only be achieved at energies below the transparency point was stipulated by Bernard and Duraffourg, stating that the quasi-Fermi level separation must be greater than the energy of the photons released (equation 2.1). The data shows that for a constant injection level, the QW sample requires a much higher current density than QD; an increase in current density of over 2000 Acm^{-2} is needed to achieve a 0.05 eV injection level. QWs have an increased number of states compared to QDs and therefore a larger number of states at any given energy allowing for higher achievable gain.

Data in figure 4.19 indicates GaInP QW samples will lase at a shorter wavelength ($\approx$ 650 nm) than the InAsP QDs. Although longer wavelengths have more beneficial biological applications as mentioned previously, 650 nm is still useful in biophotonics. The high level of absorbance of oxyhaemoglobin [27] at this wavelength and its place in the first near-infrared window, used in

imaging tissue [28], along with the high magnitude of gain, make this QW structure suitable for my proof of principle integrated coupled-cavity laser device.

4.6 Summary

In this chapter, the optical properties of different laser structures have been investigated with the motivation to establish a suitable active region for an integrated microfluidic device to use for coupled-cavity measurements. The range of wavelengths that can be accessed, as well as the threshold current dependencies and optical gain, are all important factors to consider when choosing the III-V structure.

The effect different barrier widths, of 8 nm, 16 nm and 24 nm, have on the performance of laser devices in terms of threshold current has been investigated. Measurements revealed that reducing the barrier widths to 8 nm from 16 nm, improved the performance of a 2 mm laser. The lasing wavelength has been shown to increase in blue-shift with increasing barrier width, and is attributed to a shift in the ground state transitions of the large dot subset, as seen in the absorption spectrum of each barrier width sample. These measurements also revealed an increase in inhomogeneous broadening of the large dot ground state with a decrease in barrier width, and given the larger magnitude, indicate an increase in the dot density in the dot subset. The improved performance of the 8 nm is essentially due to the shift of the dot ground states to longer wavelength and the reduced leakage of carriers, evidenced by increased activation energy to well states that remain at a fixed energy.

Measurements of modal gain of each barrier width, suggest that the performance of 16 nm and 24 nm barrier width samples are very similar. The 8 nm sample achieves higher gain magnitudes and is seen as the most attractive structure to be used in the coupled-cavity device. However, the achievable modal gain, of even the 8 nm barrier InAsP QD structure, is insufficient to overcome the considerable cavity losses calculated for the final device. For QD structures to be included in future work, they would need to provide a net gain in excess of 25 cm^{-1}, where currently, the maximum net gain measured (at 2000 Acm^{-2}) is less than 20 cm^{-1}. Consequently, the optical gain properties of a commercially available red-emitting GaInP/AlGaInP QW structure were investigated and compared to those of the investigated QDs. It was found that the QW sample,

although having higher threshold current densities, will provide sufficient gain for the microfluidic coupled-cavity device and will be used in the proceeding chapters.

References

[1] I. Karomi, *"Design and Analysis of Quantum Dot Laser (InAsP) for Bio-photonic and Mode-Locking Applications"*, PhD thesis, Cardiff University, 2018

[2] S. Haffouz, K.D. Zeuner, D. Dalacu, P.J. Poole, J. Lapointe, D. Poitras, K. Mnaymneh, X. Wu, M. Couillard, M. Korkusinski, E. Schöll, K.D. Jöns , V. Zwiller and R.L. Williams† *"Bright Single InAsP Quantum Dots at Telecom Wavelengths in Position-Controlled InP Nanowires: The Role of the Photonic Waveguide"*, Nano Lett., vol. 18, no. 5, pp. 3047–3052, 2018

[3] A. Roggan, M. Friebel, K. Dörschel, A. Hahn and G. Müller *"Optical Properties of Circulating Human Blood in the Wavelength Range 400-2500 mn"*, Journ. of Biomed. Opt., vol. 4, no. 1, pp.36–46, 1999

[4] N. Bashkatov, E.A. Genina, V.I. Kochubey and V.V. Tuchin, *"Optical properties of human skin, subcutaneous and mucous tissues in the wavelength range from 400 to 2000 nm"*, J. Phys. D: Appl. Phys, vol. 38, pp. 2543–2555, 2005

[5] M.J. Leahy, "Microvascular blood flow: microcirculation imaging", *Handbook of Biophotonics*, Wiley-VCH Verlag GmbH & Co, Weinheim, 2013

[6] I. Yoshiya, Y. Shimada and K. Tanaka, *"Spectrophotometric monitoring of arterial oxygen saturation in the fingertip"*, Medic. and Bio. Engin. and Comp., vol. 18, iss. 1, pp. 27-32, 1980

[7] A.B. Krysa, J.S. Roberts, J. Devenson, R. Beanland, I. Karomi, S. Shutts and P.M. Smowton, *"InAsP/AlGaInP/GaAs QD laser operating at ∼770nm"*, J. Phys. Conf. Ser., vol. 740, 012008, 2016

[8] R. Thomas, *"Monolithic coupled-cavity laser diodes for bio-sensing applications"*, PhD Thesis, Cardiff University, 2012

[9] P.M. Smowton, S.N. Elliott, S. Shutts, M.S. Al-Ghamdi and A.B. Krysa, *"Temperature-Dependent Threshold Current in InP Quantum-Dot Lasers"*, IEEE Journ. Select. Top. Quant. Electron., vol. 17, no. 5, pp. 1343-1348, 2011

[10] P. Blood, G.M. Lewis, H. Summer, J. Thomson and J. Lutti, *"Characterization of Semiconductor Laser Gain Media by the Segmented Contact Method"*, IEEE Journ. of Sel. Topics in Quant. Elect., vol. 9, no. 5, pp. 1275-1282, 2003

[11] G.M. Lewis, *"Study of Spontaneous Emission and Gain from Strained $(Al_yGa_{1-y})_xIn_{1-x}P$ Quantum Well Laser Diodes"*, PhD Thesis, Cardiff University, 2003

[12] M.S. Al-Ghamdi, P.M. Smowton, S. Shutts and P.Blood, *"Barrier Width and Growth Temperature Effect in InP/AlGaInP Quantum Dot Lasers"*, IEEE LEOS Ann. Meet. Conf. Proceed., pp.741-742, 2009

[13] P. Blood, *Quantum Confined Laser Devices*, Oxford University Press, Oxford, 1st Edition, 2015

[14] P.M. Smowton, A. George, I.C. Sandall, M. Hopkinson and H. Liu, *"Origin of Temperature-Dependent Threshold Current in p-Doped and Undoped In(Ga)As Quantum Dot Lasers"*, IEEE Journ. Sel. Top. in Quant. Electron., vol. 14, no. 4, pp. 1162-1170, 2008

[15] T. Higashi, T. Yamamoto, S. Ogita, *"Experimental Analysis of Characteristic Temperature in Quantum-Well Semiconductor Lasers"*, IEEE Jour. Sel. Top. Quant. Electron., vol. 3, no. 2, pp. 513-512, 1997

[16] L.A. Coldren and S.W. Corzine, *Diode Lasers and Photonic Integrated Circuits*, Wiley, New York, 1st Edition, 1995

[17] P.M. Smowton and P. Blood *"GaInP-(Al_yGa_{1-y})InP 670 nm Quantum-Well Lasers for High-Temperature Operation"*, IEEE Journ. of Quant. Elect., vol. 31, no. 12, pp. 2159-2164, 1995

[18] I. Karomi, P.M. Smowton, S. Shutts, A. B. Krysa and R. Beanland, *"InAsP quantum dot lasers grown by MOVPE"*, Opt. Expr., vol. 23, no. 21, pp. 27282-27291, 2015

[19] M.S. Al-Ghamdi, P.M. Smowton, P. Blood, *"Dot Density Effect by Quantity of Deposited Material in InP/AlGaInP Structures"*, IEEE Photon. Tech. Lett., vol. 23, no. 16, pp. 1169-1171, 2011

[20] P.M. Smowton, M.S. Al-Ghamdi, S. Shutts, G. Edwards, M. Hutchings and A.B. Krysa, *"Effect of Growth Temperature on InP QD lasers"*, IEEE. Photon. Tech. Lett., vol. 22, no. 2, pp. 88-90, 2010

[21] C.L Walker, I.C. Sandall, P.M. Smowton, I.R Sellers, D.J. Mowbray, H.Y Lius and M. Hopkinson, *"The Role of High Growth Temperature GaAs Spacer Layers in 1.3-μm In(Ga)As Quantum-Dot Lasers"*, IEEE Photon. Tech. Lett., vol. 17, no. 10, pp. 2011-2013, 2005

[22] J. Kim, C. Meuer, D. Bimberg and G. Eisenstein, *"Effect of Inhomogeneous Broadening on Gain and Phase Recovery of Quantum-Dot Semiconductor Optical Amplifiers"*, IEEE Journ. Quant. Electron., vol. 46, iss. 11, pp. 1670-1680, 2010

[23] V.M. Ustinov, A.E. Zhukov, A.Y. Egorov and N.A. Maleev, *"Quantum Dot Lasers"*, Oxford University Press, Oxford, 1st Edition , 2003

[24] A.E. Zhukov, A.R. Kovsh, V.M. Ustinov, A.Y. Egorov, N.N. Ledentsov, A.F. Tsatsul'nikov, M.V. Maximov, Y.M. Shernyakov, V.I. Kopchatov, A.V. Lunev, P.S. Kop'ev, D. Bimberg and Z.I. Alferov, *"Gain characteristics of quantum dot injection lasers"*, Semicond. Sci. Technol., vol. 14, pp.118-123, 1999

[25] P.M. Smowton, H.D. Summers, P. Rees and P. Blood, *"Optimisation of 670 nm strained-quantum-well laser diodes for high-temperature operation"*, IEE Proceed.- Optoelectron., vol. 141, no. 2, pp. 136-140, 1994

[26] R. Debusmann, T.W. Schlereth, S. Gerhard, W. Kaiser, S. Höfling and A. Forchel, *"Gain Studies on Quantum-Dot Lasers With Temperature-Stable Emission Wavelength"*, IEEE Journ. Quant. Electron., vol. 44, no. 2, pp. 175-181, 2008

[27] M. Uyuklu, M. Canpolat, H.J. Meiselman and O.K. Baskurt, *"Wavelength selection in measuring red blood cell aggregation based on light transmittance"*, Journ. Biomed. Optics, vol. 16, no. 11, pp. 117006, 2011

[28] L.A. Sordillo, Y. Pu, S.O Pratavieira, Y, Budansky and R.R. Alfano, *"Deep optical imaging of tissue using the second and third near-infrared spectral windows"*, Journ. of Biomed. Optics, vol. 9, no. 5, pp. 056004-1-6, 2014

Chapter 5

The Effect of Etched and Angled Facets on Device Performance

5.1 Introduction

Due to the difficulties and disadvantages of 'pick and place' fabrication techniques [1] [2] [3], lasers with cleaved facets are hard to achieve in complex monolithically integrated devices, like that proposed in section 3.2. The fabrication process described in figure 3.15 provides facet verticality akin to that obtained by cleaving and allows for a wider range of device design and integration of components. However, in this particular fabrication process the inherent pattern transfer from lithography masks and facet effects contribute to a roughening of the semiconductor surface of the facet [4]. Modelling has shown that this roughness causes a decrease in the reflectivity compared to that of a perfectly smooth facet [5]. This can be proven experimentally by comparing either the threshold current density [6] or the external differential efficiency [7] of lasers with etched facets to those with at least one cleaved facet.

As explained in section 2.6.1, the magnitude of coupling between sections of a coupled-cavity laser is determined by both the reflection/transmission coefficients of each cavity and the gap length between them. If the gap length is fixed, due to design and/or fabrication constraints, the only feasible way of increasing coupling is through minimisation of reflection coefficients, and therefore reflectivity, of the laser facets. For applications such as superluminescent diodes (SLEDs), low facet reflectivities can be achieved by an antireflection coating on the facet [8]. In-

stead, the focus has moved to incorporating angled facets into SLEDs [9] and amplifiers [10] to achieve this.

This chapter presents the characterisation of etched laser facets, using the relationship between facet reflectivity, R, and threshold gain to quantify a facet efficiency, η_f. Here, it is defined as

$$\eta_f = \frac{R_{etched}}{R_{cleaved}} \tag{5.1}$$

This has been achieved by investigating the performance of oxide-isolated stripe lasers with two cleaved (CC) facets and with one facet cleaved and one etched (CE), all being perpendicular to the oxide stripe. Their threshold current density, J_{th}, is compared to the net modal gain data of the same material. This has been previously measured using the segmented contact method described in section 4.2.2.2. Results from the first part of this chapter have then been applied to devices with an etched-angled facet (the front facet in this case is cleaved) to quantify the effect of facet angle on facet reflectivity and device performance. Experimental reflectivities have been compared to theoretical values, calculated using a reflection loss equation, and the difference between these and the experimental data presented in this chapter has been investigated.

5.2 Efficiency of Etched Facets

5.2.1 Experimental Procedure

From equation 2.23 the threshold current, I_{th} of a laser can be defined as the point at which sufficient optical gain is provided to equal all of the cavity losses. Above this point, a small increase in injected current causes lasing action, seen as a sharp increase in the light output of the laser. This abrupt change in light output is measured to calculate a laser's J_{th}.

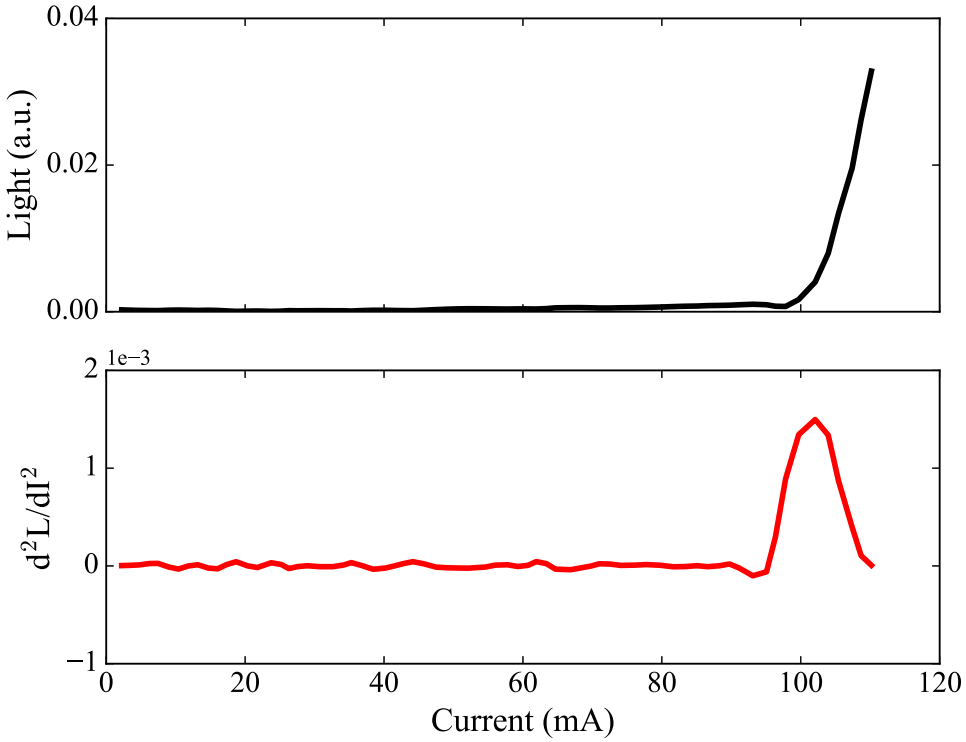

Figure 5.1: A light-current curve of a device (black line) and its calculated second differential (red line). The threshold current (or current density) of the laser can then be extracted as the x-coordinate at the peak of the second differential. This method of measuring the lasing threshold has been used throughout this work.

The light - current (L-I) characteristics (see figure 5.1) of the CC and CE lasers have been measured using the experimental set up originally assembled by K. Griffiths [11]. A device mounted on a transistor header is placed under a broad area silicon photo-detector (reverse biased at -10V). A pulse generator is used to apply a current to the device via a computer controlled current source. The resulting light, current and voltage are all measured at a boxcar integrator that provides a gated measurement triggered by the pulse generator. The measured values are recorded by a computer which increments the current supplied to the device from the pulse generator and the measure-

ments are all repeated. This measurement loop is repeated until the light measurement reaches a preset limit.

The maximum of the second order derivative, or

$$\frac{d}{dI}\frac{d^2L}{dI^2} = 0 \tag{5.2}$$

of the L-I curve has been used throughout this work to extract values of I_{th} (and/or J_{th}) [12]. Figure 5.1 gives an example of how values are extracted. The black line is an example of a L-I curve and the red line is the calculated second differential of the L-I. I_{th} is then extracted as the x-coordinate at the peak of the red line.

5.2.2 Laser Measurements

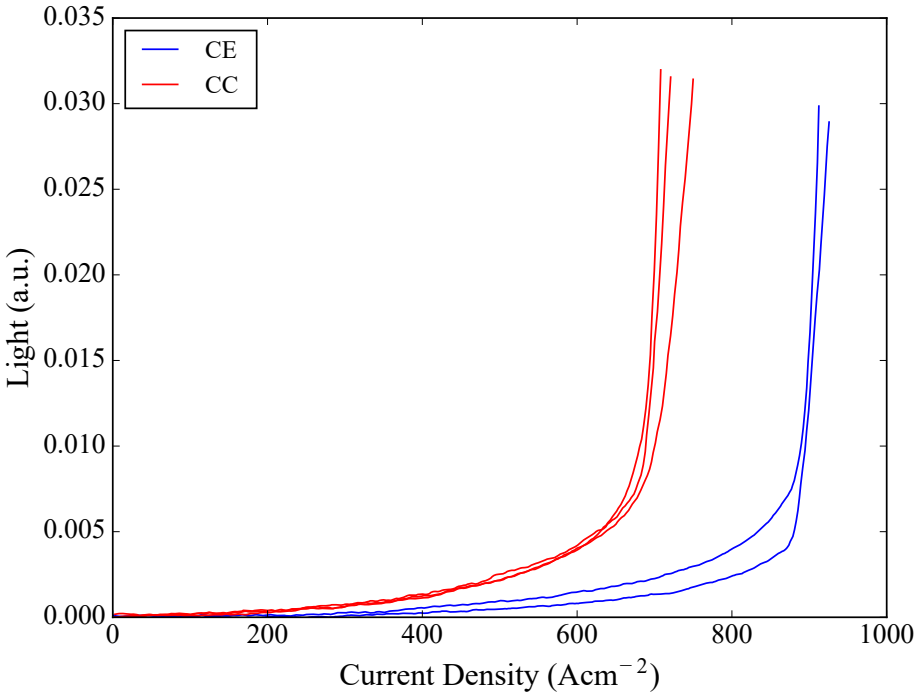

Figure 5.2: The comparison of light-current density curves for oxide-isolated stripe lasers with cleaved facets (red) and one cleaved and one etched facet (blue).

The CC and CE devices have been processed from two different samples, both of which originated from the same wafer. The light - current density (L-J) curves (measured from the cleaved facet in the C-E case) for these devices are presented in figure 5.2. J_{th} for the CE devices is approximately

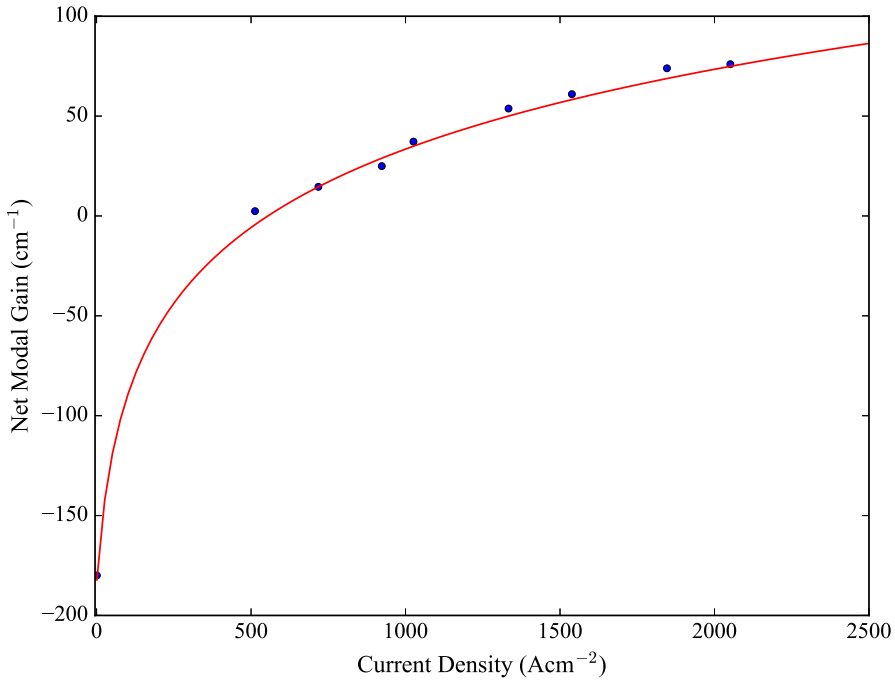

Figure 5.3: Peak net modal gain as a function of current density (blue points) fitted with a three parameter curve fit (red line). The fit equation used is of the form $y = a\ln[(x+b)/(c+b)]$ where the parameters from the fit are a = 58.7, b = 25.0 and c = 532.9.

29% higher than that of the CC reference devices. In order to calculate an etched facet reflectivity, the modal gain spectrum must be known. The net modal gain of this QW material was measured in section 4.5 and for comparison purposes it is necessary to plot the peak net modal gain values from figure 4.19 as a function of current density. This is plotted in figure 5.3.

Assuming $R_{cleaved}$ is 0.28, the logarithmic fit in figure 5.3 and equation 2.23 allow the determination of R_{etched}. This results in a mean value for R_{etched} of 0.104 with a standard deviation of 0.004. Therefore, the corresponding etched facet efficiency for the particular AlGaInP/GaInP MQW material and fabrication processes used, is η_f = 0.37 $\pm$ 0.04.

5.3 Angled Facet Devices

It was mentioned in the introduction of this chapter that angled facets are a technique employed to reduce facet reflectivity. Previous characterisation of angled facets include devices where waveguides are rotated with respect to the cleaving plane [13], facets etched to emit in-plane and perpendicular to the edge of the chip [14], and facet angle incorporated as the final fabrication step [9]. Adjusting the pattern of the EBL design in step 1, section 3.4.1.2(b) allows for more control over the range of achievable facet angles and at a point in the process flow which would otherwise not be achievable in the fabrication of the final device. Therefore, the etched-angled facets in this work are all achieved by this method for comparison purposes.

5.3.1 Facet Roughness

Although η_f has been found in the previous section, this currently only applies to etched facets of 0^o, where propagating light is at normal incidence to the facet. If angled facets are to be used in the integrated coupled-cavity device, the effect of etching off axis to the (001) plane must be investigated to allow for correct reflectivities to be used in future analysis of etched-angled devices in section 5.3.

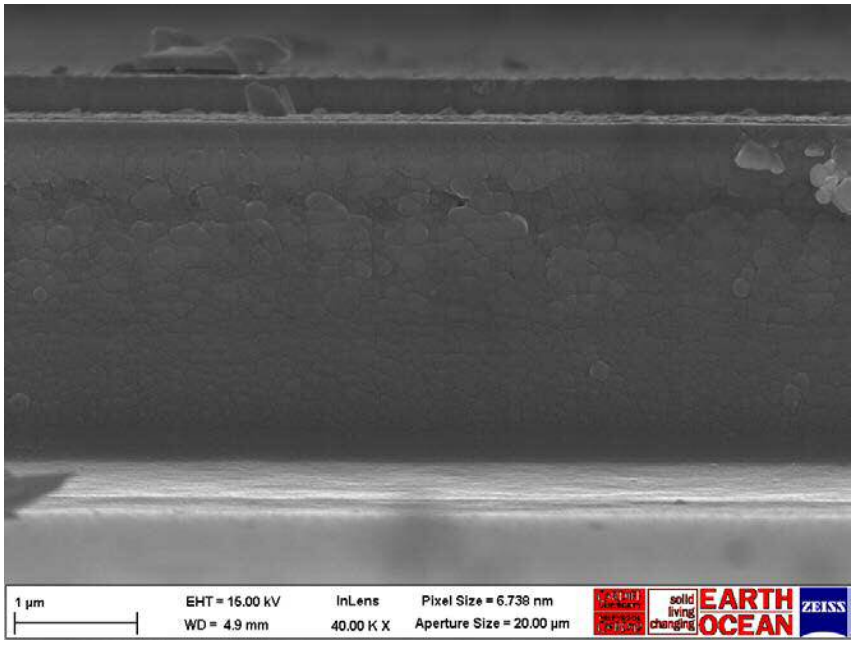

Figure 5.4: SEM image of an etched 0^o laser diode facet that shows variation in grain size of the PdAu coating deposited for better imaging results. The differences in grain size can be attributed to different layers in the material structure and an increase in roughness (either due to layer composition and/or residue on the facet) with increased grain size.

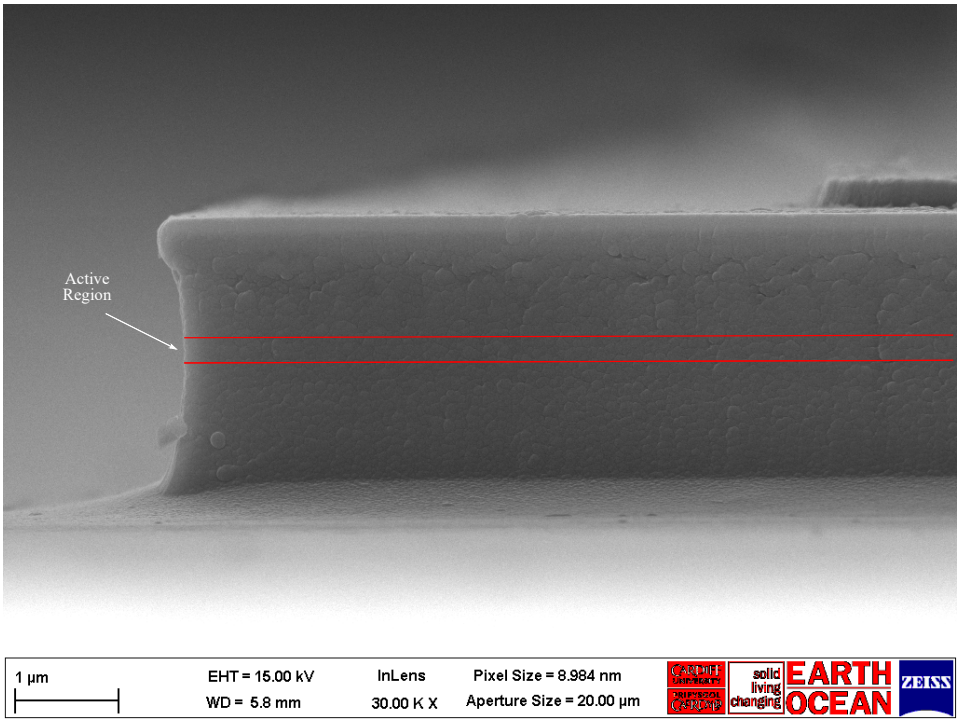

Figure 5.5: SEM image [i]of the etch profile of AlGaInP/GaInP QW material in a Ar/Cl_2 36/4 sccm dry ICP etch showing the concave like sidewall. It is assumed that the front surface also has this shape.

Figure 5.4 shows a scanning electron microscope (SEM) image of a 0^o facet formed by the dry etching technique in steps 1 to 3 of section 3.4.1.2(b). Visible on top of the etched facet is the thin layer of SiO_2 and the thicker p-contact. The sample was coated in a 20 nm thick coating of palladium-gold (Pd-Au) to reduce charging effects whilst imaging. The facet in figure 5.4 shows a visible difference in grain size of the coating. This can be attributed to different epitaxial layers in the material structure and a potential increase in roughness at certain points down the height of the facet. On comparison to the supplied epitaxial structure, the positioning of the darker band and larger grains corresponds to the high percentage of aluminium in the first AlGaInP p-cladding layer. It is suspected that the in-volatile products, $InCl_3$ and aluminium oxides, produced during the etching of AlGaInP using Cl_2/Ar chemistry (step 3, section 3.4.1.2), have a self-masking effect causing a roughening of the surface [15]. The etch was performed at an elevated temperature of 180^oC to assist with the removal of $InCl_3$ [16]. However, the simplified etch chemistry of a Cl_2/Ar etch that has been used to potentially reduce the sensitivity to etch conditions [17], means the self-masking effects are more prominent because of the high aluminium fraction in this particular

[i]Acknowledgements to Dr Duncan Muir in School of Earth & Ocean Sciences at Cardiff University for the use of the SEM and resulting images.

epitaxial structure. To prevent the oxidation of Al, BCl_3 would ideally be used here to eliminate O_2 [15]. Once past this first AlGaInP layer, the grains decrease in size down the vertical height of the facet. This could be due to the increased rate in removal of the aluminium oxides as the etch progresses. This effect could also be enhanced by re-deposited material from the etch mask and pattern transfer from the EBL.

Another feature apparent with this etch recipe is the slight concave sidewall in figure 5.5. It is assumed that the front facet also has this profile. This could indicate that the Cl_2/Ar gas ratios or RIE/ICP powers are not suitable for this epitaxial structure. Since the active region is at a depth where the profile is at its flattest and that etch optimisation is not a part of this work, the etch recipe described in step 3 section 3.4.1.2 is deemed adequate.

Gwyddion v.2.51 software has been used as an indirect method to qualitatively analyse and compare the surface roughness of different etched-angled facets using SEM images [18]. Before analysis, imported SEM images were scaled to ensure the x and y dimensions in the image plane are correct on the actual length scale. Using a profile thickness of 3 pixels with linear interpolation for each image, the root mean square deviation (R_{ms}) was found for each sample. On the 0^o sample, there is approximately a 50% increase between the measured R_{ms} of the GaAs cap and Al containing p-cladding layer. This is consistent along the horizontal width of the facet, with the R_{ms} measured close to both sidewalls of the mesa. Further down the facet, close to the active region, the average R_{ms} decreases, around a 30% difference to the cap.

On comparison to facets with different angles (1.7^o, 3.3^o, 12.3^o and 14.1^o laser facets were imaged) there is no evidence to suggest that the etching process causes more or less roughness to the laser facet when etching off axis to the crystal plane and therefore, it can be assumed that η_f found in section 5.2.2 for 0^o facets is also valid for etched-angled facet QW oxide-isolated stripe lasers using the etch process.

5.3.2 Facet Reflectivity

The power - current density (P-J) characteristics of the devices described at the start of section 5.3 have been measured using the set up in figure 5.6. The set up is identical to that in section 5.2.2

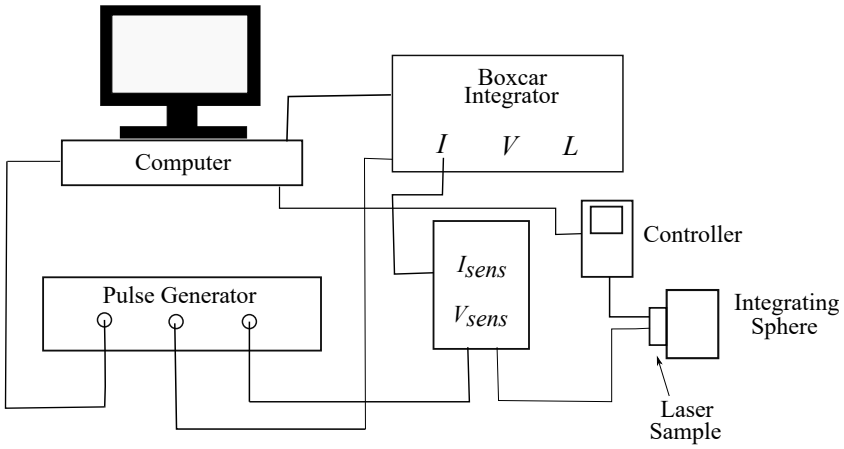

Figure 5.6: Diagram of experimental setup to measure the power output of a laser device using an integrating sphere.

with the detector replaced with an integrating sphere and power meter. The integrating sphere used here has a Si detector and two spheres. The device is mounted on a transistor header and placed inside the first sphere. This sphere is a hollow sphere with a white PTFE reflective coating that is polarisation insensitive. Light passes into the second sphere after multiple reflections, where it then falls incident on the detector. The power meter reads the output of the detector and sends a background corrected readout to the computer. A pulse generator is used as the current source, which is controlled by the computer. For these measurements, a 1000 ns pulse width at a rate of 0.6 kHz was used. This process is repeated for each current density and is recorded by the computer until the preset limit is reached. The power and current are then collected by the boxcar which provides a gated measurement and is then recorded by the computer. The mode width and device length were measured, as in section 4.4.1, to use in the calculation to convert current to current density. P-J curves as a function of facet angle are shown in figure 5.7. With the known relationship between threshold gain and facet reflectivity, it is unsurprising to see that threshold current density increases with facet angle. Facets with etched angles of 1.7^o have a threshold current density around 1100 Acm^{-2}. An increase in angle to 3.3^o and 5.0^o produces a current density increase of 200 Acm^{-2} and 500 Acm^{-2} respectively. There is a large increase in the threshold current density of the 14.1^o device to beyond 3000 Acm^{-2} indicating a very high threshold gain requirement. Figure 5.3 is once again used along with the threshold gain equation in equation 2.23 to extract effective facet reflectivity, R_{eff}. This must be corrected to extract the

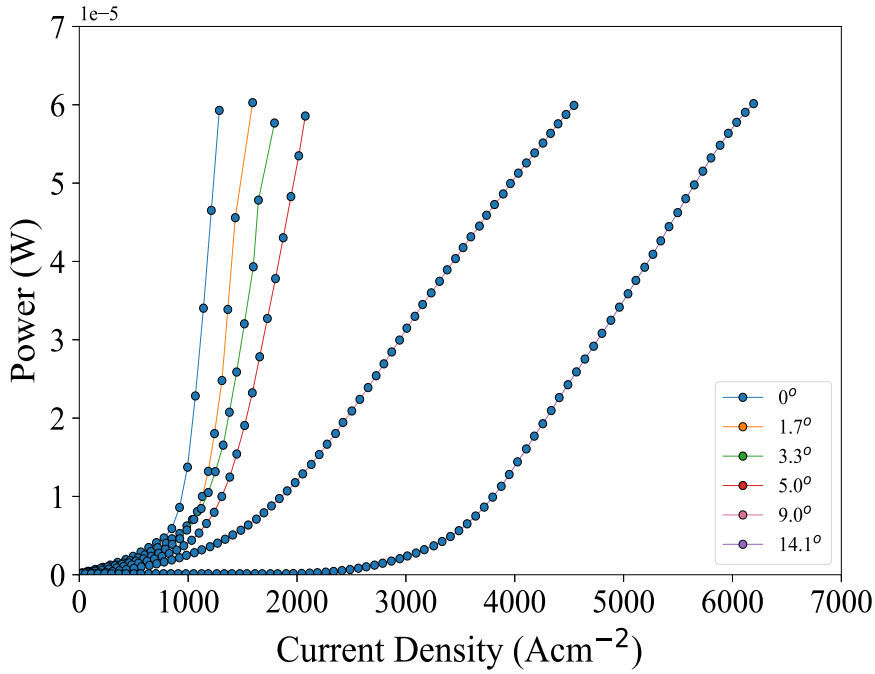

Figure 5.7: Power-current curves of CE QW devices with different rear etched facet angles of 0^o, 1.7^o, 3.3^o, 5.0^o, 9.0^o and 14.1^o. The power output of each device was measured with a 0.06% duty cycle using an integrating sphere.

actual etched-angled facet reflectivity, R_{angle}, by the relationship

$$R_{angle} = \frac{R_{eff}}{\eta_f} \tag{5.3}$$

Using this relationship and η_f = 0.37 found in section 5.2.2, the corrected facet reflectivities are plotted as a function of facet angle in figure 5.8. Reflectivities of 1x10^{-3} are obtained with facet angles as small as 1.7^o with values decreasing to 4.4x10^{-4}, 3.9x10^{-5} and 1.2x10^{-5} with an increase in facet angle. A very low reflectivity of 4.9x10^{-9} is achieved with a facet angle of 14.1^o. The critical angle is calculated as 17.8^o for this expitaxial structure and air interface. These results will be compared to theoretical calculations in section 5.3.2.2.

5.3.2.1 Theoretical Calculation

The theoretical calculation of facet reflectivity is not so trivial. The model in [19], describes the case of finding the reflection coefficient of the guided mode that turns back on itself to be equivalent to the case of transmission from the lasing waveguide into a slab waveguide of tilt angle 2θ (figure 5.9). In ideal conditions, i.e. if the two modes were perfectly aligned, the transmission

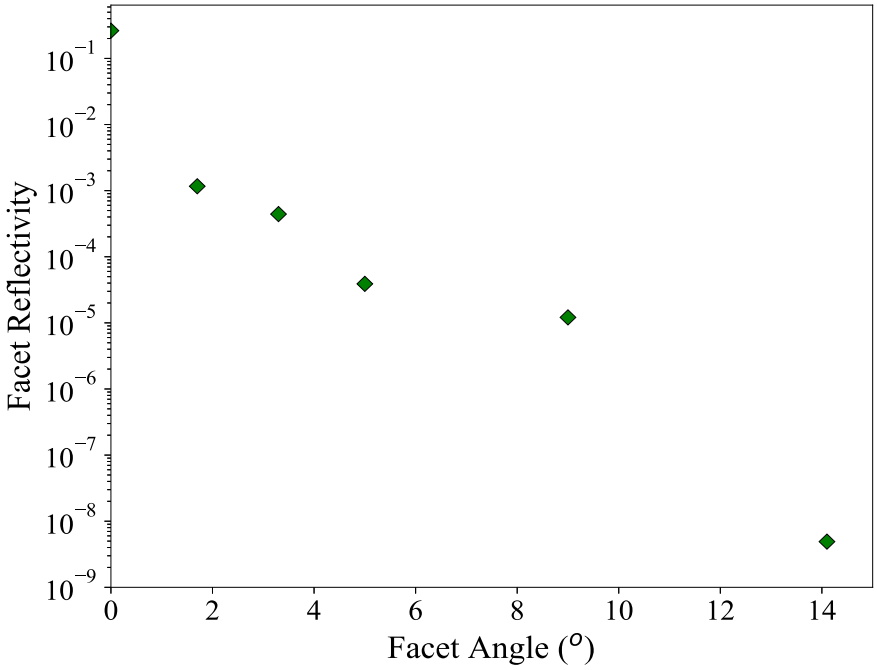

Figure 5.8: Calculated facet reflectivities from experimental data in figures 5.7 and 5.3 as a function of etched facet angle of QW devices.

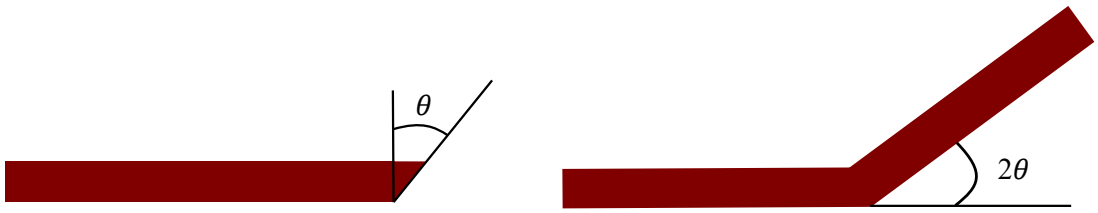

Figure 5.9: Equivalent model for the calculation of the facet reflectivity.(a) An angled facet waveguide of angle, θ and the equivalent situation for calculation purposes in (b) with two waveguides coupled at an angle 2θ.

coefficient would be 1. However, in non-ideal conditions the misalignment causes a loss equal to $\delta\phi = (\beta x).(2\tan\theta) \approx 2\beta\theta x$ [13], where β is the propagation constant of the guided TE mode and x is the transverse coordinate. The coupling coefficient of two waveguides is proportional to the correlation integral of the two electric fields, given by [20]

$$c \propto \int_{-\infty}^{\infty} |E_y|^2 \exp^{2i\beta\theta x} dx \tag{5.4}$$

where E_y is the y component of the fundamental TE mode of the waveguide. The reflectivity is then obtained from c

$$R = R_f(\theta)\,|c|^2 \tag{5.5}$$

where $R_f(\theta)$ is the Fresnel reflection coefficient of a plane wave that is reflected from an angled facet between semiconductor crystal and air. The condition in equation 2.24 in 2.3.1 applies to only normal incidence, i.e. where $\theta_i = \theta_t = 0^o$. However, for instances of non-normal incidence, which is the case when considering reflectivities of angled facets on a laser diode, Fresnel's reflection coefficient is of the form [21]

$$R_f(\theta) = \frac{\left(n_1 \cos\theta_i - \sqrt{n_2^2 - n_1^2 \sin^2\theta_i}\right)^2}{\left(n_1 \cos\theta_i + \sqrt{n_2^2 - n_1^2 \sin^2\theta_i}\right)^2} \tag{5.6}$$

where angle of incidence, θ_i, is equal to the facet angle and n_1 and n_2 are the refractive indices of the semiconductor crystal and air respectively.

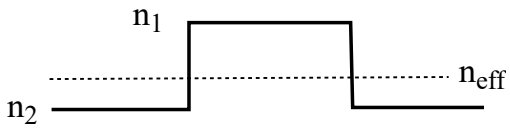

Figure 5.10: Slab model for the waveguide and the corresponding refractive indices, n_1, n_2 and n_{eff}.

Using the expressions for the fundamental mode inside and outside the waveguide [21],

$$E_y = A\cos(\kappa x) \qquad |x| \leq \mathrm{d} \tag{5.7}$$

$$E_y = A\cos(\kappa d)\exp^{-\gamma(|x|-d)} \qquad |x| > \mathrm{d} \tag{5.8}$$

where

$$\kappa^2 = n_1^2 k_0^2 - \beta^2 \tag{5.9}$$

$$\gamma^2 = \beta^2 - n_2^2 k_0^2 \tag{5.10}$$

with $k_0 = 2\pi/\lambda$ and $\beta = 2\pi n_{eff}/\lambda$, the correlation integral can be solved to obtain facet reflectivity as a function of facet angle. Equation 5.5 becomes [19]

$$R = R_f(\theta).\left[\frac{WU^2\{\left[W^2-(\beta\theta d)^2\right]\frac{\sin(2\beta\theta d)}{2\beta\theta d}+W\cos(2\beta\theta d)\}}{(1+W)\left[U^2-(\beta\theta d)^2\right]\left[W^2+(\beta\theta d)^2\right]}\right]^2 \tag{5.11}$$

where the parameters U and W, respectively, are the normalised transverse propagation constant

$$U = \kappa d \tag{5.12}$$

and the normalised transverse decay parameter

$$W = \gamma d \tag{5.13}$$

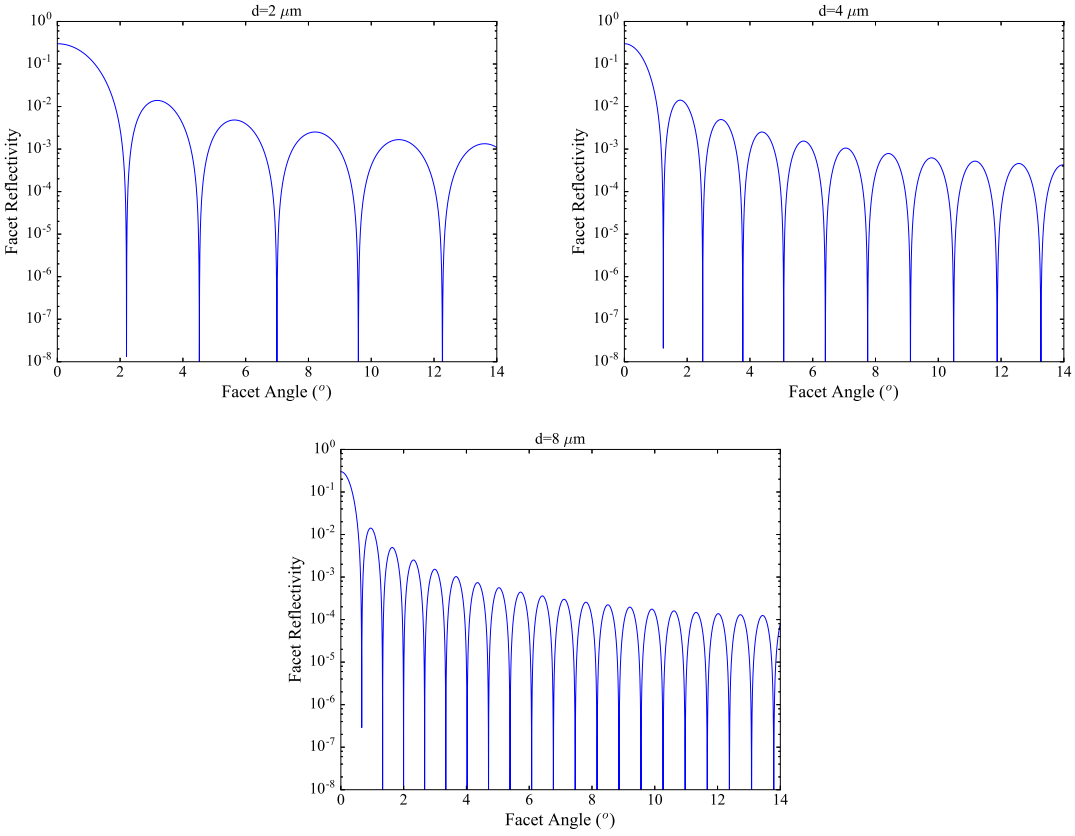

Figure 5.11: Facet reflectivity as a function of facet angle calculated using $n_1 = 3.4216$, $n_{eff} = 3.2646$ and $n_2 = 3.24774$ and for several values of the waveguide width (a) 2 μm, (b) 4 μm and (c) 8 μm operating at a wavelength of 651 nm.

Figure 5.11 shows examples computed for a hypothetical uncoated laser waveguide with n_1 =

3.4216, n_2 = 3.24774 and n_{eff} = 3.2646 operating at a wavelength of 651 nm, of widths, d = 2, 4 and 8 nm. It is also assumed here that $\eta_f = 1$, i.e. the facet is a perfectly smooth mirror. The reflectivity at a facet angle of 0^o is simply the Fresnel reflection loss of the field from the index step between semiconductor crystal and air at normal incidence and does not change in each instance of d. With an increase in facet angle, there is a rapid decrease in reflectivity. The dependence of the reflectivity in equation 5.11, on the waveguide width, is due to the decay parameter γ in equation 5.13 in the cladding material. The wider the waveguide, the faster the decline of facet reflectivity.

5.3.2.2 Comparison with Experimental Results

Equation 5.11 is used to calculate the reflection losses from an angled facet for the fundamental TE mode of a slab waveguide. The slab waveguide model can be used to describe the laser mode in a broad-area or ridge waveguide in the effective refractive index approximation. The results presented in this section are therefore, also an approximately valid. For large facet angles the evanescent field outside the waveguide core is poorly represented by the Gaussian approximation. Although the TE mode of the approximate effective index slab waveguide model corresponds to mixed TE and TM-like modes of a broad area waveguide, the reflection losses are expected to be more accurate that the Gaussian approximation. Using the TE mode of the slab in the loss calculations does not restrict its use, since it is the shape of the field distribution and the relative position of the phase fronts.

Calculating the reflection loss in equation 5.11 for the QW material used in this work allows for the comparison with reflectivities experimentally found in in section 5.3.2. In figure 5.12, the solid blue line has been calculated using the same n_1, n_2, n_{eff} and λ values as examples in figure 5.11. However, the peak amplitudes and frequency have changed due to the waveguide width being much larger than the examples in figure 5.11. Since the waveguide is much larger, the waveguide now supports multiple transverse modes. As before the reflectivity at 0^o is the Fresnel reflection loss of the field from the index step between semiconductor crystal and air at normal incidence. The amplitude change that would occur if the measurement error of the waveguide width (± 5 μm) has also been plotted in figure 5.12. The top and bottom red dashed lines correspond to the minimum and maximum waveguide widths respectively. Plotting experimental facet reflectivities

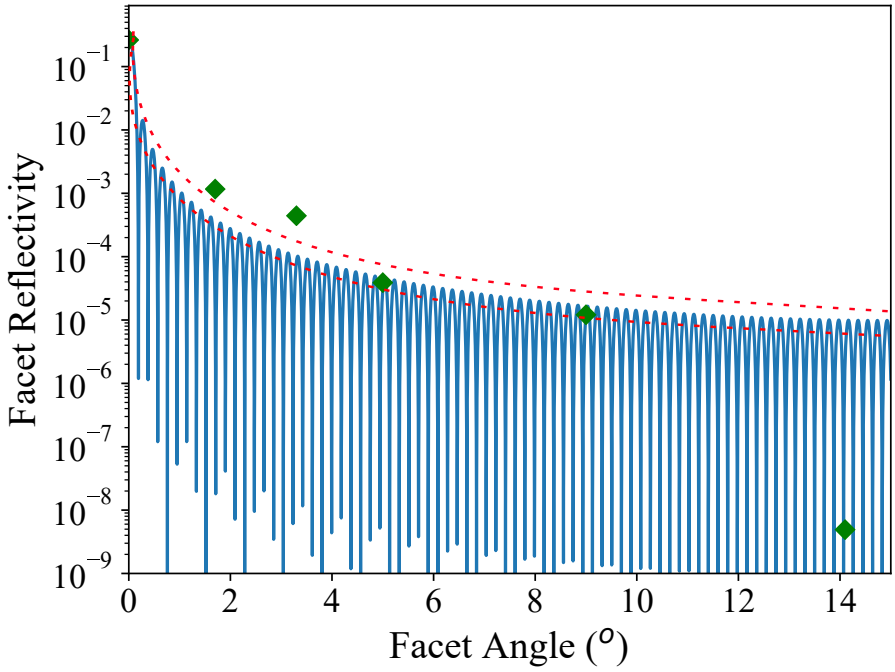

Figure 5.12: Comparison of facet reflectivity as a function of facet angle for experimental data, previously shown in figure 5.8 (green diamonds), with theoretical values (solid blue line). The theoretical values have been calculated using $n_1 = 3.4216$, $n_{eff} = 3.2646$ and $n_2 = 3.24774$ for a waveguide width of 30 μm operating at a wavelength of 651 nm. The red dashed lines indicate the region in which the amplitude of facet reflectivity may fall when incorporating the error associated with measuring the waveguide width by optical microscope.

in figure 5.12 shows that the measured data fits well to the calculated reflectivity. It is experimentally very hard to meet the exact angle of a specific dip due to fabrication tolerances and the exact mode structure not being known. Due to the approximation used to plot the theoretical data in figure 5.11, the waveguide may support more transverse modes than has been approximated here. Therefore, less severe dips in the reflectivity may be seen, so what is presented here is in effect the ideal case for a single mode device. The magnitude of the peaks in the data however, are still valid. The data points that sit on or above the top dashed red line may indicate a lower η_f than has been assumed or that the cleaved facet also has an efficiency associated with it due to imperfections from the cleaving process. Another possibility is resist or SiO_2 residue on the facet, left behind after fabrication. No evidence for this was seen in section 5.3.1. However, the lasers imaged were not the same as those used to collect data in figure 5.7, but were from the same sample. This is due to the destructive nature of the metal coating sputtered onto samples to avoid self charging effects during SEM measurements.

5.3.3 Differential Efficiency

A laser diode's ability to convert input electric to output light power, measured above threshold, is regarded as an important figure of merit of performance. A curve of optical power versus current is insightful in many ways but here, the focus is on extracting the external (η^d_{ext}) and internal (η^d_0) differential efficiencies as a function of facet angle.

η^d_{ext} is a measure of the number of photons per unit time emitted from the laser diode due to an increase in applied external current. From [22], η^d_{ext} is defined as

$$\eta^d_{ext} = \frac{2e}{h\nu}\frac{dP_{ext}}{dI} \tag{5.14}$$

with $\frac{dP_{ext}}{dI}$ equal to the slope of the curve of optical power per facet versus current and $h\nu$ the photon energy of the laser light. The factor of 2 is included in equation 5.14 to account for light emission from both facets, assuming both have the same reflectivity.

As seen in section 5.3.2, facet reflectivity changes quite dramatically with facet angle and therefore the front and back facet of these C-E laser diodes have different reflectivities. Equation 5.14 above only applies when both facets have the same reflectivities and so this equation must be modified to account for the asymmetry. Therefore the external differential efficiency of the front ($\eta^d_{ext,F}$) and back ($\eta^d_{ext,B}$) facet are [23]

$$\eta^d_{ext,F} = \frac{e}{h\nu}.\frac{dP_{total}}{dI}.\frac{(1-R_F)(1+R_B)}{(1-R_FR_B)} \tag{5.15}$$

$$\eta^d_{ext,B} = \frac{e}{h\nu}.\frac{dP_{total}}{dI}.\frac{(1+R_F)(1-R_B)}{(1-R_FR_B)} \tag{5.16}$$

where R_F and R_B are the reflectivities of the front and back facet respectively and $\frac{dP_{total}}{dI}$ is now equal to the slope of the curve of total optical power from the laser versus current.

Table 5.1 gives η^d_{ext} as a function of facet angle calculated from P-I curves in figure 5.7 and equations 5.15 and 5.16. α_i for this material has been measured previously in section 4.5 and the value at 300 K is α_i = 5.7 cm^{-1}. It is seen that η^d_{ext} decreases with an increase in facet angle. Etched facet lasers typically have lower average η^d_{ext} values reported than those for cleaved facet lasers [16]. However, there are no reports on how these parameters change when incorporating

Table 5.1: The calculated external differential quantum efficiencies from measured P-I curves of devices fabricated with one etched facet (back) at varying angles to normal incidence and the other, cleaved (front).

Facet Angle (^{o})	$\eta^d_{ext,F}$ (%)	$\eta^d_{ext,B}$ (%)
0	14.2	19.4
1.7	7.03	12.6
3.3	6.17	11.0
5.0	4.51	8.06
9.0	1.46	2.61
14.1	1.45	2.59

both types of facet into a laser diode. The non-radiative recombination of carriers can be increased in etched facet lasers due to electron traps introduced into the semiconductor crystal by plasma etching [24]. Alongside this, as the facet angle is increased, less photons travel back down the waveguide to contribute to the round trip amplification. With the misorientation, most of the light from the facet will not re-couple back into the waveguide [9]. It is also worth noting that the $\eta^d_{ext,B}$ values are higher than those for $\eta^d_{ext,F}$. This is expected due to this facet having a lower reflectivity (and therefore higher transmission) caused either by plasma etching or a combination of etching and facet angle.

5.4 Summary

This chapter has presented the characterisation and performance of etched facet AlGaInP/GaInP QW lasers. The L-I characteristics of laser with two cleaved facets (CC) and with one cleaved and one etched (CE) have been measured to calculate and plot light - current density for these devices. A logarithmic function has been fitted to the peak net modal gain data of this epitaxial structure using a segmented contact device, previously measured in section 4.5. This has been used to calculate the threshold gain corresponding to each of the CE laser threshold current densities. Using equation 2.23 to relate threshold gain to facet reflectivity gives a mean value for etched facet efficiency, η_f, of 0.37 ± 0.04.

Using SEM images, it is possible to surmise that changing the facet angle of an etched facet

laser does not change the facet efficiency, i.e. η_f is constant. By measuring P-I characteristics of angled facet CE laser, threshold current density increases with facet angle. It is possible to use the same method mentioned above to calculate facet reflectivity as a function of facet angle. A very low reflectivity of $4.9\text{x}10^{-9}$ is measured for a laser with a 14.1^o etched facet. Comparison to theoretical values of the device angles show close agreement. P-I characteristics are also used to investigate the external quantum efficiency as a function of facet angle. Increasing facet angle has a detrimental effect on this efficiency, where the external quantum efficiency of an etched facet decreases approximately 87% when facet angle is increased from 0^o to 14.1^o.

References

[1] B. Corbett, R. Loi, W. Zhou, D. Liu and Z. Ma, *"Transfer print techniques for heterogeneous integration of photonic components"*, Prog. Quant. Electron., vol. 52, pp. 1-17, 2017

[2] S.W. Kettlitz, S. Valouch, W. Sittel and U. Lemmer, *"Flexible planar microfluidic chip employing a light emitting diode and a PIN-photodiode for portable flow cytometers"*, Lab Chip, vol. 12, no. 1, pp. 197-203, 2012

[3] X.J. Liang, A.Q. Liu, C.S. Li,, T.C. Ayi and P.H. Yap, *"Determining refractive index of single living cell using an integrated microchip"*, Sens. Actuat. A, vol. 133, no. 2, pp. 349-354, 2007

[4] D.A. Francis, C.J. Chang-Hasnain and K. Eason, *"Effect of facet roughness on etched-facet semiconductor laser diodes"*, Appl. Phys. Lett., vol. 68, no. 12, pp. 1598-1600, March 1996

[5] D.A. Stocker, E.F. Schubert, W. Grieschaber, K.S. Boutros and J.M. Redwing, *"Facet roughness analysis for InGaN/GaN lasers with cleaved facets"*, Appl. Phys. Lett., vol. 73, no. 14, pp. 1925-1927, Oct 1998

[6] L.A. Coldren, B.I. Miller and J.A. Rentschler, *"Etched Mirror and Groove-Coupled GaInAsP/InP Laser Devices for Integrated Optics"*, IEEE J. Quantum Electron., vol. QE-18, pp. 1679-1687, Oct. 1982

[7] J.L. Merz and R.A. Logan, *"GaAs double heterostructure lasers fabricated by wet chemical etching"*, Joun. Appl. Phys., vol. 47, no. 8, pp. 3503-3509, Aug 1976

[8] I.P. Kaminow, G. Eisenstein, L.W. Stulz and A.G. Dentai, *"Lateral confinement InGaAsP superluminescent diode at 1.3 μm"*, IEEE J. Quantum Electron., vol. QE-19, no. 1, pp. 78-82, 1983

[9] Z.Y. Zhang, I.J. Luxmoore, C.Y. Jin, H.Y. Liu, Q. Jiang, K.M. Groom, D.T. Childs, M. Hopkinson, A.G. Cullis and R.A. Hogg, *"Effect of facet angle on effective facet reflectivity and operating characteristics of quantum dot edge emitting lasers and superluminescent light-emitting diodes"*, Appl. Phys. Lett., vol. 91, pp. 081112-(1-3), 2007

[10] Z. Wang, B. Mikkelson, B. Pederson, K.E. Stubkjaer and D.S. Olesen, *"Coupling between angled-facet amplifiers and tapered lens-ended fibers"*, J. Light. Technol., vol. 9, no. 1, pp. 49-55, 1991

[11] K. Griffiths, *"Automated Laser Diode Measurements"*, MPhil Thesis, UWCC, 1992

[12] C.Z. Ning, *"What is Laser Threshold?"*, IEEE Journ. Select. Topic. Quant. Electron., vol. 19, no. 4, (Invited Paper), 2013

[13] M. Mundbrod, *"Ridge-Waveguide Laser with Tilted Facets"*, Annual Report, Optoelectronics Dept., University of Ulm, pp. 1-6, 2003

[14] R. Santos, D. D'Agostino, F.M. Soares, H. Rabbani Haghighi, K.A. Williams and X.J.M. Leijtens, *"Fabrication of Etched Facets and Vertical Couplers in InP for Packaging and On-Wafer Test"*, IEEE Phot. Technol. Lett., vol. 28, no. 3, pp. 245-247, 2016

[15] Z. Hao, S. Han, F. Ren, B. Xiong, C. Sun and Y. Luo, *"Smooth and Vertical Etching of GaAs/GaInP/AlGaInP Using Iductively Coupled $Cl_2/BCl_3/CH_4$ Plasma"*, Jpn. Journ. Appl. Phys., vol. 43, no. 12, pp. 8304-8307, 2004

[16] G.T. Edwards, P.M. Smowton and D.I. Westwood, *"Dry Etching of Ansiotropic Microstructures for Distributed Bragg Reflectors in AlGaInP/GaAs Laser Structures"*, IEEE Journ. Select. Topic. Quant. Electron., vol. 14, no. 4, pp. 1098-1103, 2008

[17] S. Shutts, *"Monolithic Dual-Wavelength InP/AlGaInP Quantum Dot Lasers"*, PhD thesis, Cardiff University, 2012

[18] Ž. Pavlović, D. Risović and D. Novaković, *"Comparative study of direct and indirect image-based profilometry in characterization of surface roughness"*, Surf. Interface Anal., vol. 44, pp. 825-830, 2012

[19] D. Marcuse, *"Reflection loss of laser mode from tilted end mirror"*, Journ. of Lightwave Tech., vol. 7, no. 2, pp. 336-339, Feb 1989

[20] K.J. Ebeling, *"Integrated Optoelectronics"*, Springer-Verlag, Berlin, 1993

[21] D. Marcuse, *"Light Transmission Optics"*, Van Nostrand Reinhold, New York, 1982

[22] P.M. Smowton and P. Blood, *"The Differential Efficiency of Quantum-Well Lasers"*, IEEE Journ. Select. Topic. Quant. Electron., vol. 3, no. 2, pp. 491-498, April 1997

[23] C.J. Panchal, V.A. Kheraj, K.M. Patel, P.K. Patel, B.M. Arora, T.K. Sharma, *"Effect of facet reflectivities on high-power highly strained InGaAs quantum-well diode Lasers Operating at 1.2 μm"*, Proc. of SPIE Vol. 6028, 2005

[24] J.W. Lee, S.J. Pearton, C.R. Abernathy, W.S. Hobson and F. Ren, *"Damage introduction in InGaP by electron cyclotron resonance Ar plasmas"*, Appl. Phys. Lett., vol. 67, pp. 3129-3131, 1995

Chapter 6

Realisation of C-C Sensing

6.1 Introduction

Development of lab-on-chip systems has combined fluidic and optical guiding with components such as sensors and detectors, to create micrototal analysis systems (μTAS) for bio-sensing applications [1]. Integration of all components brings about a fully portable system for monitoring in point-of-care and resource-limited settings [2]. Consequently, chip based sensing using capillary fill microfluidics with monolithically integrated lasers and detectors, using a device as fabricated in section 3.6, demonstrates chip based particle sensing and the feasibility of true chip based photonic measurements.

Current optical sensors use various mechanisms including refractive index changes [3], absorption [4] and Raman scattering [5] for sensing. More advanced integrated systems involve the realisation of biological cell lasers using green fluorescent protein [6] and the incorporation of biological matter on the side walls of whispering gallery mode resonators [7], both as the lasing gain medium. These results indicate the feasibility of a coupled-cavity semiconductor laser, whereby cells, flowing through the open cavity, become an active element of the laser cavity and can influence the cavity losses of the laser. This has the potential to increase the sensitivity and resolution of detection events.

Gain models presented in [8] demonstrate how coupled-cavity modes can have lower threshold gain values than those formed in either of the individual laser sections of the coupled-cavity de-

vice. A perturbation of the gap loss, caused by a passing cell, could therefore be used to trigger a change in the device from it lasing as a coupled-cavity, to lasing as two individual lasers or not lasing at all. Etched, angled, internal facets, shown to affect facet reflectivity in the previous chapter, of the coupled-cavity, can be incorporated to increase discrimination. Evidence of the interaction between the cell and the lasing mode would be contained within the light (or photo-voltage) output measured from the device.

This chapter presents the results of an investigation into the nature of the coupling between laser sections of a coupled-cavity device for a proof of concept. Although coupled-cavity modes have been established in devices with gap lengths of the order of a few tens of microns, an aim of this investigation has been to consider whether coupled-cavity modes can be established in a device with 100 μm wide gap along with other considerable gap losses. In section 6.2, the coupling between the laser section of the device has been investigated by measuring the photo-voltage generated by one section from an optical input from another. The detection of 6 μm beads, due to their size likeness to a specific WBC type, is also presented. Following on from this, evidence for coupled-cavity modes is investigated using lasing spectra and gain requirement calculations. In section 6.5.2, with the incorporation of angled-etched facets, evidence of coupled-cavity modes is presented in the interpretation of the light-current characteristics.

6.2 Device Configuration

A coupled-cavity device, through electrical isolation of each section, can be operated as both a laser or detector. By forward biasing one section, the resulting light that is transmitted across the gap and coupled into the active region of the opposing section can be detected by measuring the photo-current generated in that section. Figure 6.1 shows the layout of the laser/detector array and microfluidic channel, with the oxide-isolated stripe in the centre of each etched mesa being 30 μm wide and 990 μm long, fabricated from the AlGaInP/GaInP quantum well (QW) structure in chapter 4. The addition of a third section, sections 2 and 6 in figure 6.1, have been included with the intention of on-chip proof of principle coupled-cavity (C-C) measurements. The etched facets in this figure are, in this work, labelled as 0^o facets. The numbers seen here correlate to specific numbering of the driver boards in the computer software for the control unit electronics, that the device is placed in, and this labelling will be used throughout the chapter. The experimental setup up will be described in the next section.

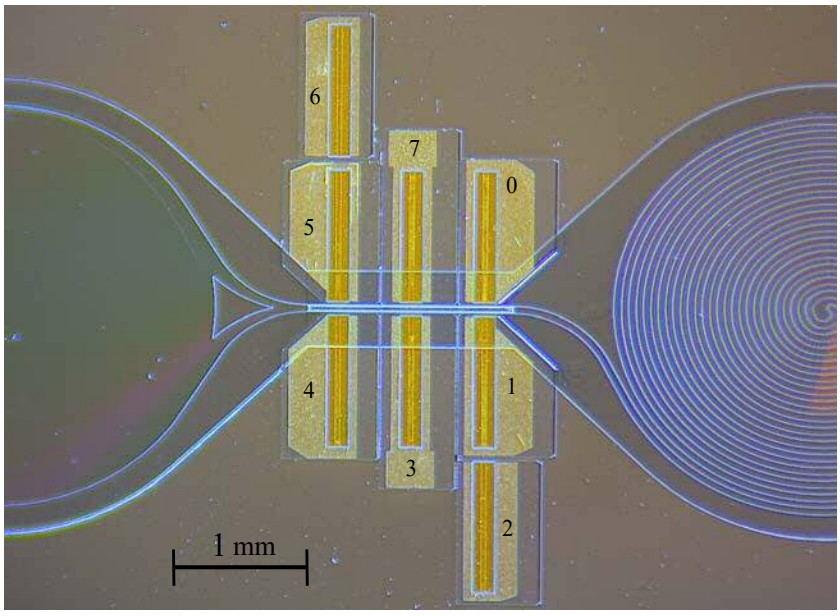

Figure 6.1: Integrated lasers and on-chip detectors with capillary fill microfluidics. This optical microscope image shows the an inlet reservoir on the left, the 3D microfluidic channel in the centre between the laser sections, and the spiral outlet on the right. On the first and third laser pair is an additional section, with the intention of being used as an on-chip coupled-cavity detector. The labelling of each section, with a number from 0 to 7, correlates to commands from the computer software to the electronics in the control unit and will be used to label results later in the chapter.

Chapter 5 detailed the effect of etched, angled facets on device performance, the main result indicating significant decreases in facet reflectivity with increasing facet angle. Here, we aim to

employ this technique to reduce the effective reflectivity of the gap facets. Figure 6.2 shows an optical microscope image of a fabricated device with etched, angled, internal facets, either side of the microfluidic channel. Each laser section can be seen to be offset to its opposing section across the channel. This is to correct for the now changed angle of transmitted light (compared to the standard Fabry-Pérot laser cavity in figure 6.1), and the refraction that occurs at each interface in the channel. Simple trigonometry and Fresnel's equation calculations are used to calculate this offset for a specific facet angle. A device with 22.6^o angled facet laser/detector pairs is used in this chapter, to ensure a large amount of coupling is achieved whilst still allowing lasing action in each section, and that this is achieved within the limits of the control unit electronics.

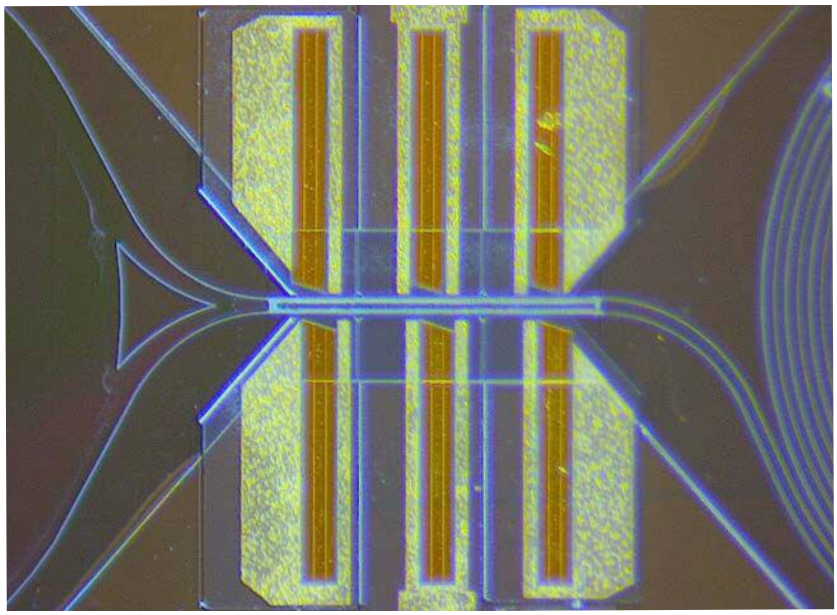

Figure 6.2: Optical microscope image of an array of laser/detector sections with etched, angled facets, either side of the microfluidic channel.

6.3 Experimental Operation of On-Chip Measurements

Figure 6.3 shows the components of the experimental set up used for all on-chip measurements in this chapter. The packaged device is plugged into a control unit [i] containing the electronic boards required to drive and sequence the lasers, that also amplify the recorded photo-voltage signals. The control unit is designed with a low profile so that it can be operated within the working distance of a microscope objective lens. This allows the passage of particles to be recorded independently of the chip based measurement using a high speed (HS) camera. The camera and microscope are

[i] Designed and built by Andrew Harrison

used to simply characterise the performance of the chip and are not a requirement of the final system. Each section can be electrically forward biased in sequence, so that while one section acts as

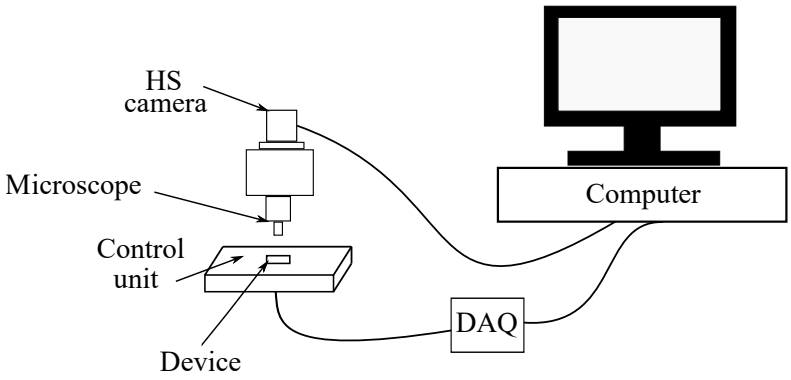

Figure 6.3: Schematic of the experimental setup used to measure both single laser characteristics and time resolved measurements.The high speed (HS) camera and microscope are used here to characterise the performance of the chip and are not required for the final system.

a laser, the others can be operated as photo-detectors. Each driver board can deliver a maximum forward-bias of 2A to each laser section. In this work, the laser sections of the device are operated in pulsed mode, to minimise self-heating effects, with a pulse length of 500 ns at a repetition rate of 10 kHz. Although the laser output intensity is very sensitive to temperature changes, no current induced self heating is observable at this duty cycle. Also, the power output of a single section is not high enough (< 60 μmW) to encourage a large heat dissipation, so the operating temperature of the device is considered to be constant. The resulting amplified photo-voltages are logged externally by a NI 6210 USB data acquisition unit (DAQ) and transferred to a computer for analysis. This setup allows a sequential operation of the lasers, effectively toggling back and forth between laser and detector on alternate pulses, creating a system where beam transit events can be captured from both sides of the channel in separate time-resolved measurements. It also allows for on-chip measurement of light-current curves for characterisation of each laser section.

The control unit, the device sits in, is designed with a low profile so that it can be operated within the working distance of a microscope objective lens. This allows, in a research setting, for the passage of particles to be monitored by eye or be recorded independently of the electronic measurement, for instance with a high speed camera.

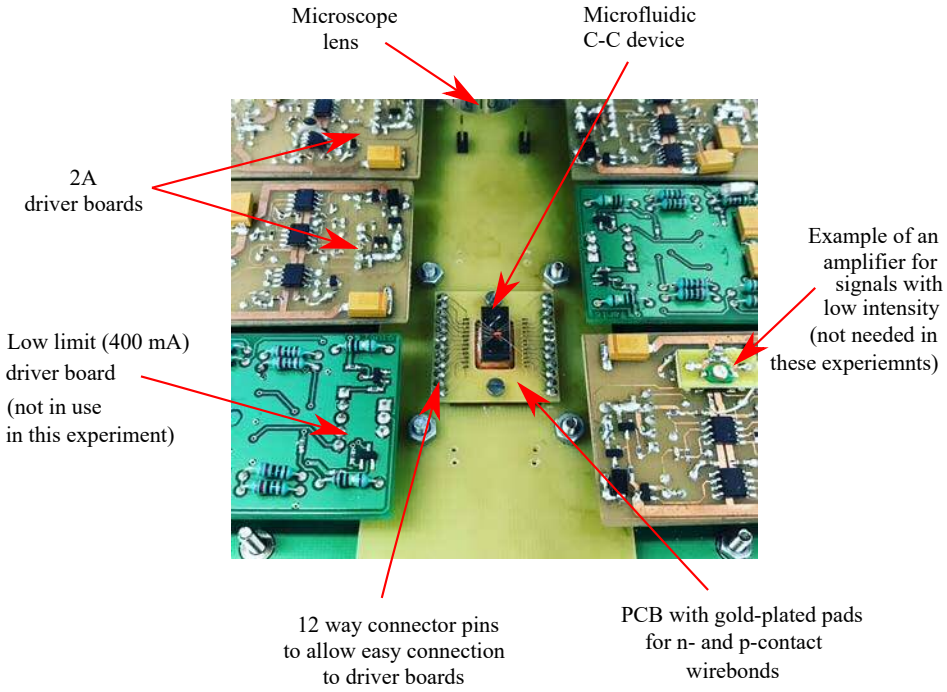

Figure 6.4: Image of inside the control unit, showing where the packaged device sits and the electronic driver boards for laser/detector sequencing. As described in the introduction the concept is that ultimately the control electronics would also be integrated on chip and the system could be monitored and/or controlled by a smart phone.

6.4 Laser-Photodetector Configuration

6.4.1 On-chip Light-Current Measurements

The control unit and computer software, in figure 6.3, allows on-chip light-current (L-I) measurements, by user selection of laser and detector sections and specifying the automated current step and limit. An example L-I curve, from a 0^o facet laser, is shown in figure 6.5 and obtained by measuring the photo-current, incident on the selected detector, at each current, until the preset current limit is reached.

In figure 6.5 there are three curves, all where section 1 is measured on 0, but with different current increments for each. The steps tested were 2 mA (blue solid line), 20 mA (black dashed line) and 50 mA (red dotted line). The sharp change in gradient associated with the transition from below threshold spontaneous emission to above threshold lasing is well defined in all three cases. The ability to measure such well defined L–I curves, demonstrates that light must be coupled across the gap from one section to the other. The 2 mA curve, shows a jagged line indicating the current

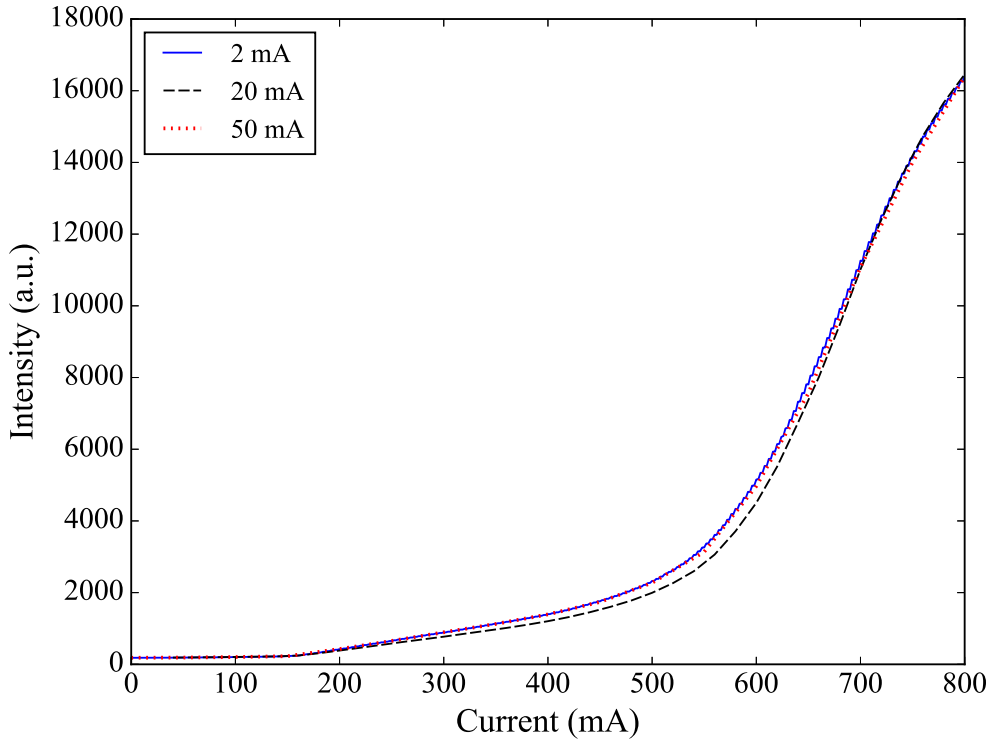

Figure 6.5: Example L-I curve of section 1 measured on-chip on section 0 (see figure 6.1). Different automated current steps; 2 mA (blue line), 20 mA (green line) and 50 mA (red line), provide similar shaped curves and have negligible differences in the apparent in threshold current.

step size is smaller than the resolution of the DAQ causing a digitisation error. On the other hand, increments of 50 mA provide data points that are too far apart, providing less detail around threshold. Using 20 mA increments provides sufficient points within a reasonable time-scale, but due to no change in threshold current between the three curves in figure 6.5, both 20 mA and 50 mA increments have been used in this work, depending on the current range required for that device.

To test whether fluid in the SU-8 microfluidic channel has any effect on the threshold current of a laser section and the coupling between two sections, the L-I characteristics of a forward biased laser section 'L' has been measured using the photo-current generated in the opposing detector section 'D', with and without isopropyl alcohol(IPA) in the channel.

The L–I curves that result from using the device in the laser/detector configuration with an empty and filled channel are presented in figure 6.6. The threshold current values and above threshold gradients of the L–I curves for each of the devices are very similar, indicating that the presence of

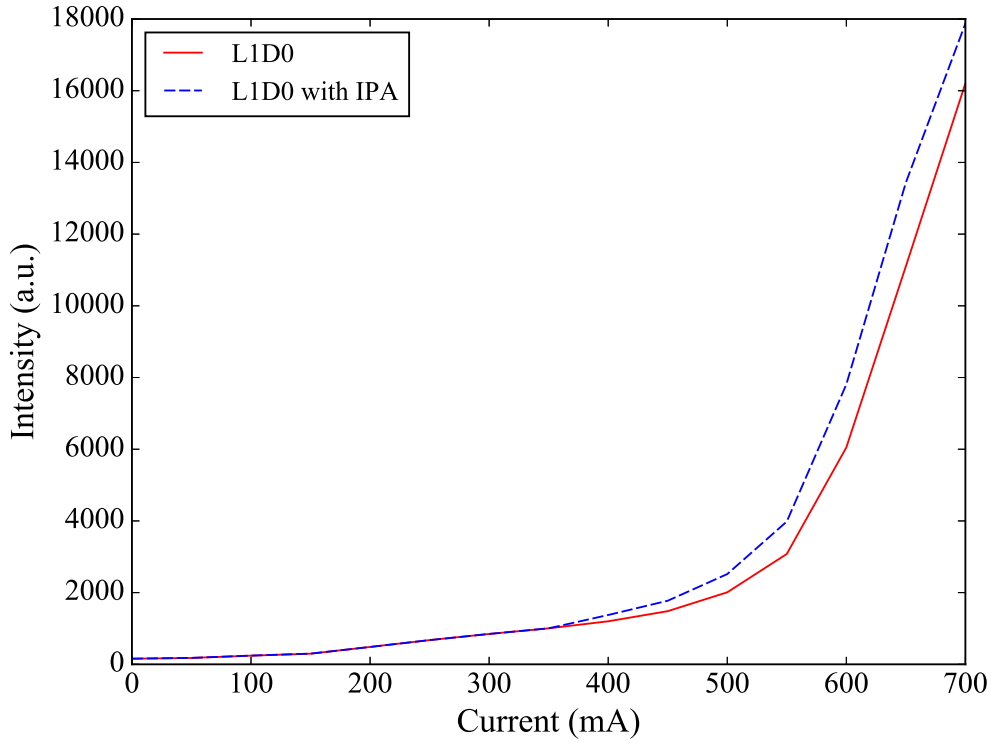

Figure 6.6: L-I curves for a coupled-cavity device with the SU-8 micro-fluidic channel empty (red solid line) and filled with isopropyl alcohol (blue dashed line) measured using one section as a source 'L1', and the other as a detector 'D0', with and without IPA in the channel.

the IPA in the SU-8 microfluidic channel has very little influence on the behaviour of the individual laser sections. However, the coupling between laser 1 (L1) and detector 0 (D0) is improved as seen by the increase in light intensity of the L-I curve at all currents above 400 mA. The presence of IPA in the channel increases the refractive index of the gap between laser and detector pair, reducing the reflectivity of the two interfaces and improving the coupling between them.

The same experimental procedure can be applied to a laser/detector pair with internal etched-angled facets. L-I curves of two sections from a device, arranged as in figure 6.2, with an internal facet angle of 22.6^o and stripe wide 30 μm, are plotted in figure 6.7. The threshold current is apparent from the change in slope but, there is an increased amount of spontaneous emission detected below threshold. This can be explained by the increase in threshold current density and ASE due to the increased threshold gain of the lasers compared to those seen in figures 6.5 and 6.6.

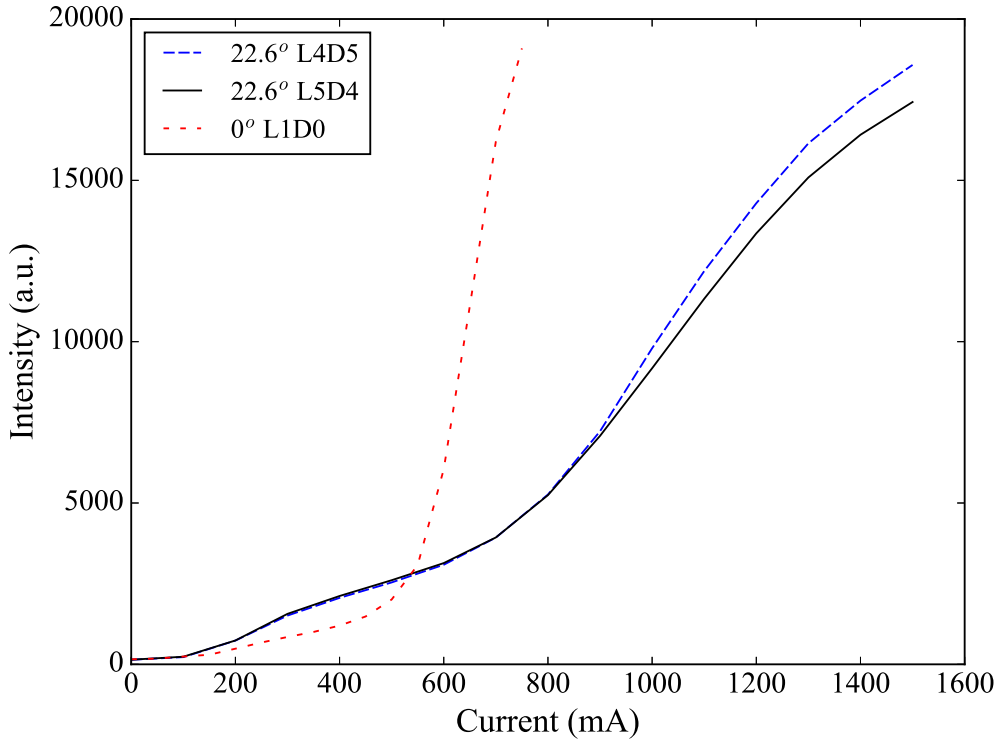

Figure 6.7: On-chip L-I measurement of an angled-facet laser/detector pair across the microfluidic channel (see figure 6.2). The internal, etched, facet angle of both L4 (blue dashed line) and L5 (solid black line) is 22.6^o. For comparison, an L-I (red dotted line) from a laser with an internal facet angle of 0^o has been included, showing the difference in performance.

6.4.1.1 Coupled-Cavity Detector Efficiency

As mentioned at the start of section 6.2, two additional sections have been included in the design to allow for C-C measurements on-chip as well as those from a single laser, offering added performance and functionality of the device. This section is identical to all other sections on the device, allowing for both detection and lasing operation. It is designed with a 100 μm gap between, for instance, sections 5 and 6, and has uncoated, etched, 0^o facets. However, figure 6.8 indicates a difference in detection performance.

D6 collects a significantly less amount of light from L5 as opposed to D4, suggesting its efficiency is compromised somehow. The main difference between these scenarios is the reflectivity of the emission and collection facets. The internal etched facets of L5 and D4 are coated in SU-8 due to the microfluidic channel design, whereas the rear and front facets of L5 and D6 respectively, are uncoated (i.e. they have a semiconductor-air interface). The lower reflectivity of the

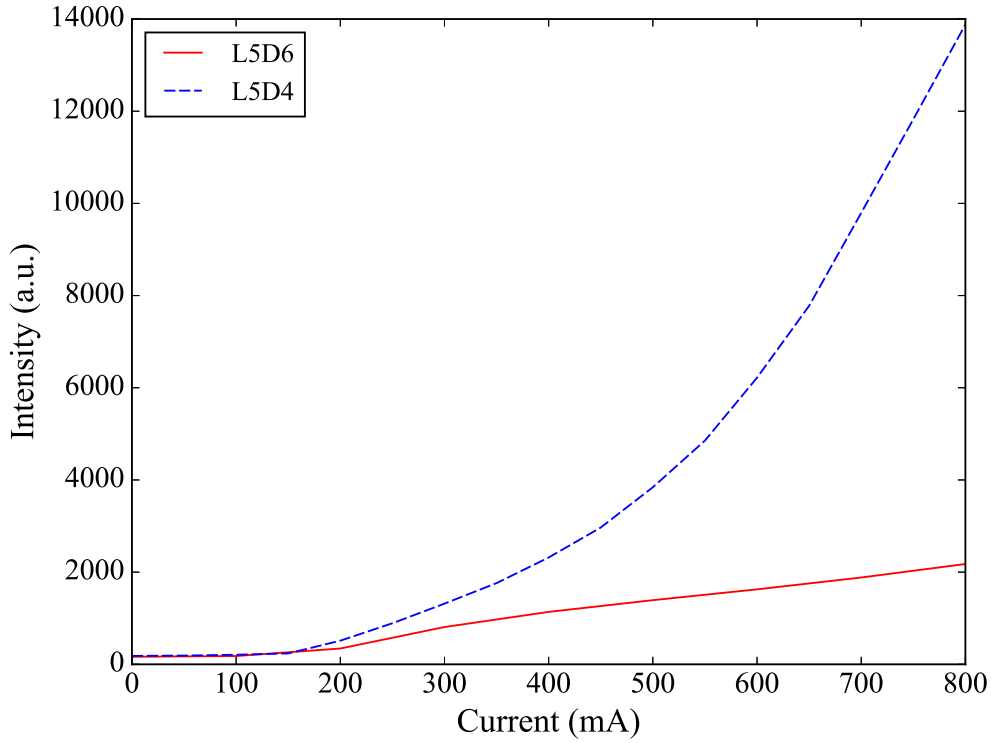

Figure 6.8: L-I curves for section 5 as a laser, L5, measured on; (i) D4 across the microfluidic channel (dashed blue line) and (ii) D6 at the rear of section 5 (solid red line).

semiconductor-SU-8 interface, calculated using equation 2.24 replacing n_{air} with $n_{SU-8} = 1.596$, suggests that this increases the coupling between sections, and enabling a higher percentage of light to be collected. Sufficient light must be collected on D6 (or D2) for C-C measurements and therefore, a design improvement must be made to ensure this is the case. A simplistic approach was taken for ease of fabrication, whereby SU-8 is patterned over the corresponding facets. Figure 6.9(a) shows an optical microscope image of the SU-8 patterned to cover both the rear facet of L5 and front facet of D6 (it is also the same for L1 and D2). A L-I curve of L5 is shown in figure 6.9(b) (to note, L5 here is from a different device to L5 in figure 6.8). The L-I curve of L5D6 now shows a much improved signal intensity, and is comparable to that of L5D4, indicating that this small addition to the fabrication process is enough to improve the detected signal, allowing for future C-C detection measurements.

6.4.2 Bead Detection

In this section, detection of polystyrene microbeads is demonstrated using both a 0^o and 22.6 ^{o} facet laser/detector configuration and experimental setup, described in section 6.3.

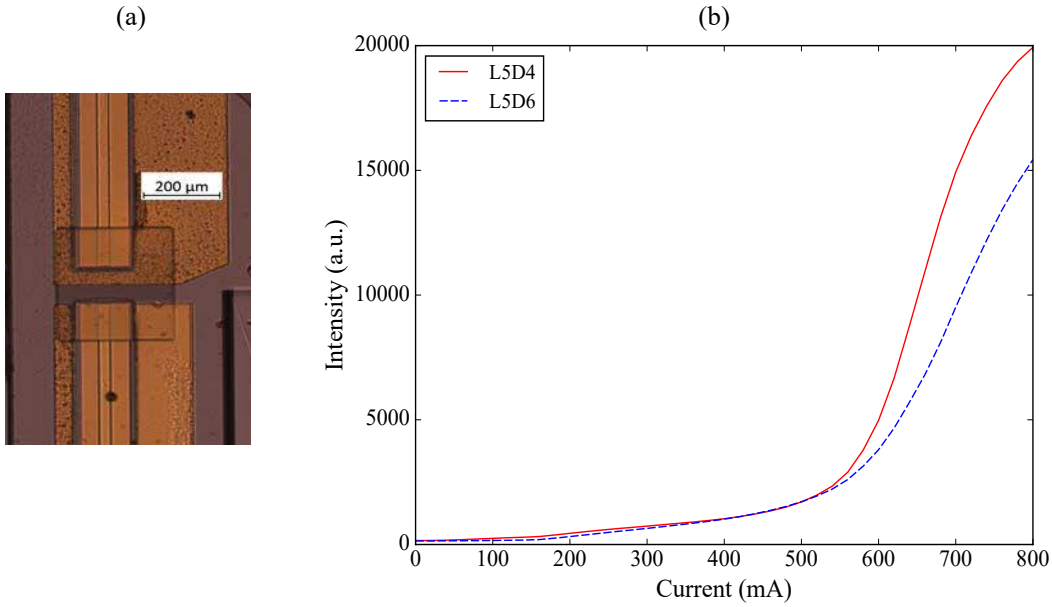

Figure 6.9: (a) Detector design with the inclusion of SU-8 over both emitting and detecting facets and (b) the resulting L-I curve from laser 5 on detector 6, L5D6 (blue dashed line) and the comparison to laser 5 on detector 4, L5D4, (red solid line) showing an improvement in D6 performance from figure 6.8.

Calibration beads in a suspension of water, 0.05% Tween 20 (a surfactant) and 2 mM sodium azide (a preservative), purchased from Thermo Fisher Scientific at a density of 2 x 10^7 beads/mL, were used in this section. A (2.0 $\pm$ 0.4) μL volume of (6.0 $\pm$ 0.3) μm beads was deposited in the inlet reservoir (LHS of figure 6.1), by pipette, and 60 s of data was recorded. The resulting photo-voltage, from a single, toggled, 0^o facet laser/detector pair, is plotted in figure 6.10.

The sharp increase in the background signal intensity of both traces, that occurs around 2 s, is a result of the initially empty channel filling with water. As mentioned previously, the presence of fluid, water in this case, in the channel increases the refractive index of the gap between laser and detector pair, reducing the reflectivity of the two interfaces and improving the coupling between them. Bead detection events appear in figure 6.10 as either positive or negative spikes and each event is captured by both detectors.

Previous work on bead detection in channels, using 10 μm ridge lasers, found that there are three main types of detection signals [9]. This has been attributed to the elliptical far-field distribution of the QW lasers and the fact that the beads can travel at varying heights through the channel.

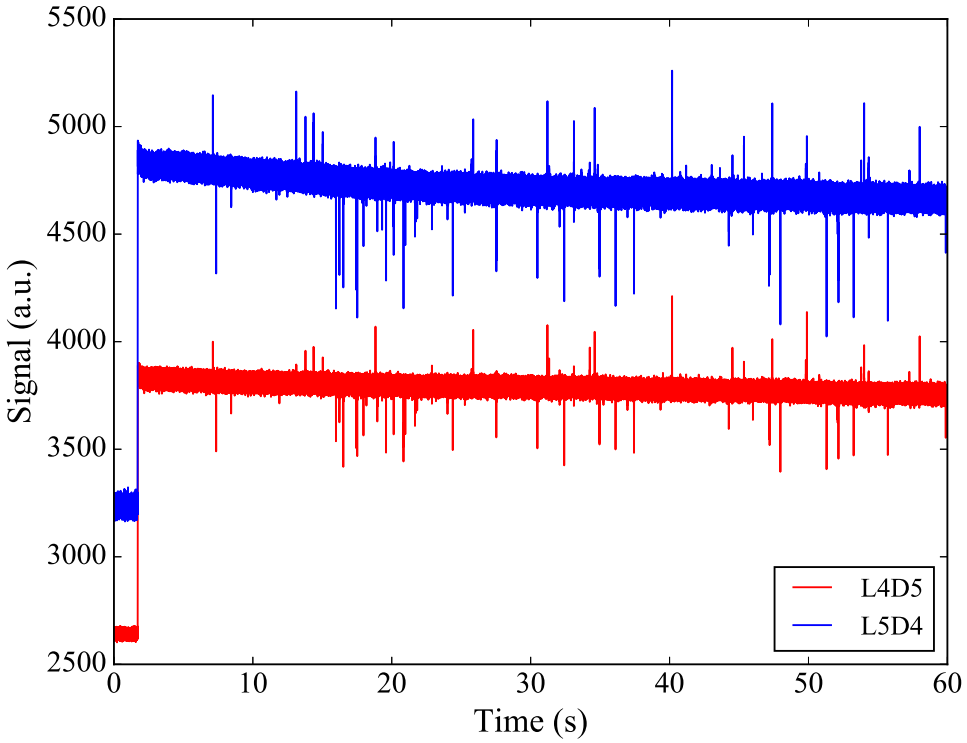

Figure 6.10: Photo-voltage signals from a laser/detector pair for a sample of 6 μm beads. The spikes in the data correlate to individual transit events.

On closer inspection of the data in figure 6.10, it is clear that there are still three types of bead events using a much wider beam. Each type of transit event produces a different measured signal depending on its height in the channel, and the measured signals for each type are plotted in figure 6.11.

If a bead is travelling at a height greater than one bead's radius in the channel, light falling on the detector is not interrupted by the bead. This is due to the relatively small dimension of the detector in the vertical direction ($\approx$ 500 nm) available when using a QW device as an in-plane photodetector. Signals measured, when a bead is at this channel height, produce a positive signal caused by the redirection of, otherwise divergent light rays, back inside the collection angle of the detector. This type of event, type 1, is seen in signal in figure 6.11(a). The signal in figure 6.11(c), is a decrease in signal intensity due to the bead blocking light falling on the detector. This type of event, type 3, occurs when the bead is travelling at a channel height above that of the detector. The third type of signal, type 2, is seen in figure 6.11(b). Here, the bead passes the detector at a central position in the channel, partially blocking the light when not exactly centred between laser

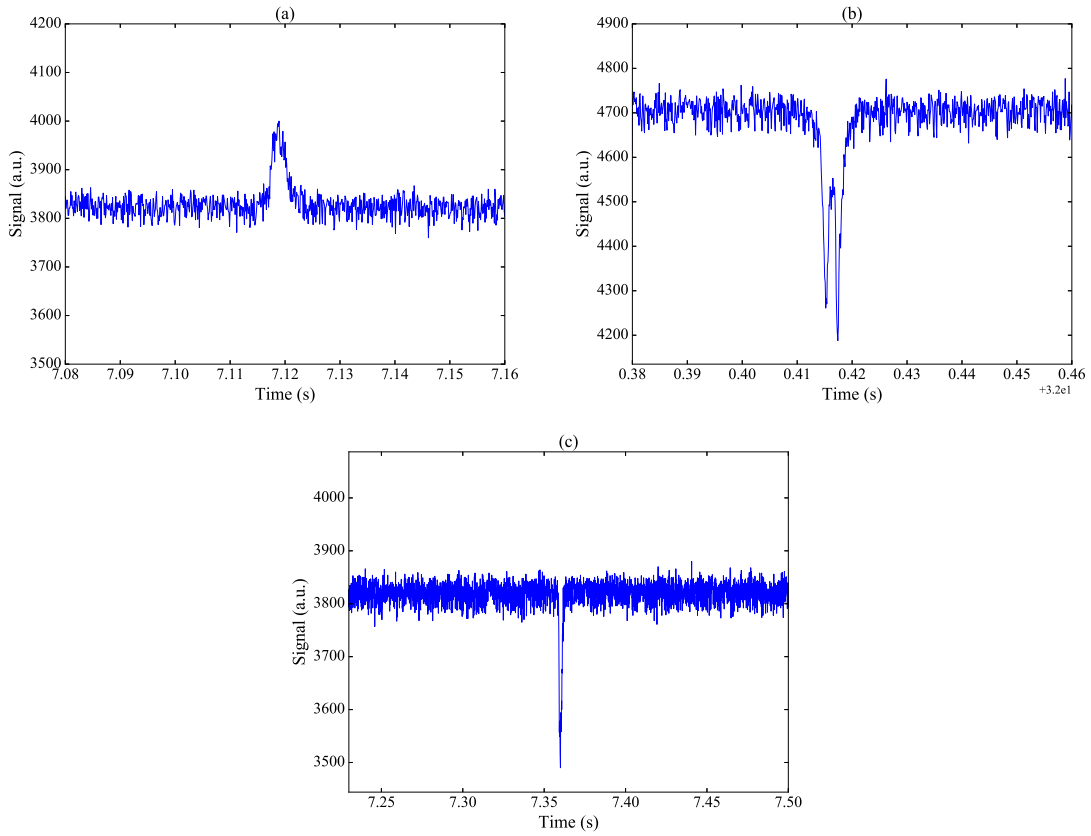

Figure 6.11: The three types of measured bead transit events for 6 μm microbeads: (a) a bead passing through the beam below the acceptance angle of the detector, (b) a bead passing through the beam in the central position of the detector and (c) bead passing through the beam above the height of the detector.

and detector laterally, and when centred enhancing the light falling on the detector by focussing the beam. The size of beads detected can be calculated from event types 2 and 3 [28] if two or three adjacent laser/detector pairs are used in sequence.

We also demonstrate the detection of (10.0 ± 0.1) μm polystyrene microbeads using a laser/detector pair with 22.6^o internal angled facets, the results of which are plotted in figure 6.12. The beads used here were also purchased from Thermo Fisher Scientific and were supplied at the same density and in the same suspension as the aforementioned 6 μm beads. The small number of transit events is due to a smaller concentration of beads being used, to prevent channel blockage. It is noticeable from figure 6.12(b) that the bead transit events are an inverted type 3. It is possible the angled facets enhance the light on the detector with the bead in a central position in the channel, due to the increased coupling between the laser and detector sections.

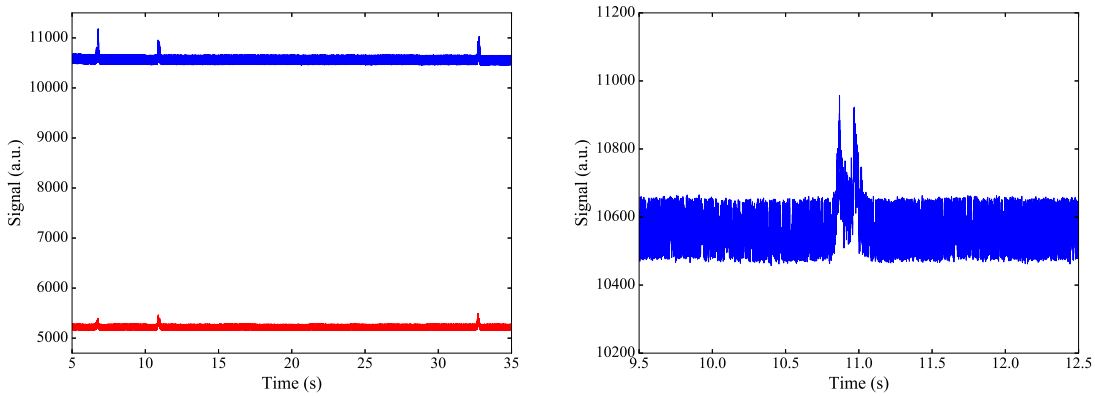

Figure 6.12: (a)Photo-voltage signals from a laser/detector pair for a sample of 10 μm beads. The spikes in the data correlate to individual transit events. (b) Zoom in of a event from (a) showing the nature of the transit events.

6.5 The Potential of a Coupled-Cavity Sensor

The advantages of proximity and alignment that are inherent in the monolithic configuration are somewhat negated by the limited vertical height of the active region but, the level of sensitivity demonstrated in the measurements in section 6.4.2, combined with the self-contained nature of the monolithic source/detector configuration, highlights the potential of this integrated device for C-C measurements.

This section starts by focussing on the coupling between two 0^o facet C-C sections using both wavelength and photocurrent measurements. Calculation of the gap loss allows determination of the C-C laser gain requirement, and using the gain-current density relationship in figure 5.3, a comparison can be made between C-C and individual section lasing. The gap loss is calculated for both 0^o and 22.6^o angled, etched, internal facets in section 6.5.1. Following this is evidence for C-C modes, with an angled facet C-C laser, using the light output measured from the device.

6.5.1 Gap Loss Model

A Gaussian beam model has been used to estimate the reduction in coupling strength that occurs in the coupled-cavity laser because of the diffraction losses that are incurred by the optical mode as it traverses the channel gap. The losses are assumed to be dominated by diffraction from the narrowest dimension of the waveguide, in this case, the direction perpendicular to the plane of the active region with the losses in the other transverse direction being ignored as they are considered

negligible by comparison (wide slab waveguide approximation) [16].

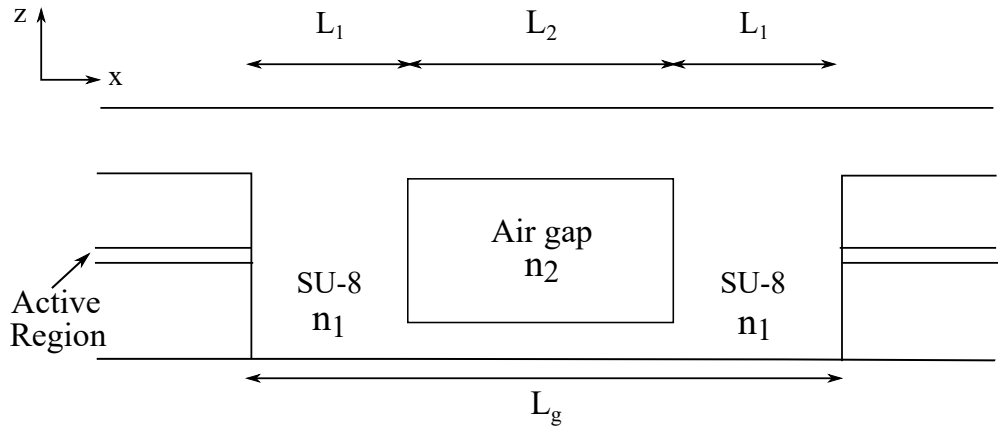

Figure 6.13: Schematic cross-section of the integrated device with the active region of the laser sections shown either side of the fabricated 3D SU-8 microfluidic channel with an air gap in the middle.

Assuming the fundamental mode of the waveguide, in the z-direction, has a Gaussian like E-field distribution, the E-field of the mode propagating the channel gap can be modelled by [10]

$$E(x,z) = E_0 \frac{w_0}{w(x)} \exp\left(\frac{-z^2}{w(x)^2}\right) \tag{6.1}$$

where w_0 is the beam width at which the field amplitude has dropped to 1/e of its peak value E_0. The beam width w is given by

$$w(x) = w_0 \sqrt{1 + \left(\frac{\lambda x}{\pi n w_0^2}\right)} \tag{6.2}$$

where λ is the lasing wavelength and n is the refractive index of the medium at a distance x. As $w(x)$ increases with an increase along the x-direction, the peak amplitude of the beam is reduced by $w_0/w(x)$.

The light emitted by the laser section is coupled into the fundamental mode of another section across the channel, and the coupling efficiency of the two can be approximated by the overlap integral of the incident E-field distribution, E_i, with the E-field distribution of the waveguide mode, E_m. Therefore, the normalised power coupling efficiency can be written as

$$P(x) = \frac{|\int E_i^* E_m dz|^2}{\int E_i^* E_i dz \int E_m E_m^* dz} \tag{6.3}$$

This leads to the equation

$$P(x) = \frac{2w_0 w(x)}{w_0^2 + w(x)^2} \tag{6.4}$$

Using equations 6.4 and 6.2 along with the approximation [14],

$$w_0 \approx 0.5h + 0.04\left(\sqrt{\frac{\lambda/n_1}{h}}\right) \tag{6.5}$$

where h is the active layer thickness, a value for $P(L_g)$ can be found. In this case, for the QW material in chapter 4, h is equal to 403 nm. $P(L_g)$ is the fraction of the electric field amplitude that is coupled from one laser section to the other after a single pass of the channel gap. This single pass loss can be converted to a gap loss, α_g, defined as the fractional reduction in the electric field amplitude per unit distance,

$$\alpha_g = \frac{1}{L} \ln \frac{1}{P(L_g)} \tag{6.6}$$

where L is the total length of the gain section, i.e. 2 x (L4+L5). The threshold net gain of the C-C laser, including a value for η_f found in chapter 5 in the α_m term , becomes

$$G_{th} - \alpha_i = \frac{1}{L} \ln \frac{1}{\eta_f R} + 2\alpha_g \tag{6.7}$$

The gap loss from equation 6.6 has been calculated for two scenarios; (i) with air in the SU-8 channel gap (as in figure 6.13) and (ii) filled with IPA, to compare the threshold net gain of a C-C laser with 0^o etched facets, with the results summarised in table 6.1. α_g is less when the channel is filled with IPA due to the smaller beam diffraction that occurs during the refractive index step from SU-8 (n_{SU-8}=1.596) to IPA (n_{IPA}=1.381) than to air (n_{air}=1). α_m is the same for both situations as this only depends on the cavity length and external facet reflectivities which do not change, assuming that the first reflector controls loss and there is no in phase feedback from second reflector.

These values can be compared to experimentally calculated $G_{th} - \alpha_i$, using L-I curves and the gain-current density relationship in figure 5.3, for laser sections of length 990 μm, width 30 μm and with a facet angle of 0^o. This analysis indicates that an individual laser section has a $G_{th} - \alpha_i$ equal to 51.8 cm^{-1}, concluding that this device will not achieve C-C lasing, simply because the gain requirement of the C-C laser is higher than that of its individual sections, even with IPA in the channel. It would be possible with higher refractive index fluids, such as diiodomethane or

Table 6.1: Summary of the calculated gap losses with; (i) air as fabricated and (ii) isopropyl alcohol (IPA) in the channel gap and their corresponding threshold net gain (G_{th}-α_i) values.

Channel	α_g (cm^{-1})	α_m (cm^{-1})	G_{th}-α_i (cm^{-1})
Air	22.2	11.5	56.1
IPA	20.6	11.5	53.2

compounds containing this chemical, however, these fluids are dark in colour, potentially dangerous and are not compatible with blood cells or other biological materials.

Once again using L-I curves and the gain-current density relationship in figure 5.3, $G_{th} - \alpha_i$, for a 22.6^o facet laser section, is equal to 64.4 cm^{-1}. Incorporating the gap loss for IPA, from table 6.1, in equation 6.7, results in $G_{th} - \alpha_i$ = 59.3 cm^{-1} for a 22.6^o C-C laser with IPA in the channel gap. This C-C laser gain threshold requirement is lower than that of the calculated individual section indicating that the two sections have the potential to lase on a resonant C-C mode. However, this calculated value does not include any additional diffraction or phase losses involved in lasing from an angled facet that may occur in practice.

The gain requirement of the C-C laser, although possible to achieve with large injection currents, could be reduced for improved device lifetime and ease of use with future on-chip electronics. This could be achieved by methods including, but not limited to; a narrower gap between the laser sections, increased length of the individual lasers, using a active substrate with a wider waveguide core and the use of high-reflectivity coatings on the outer facets. However, in practise the first two solutions are impractical due to the need of the SU-8 fluid channel in the gap and increasing the real-estate and therefore price, of the final device. The use of mode-expanded III-V material, where the width of the waveguide is much wider (h $\approx$ 1 μm) than that of the QW material used for this work, has the effect of narrowing the beam divergence. This would reduce the diffraction losses from the waveguide and therefore the associated gap loss. The next section investigates evidence of C-C modes in a device with etched, angled, internal facets, through the light output of the device.

6.5.2 Evidence of Coupled-Cavity Modes

The results from the 100 μm channel gap used in the device design, although ten times larger than previously used in C-C lasers, demonstrate that a significant amount of light can be coupled from one section to another across the microfluidic channel, as described in sections 6.4.1 and 6.4.2. This is only one component required for the formation of C-C modes. The other being, that resonant light in each of the individual sections is wavelength matched. I will look for the evidence of C-C modes in the measured output power of the device. Since calculations, in section 6.5.1, show that a device with 0^o facets will not lase as a C-C laser, the L-I characteristics of a 22.6^o facet device is used to establish a proof of principle C-C measurement.

The L-I curves for each individual laser section have been measured using the experimental setup in section 4.2.1 with an external detector, due to technical issues, and the device placed outside the cryostat. Taking external measurements presents difficulties with samples packaged like those seen in figure 3.26. The external detector has to be placed a distance away from the laser due to its size and this allows a small amount of scattered light from the connector pins to also be detected. For the C-C L-I measurement, a second pulse generator is used to drive one section with a fixed input current whilst the L-I characteristic of the opposing section is measured using the computer controlled pulse generator. To convert the injected current to current density, using cavity length and mode width, the same technique is used as in section 4.4.1. To compare the lasing performance of the individual sections to those of the C-C (comprised of those same sections), the light-current density curves have been plotted in figure 6.14.

Due to slightly different mode widths of section L0 and L1, their threshold current densities are slightly different. Each laser section, therefore, will lase at a different wavelength due to the current density dependence of the peak net modal gain, seen in figure 4.19. The L-J curve of the C-C laser does show a lower threshold current density than either of the individual sections on their own, implying there is a good degree of coupling between them. The spectral misalignment of the two sections means that the reduced threshold current density seen for the L0&L1 C-C in figure 6.14 is unclear. Lasing could occur from either a single C-C mode or one section is optically pumping another. Therefore, the wavelength output of the C-C device and each of its individual sections, has been measured using the setup in figure 4.3. Each section was pumped at 10% above

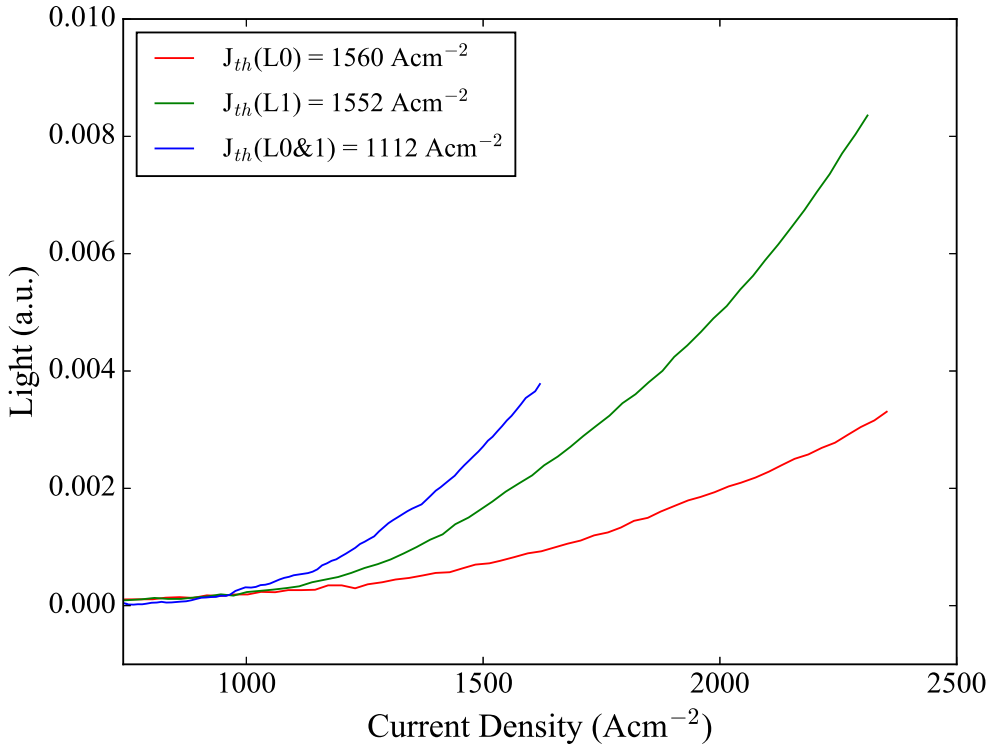

Figure 6.14: Comparison of the light versus current density of the coupled-cavity laser L0&1 (blue line) and the individual laser sections, L0 (red line) and L1 (green line).

the measured threshold current density in figure 6.14, with a scan resolution of 0.5 nm to obtain a large enough signal. The results of this are plotted in figure 6.15. The lasing spectra in figure 6.15 shows the section with the higher threshold current density operates at shorter wavelength and the section with lower threshold current density has a longer wavelength. With both sections operated together, the peak wavelength of L0&L1 does not have a clear red shift of the wavelength, as was expected with a lower threshold current density. The difference in gain requirement of an individual section and C-C laser, calculated in section 6.5.1 for an angled facet C-C laser, equates to an expected wavelength shift of 1.3 nm. However, the measured average peak wavelength is different by only 0.5 nm, within an error larger than 1.3 nm due to the scan resolution and broad nature of the spectra. This small shift makes it unclear as to whether the device is lasing as a C-C laser or L0 is optically pumping L1. Even if it is the case of an optically pumped section, this regime could still be used as a sensor to detect changes in the power output.

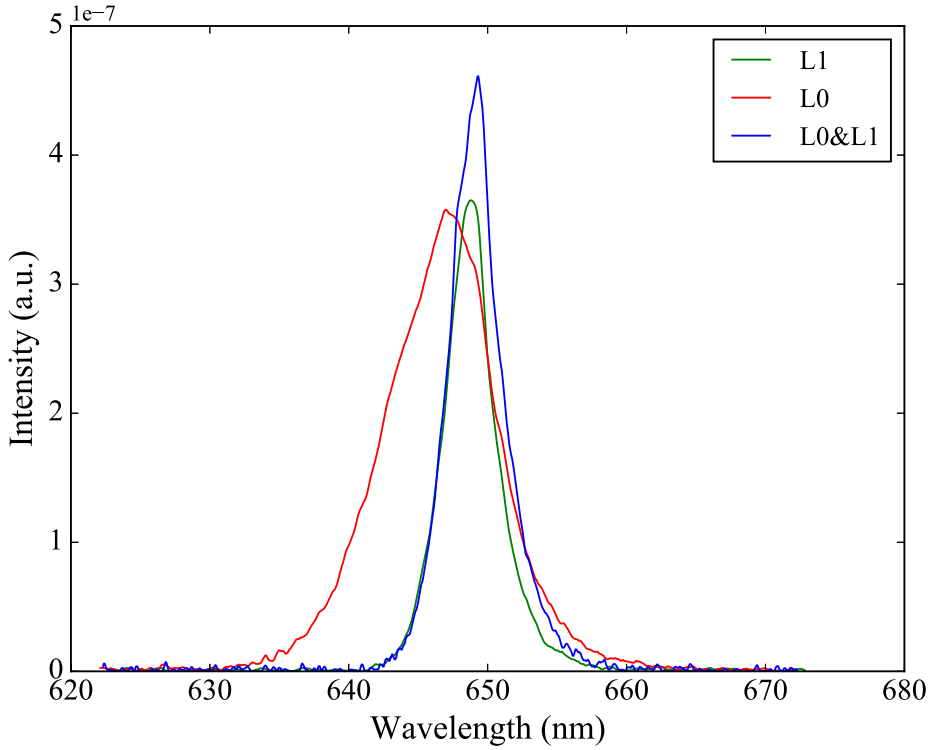

Figure 6.15: Lasing spectra for the coupled-cavity L0&L1 (blue line) and for the individual sections L0 (red line) and L1 (green line) driven independently.

6.6 Summary

Operating the device in a laser/detector configuration, allows the photo-current generated in the detector section to determine the L-I characteristics, of both 0^o and 22.6^o facet lasers, on chip, indicating coupled light between the two sections. The threshold current of a section is not affected by the addition of IPA in the SU-8 channel, but an increase in coupling is noticed. The generated photo-current has also been used to measure time-resolved bead transit events, of which there are three different types dependant on the beads' transit height through the beam.

When operating both laser sections together, in a C-C configuration, a device with 0^o will not achieve C-C lasing. The calculated C-C net gain threshold requirement is 4.3 cm^{-1} higher than that of a measured net gain value for an individual section, with air in the channel gap. There is a decrease in $G_{th} - \alpha_i$ for the addition of IPA in the channel, however, the gap loss is still too large for C-C lasing. Through incorporation of etched, angled, 22.6^o internal facets into the integrated device, $G_{th} - \alpha_i$ is higher than that of a 0^o facet section, but the reduction of the effective

reflectivity at the internal interfaces results in a lower overall threshold gain value, less than that of each individual section. Experimental evidence of C-C modes is seen in the reduction of threshold current density when operating both laser sections together as opposed to when each of the independent laser sections is driven alone. A small shift in wavelength is also seen in the C-C laser, but the sample may only be lasing through one section and optically pumping the other section. Even if this is the case, this device could still be used as a sensor by detecting a change in the output of the device.

References

[1] X. Fu and Z. Gagnon, *"Contactless microfluidic pumping using microchannel-integrated carbon black composite membranes"*, Biomicrofluidics., vol. 9, no. 5, pp. 054122, 2015

[2] F.A. Gomez, *"The future of microfluidic point-of-care diagnostic devices"*, Bioanalysis, vol. 5, no. 1, pp. 1-3, 2013

[3] H.-H. Jeong, A.G. Mark, M. Alarcon-Correa, I. Kim, P. Oswald, T.-C. Lee and P. Fischer, *"Dispersion and shape engineered plasmonic nanosensors"*, Nature Comm., vol. 7, art. no. 11331, 2016

[4] M. O'Toole and D. Diamond, *"Absorbance Based Light Emitting Diode Optical Sensors and Sensing Devices"*, Sensors, vol 8, pp. 2453-2479, 2008

[5] D.A. Heller, S. Baik, T.E. Eurell and M.S. Strano, *"Single-Walled Carbon Nanotube Spectroscopy in Live Cells: Towards Long-Term Labels and Optical Sensors"*, Advanced Materials, vol. 17, iss. 23, pp. 2793-2799, 2005

[6] M.C Gather and S.H. Yun, *"Single-cell biological lasers"*, Nature Photonics, vol. 5, pp. 406–410, 2011

[7] M. Schubert, K. Volckaert, M. Karl, A. Morton, P. Liehm, G.B. Miles, S.J. Powis and M.C. Gather, *"Lasing in Live Mitotic and Non-Phagocytic Cells by Efficient Delivery of Microresonators"*, Scientific Reports, vol. 7, no. 40877, 2017

[8] C.H. Henry and R.F. Kazarinov, *"Stabilization of Single-Frequency Operation of Coupled-Cavity Lasers"*, IEEE J. Quantum Electron., vol. QE-20, pp.733-744, July 1984

[9] R. Thomas, A. Harrison, D. Barrow and P.M. Smowton, *"Photonic integration platform with pump free microfluidics"*, Optics Express, vol. 25, 20, pp.23634-23644, 2017

[10] R. Thomas, *"Monolithic coupled-cavity laser diodes for bio-sensing applications"*, PhD Thesis, Cardiff University, 2012

[11] L.A. Coldren, K. Furuya, B.I. Miller and J.A. Rentschler, *"Etched Mirror and Groove-Coupled GaInAsP/InP Laser Devices for Integrated Optics"*, IEEE J. Quantum Electron., vol. QE-18, pp.1679-1687, Oct. 1982

Chapter 7

Conclusions & Future Work

7.1 Conclusions of this Work

This thesis has described the work that has been carried out to provide a proof of principle coupled-cavity (C-C) measurement, to be used in biosensing applications. This investigation has involved the fabrication of a novel capillary fill microfluidic sensing platform, experimental characterisation of a suitable active medium to support this proof of principle, the effect of etched, and angled, facets on device performance, and application of both laser/detector and C-C sensing.

Chapter 3 described the fabrication processes and steps involved in the fabrication of the final integrated C-C device. As well as fairly standard processes, the microfluidic delivery system required development of a deep-etched channel in the GaAs substrate, and the microfluidic channel itself. Using a 5% NH_3/H_2O_2 etch solution on the GaAs, resulted in a mean etch rate of (0.39 $\pm$ 0.12) μm/min, and showed no measurable difference between etch rates for n-type or S-I substrates. SU-8 was chosen for the fabrication of the microfluidic channels due to its chemical and optical property suitabilities. A single layer and a double exposure was all that was needed to create a 3D buried channel. In terms of development times, a minimum of 45 minutes was required to completely remove the photoresist from under the channel lid.

The work presented in chapter 4 involves the characterisation of a suitable active medium, consisting of both InAsP quantum dots (QDs) and GaInP quantum wells (QWs), to fabricate the integrated device. It focussed on how changes to the barrier width in the QD epitaxial structure could be used

to enhance device performance, and the drawback to using this QD structure. Results show that for all barrier width (8, 16, 24 nm) device performance is similar, however the slight improvement in the performance of the 8 nm barrier width sample is due to the shift of the dot ground state to a longer wavelength and a reduced leakage of carriers. Nevertheless, the QD structures presented here did not provide sufficient optical gain to overcome the expected losses inherent in the fabrication and design of the C-C device, and need improvement to be considered in the future for this work. Consequently, a GaInP QW structure was found to provide much higher gain magnitudes and was chosen for the work in the rest of the project.

A methodology for quantifying the efficiency of an etched laser facet, using the segmented contact method, was presented in chapter 5. This technique has been used to evaluate the efficiency of plasma etched facets, with a Cl_2/Ar etch chemistry, used in this work. It was found to be $\eta_f = 0.37 \pm 0.04$ for the GaInP QW material described in chapter 4. From SEM imaging, it was surmised that this efficiency was valid for etched facets of different angles. This angle being the angle of etching the facet off axis to the (001) plane. The effect of etched, angled facets on device performance is crucial for the incorporation into the final C-C device. Power-current (P-I) characteristics were obtained for cleaved-etched facet devices with varying etched angles. The threshold current density was shown to increase with facet angle, but is a non-linear increase. This is a result of a non-linear decrease in facet reflectivity with facet angle, with a very low reflectivity of $4.9\text{x}10^{-9}$ measured for a laser with a 14.9^o etched facet. Comparison of theoretical approximations of facet reflectivities reveals a close agreement with the experimental data. P-I curves were also used to investigate the external quantum efficiency, whereby increasing facet angle has a detrimental effect.

In chapter 6, the sensing capabilities of the microfluidic C-C device has been explored. Operating the device in a laser/detector configuration enabled on-chip light-current (L-I) measurements of both 0^o and 22.6^o facet lasers, indicating a good degree of coupling across the channel. The generated photo-current in the detector section, from light incident on it from a laser section, was also used to measure time-resoled bead transit events of both 6 and 10 μm microbeads. When both laser sections are operated together, in a C-C configuration, it was found that the incorporation of 22.6^o angled facets increased the threshold gain for free-running lasing of the individual, isolated

laser sections relative to that of the C-C operation such that the threshold gain of the C-C was less than that of each individual section. The evidence of this was seen in the power output of the device, where the C-C threshold current density was, on average, 440 Acm^{-2} less that its individual sections.

This integrated microfluidic C-C laser is promising as a microscale photonic device for blood cell analysis or other biosensing applications. The monolithic nature of the device offers inherent advantages in terms of alignment and proximity of the channel analyte and laser sections. This work has demonstrated the potential functionality of this device by identifying both laser/detector and C-C mechanisms for sensing applications.

7.2 Future Work

This work has been successful in developing an integrated capillary fill microfluidic coupled-cavity device with reproducible fabrication processes. However, there are certain aspects of this work that, in the future, could be undertaken to improve both the performance and functionality of the device.

Reducing cavity lengths of the laser sections in the integrated device would allow the optimisation of the coupled-cavity mechanism through its gain requirement. However, a cavity length less than 800 μm is incompatible with the requirements of the microfluidic design. Alternatively, improvement of the InAsP quantum dot structure, in chapter 4, is essential for increasing the achievable gain. This could be realised with the inclusion of additional p-doping, which if the states can be fully inverted, should result in a large optical gain. However, net gain values of 50 cm^{-1} will still not be possible with a QD system. An optimised quantum dot coupled-cavity should also produce a much larger wavelength shift for a given threshold current density change in a small device footprint. The quantum well structure in this work, in chapter 4, has a narrow spectral width, and the peak of the gain only achieving a small blue shift of the wavelength. The InAsP quantum dots have a much broader gain spectra and has a much larger peak gain shift. This has greater scope for wavelength tuning in the future, to always operate on the optimum part of the gain-current density curve.

6 μm microbeads have been shown to have a measurable effect on the photo-current signal on the detector, using a 30 μm wide oxide stripe laser. Beads of this diameter are comparable to the smallest type of human blood cells; erythrocytes (RBCs) and some types of lymphocytes (WBCs). For smaller particles, such as metallic nanoparticles ($\sim$ 500 nm), the measured photo-current using the coupled-cavity mechanism may not provide a large enough signal change to allow for their detection. It may be necessary therefore, to incorporate narrower ridge waveguides ($\leq$ 10 μm) into the device to maximise the influence of small particles on the optical coupling.

Ridge waveguides would also allow the incorporation of distributed feedback gratings on the laser sections, to select an optimum operating wavelength dependent on channel analyte. Differential absorption measurements at two wavelengths can be used to determine red blood cell counts and dual-wavelength operation, using an in-line laser geometry for differential measurements provides high device packing density around the fluid channel. The narrower nature of the ridge lasers offers the possibility of more complex device geometries, replicating flow cytometry functionality with both forward and side scatter detection. With the sub-microsecond toggling timescale of the lasers and detectors and vice versa, shown in chapter 6, this would facilitate multi-directional interrogation of each cell, going beyond traditional functionality.

In the future, for a completely self-contained system, we envisage our capillary fill, microscale optical sensor to be integrated on-chip with the functionality of the device control electronics. Replacing the computer with a smartphone enables complete system portability and allows non-specialised users access to a diagnostic tool for everyday use.